

MICROCOPY RESOLUTION TEST CHART
NATIONAL BUREAU OF STANDARDS-1963-A

DTIC FILE COPY

2

NAVAL POSTGRADUATE SCHOOL
Monterey, California

AD-A184 357



DTIC
ELECTE
SEP 10 1987
S D
C&D

THESIS

COUPLED ACOUSTIC AND OCEAN THERMODYNAMIC
MODEL

by

Jacques M. Fourniol

June 1987

Co-Advisor
Co-Advisor

Rolland W. Garwood
Lawrence J. Ziomek

Approved for public release; distribution is unlimited.

87 9 9 106

A184 357

SECURITY CLASSIFICATION OF THIS PAGE

REPORT DOCUMENTATION PAGE

1a REPORT SECURITY CLASSIFICATION UNCLASSIFIED		1b RESTRICTIVE MARKINGS	
2a SECURITY CLASSIFICATION AUTHORITY		3 DISTRIBUTION/AVAILABILITY OF REPORT Approved for public release; distribution is unlimited	
2b DECLASSIFICATION/DOWNGRADING SCHEDULE		5 MONITORING ORGANIZATION REPORT NUMBER(S)	
4 PERFORMING ORGANIZATION REPORT NUMBER(S)		7a NAME OF MONITORING ORGANIZATION Naval Postgraduate School	
6a NAME OF PERFORMING ORGANIZATION Naval Postgraduate School	6b OFFICE SYMBOL (if applicable) 68	7b ADDRESS (City, State, and ZIP Code) Monterey, California 93943-5000	
6c ADDRESS (City, State, and ZIP Code) Monterey, California 93943-5000		9 PROCUREMENT INSTRUMENT IDENTIFICATION NUMBER	
8a NAME OF FUNDING/SPONSORING ORGANIZATION	8b OFFICE SYMBOL (if applicable)	10 SOURCE OF FUNDING NUMBERS	
8c ADDRESS (City, State, and ZIP Code)		PROGRAM ELEMENT NO	PROJECT NO
		TASK NO	WORK UNIT ACCESSION NO
11 TITLE (Include Security Classification) COUPLED ACOUSTIC AND OCEAN THERMODYNAMIC MODEL			
12 PERSONAL AUTHOR(S) FOURNIOL, Jacques, M.			
13a TYPE OF REPORT Master's thesis	13b TIME COVERED FROM _____ TO _____	14 DATE OF REPORT (Year, Month, Day) 1987 June	15 PAGE COUNT 101
16 SUPPLEMENTARY NOTATION			
17 COSATI CODES		18 SUBJECT TERMS (Continue on reverse if necessary and identify by block number)	
FIELD	GROUP	Acoustic ray tracing	
	SUB-GROUP	Ocean mixed layer	
19 ABSTRACT (Continue on reverse if necessary and identify by block number)			
<p>→ An acoustic ray tracing algorithm is developed and coupled with a thermodynamic upper ocean mixed layer model. For a test case, the coupled mixed layer-acoustic model is applied to a specific area in the western Mediterranean Sea. Climatological atmospheric forcing is used to provide boundary conditions for the mixed layer for short periods of time during different seasons. The response of the acoustic model to the predicted changes in the sound-speed profile is analyzed to show dependence of acoustic propagation upon the surface atmospheric forcing and the season. The atmospheric factors such as wind, rain, and solar irradiation have almost no effect on the propagation of rays emanating from a deep transmitter. In the case of a shallow source, the wind is the most dominating factor which influences the acoustic propagation. The effect of heavy rain with light wind is also examined. ←</p>			
20 DISTRIBUTION/AVAILABILITY OF ABSTRACT <input checked="" type="checkbox"/> UNCLASSIFIED/UNLIMITED <input type="checkbox"/> SAME AS RPT <input type="checkbox"/> DTIC USERS		21 ABSTRACT SECURITY CLASSIFICATION unclassified	
22a NAME OF RESPONSIBLE INDIVIDUAL Garwood, R.		22b TELEPHONE (Include Area Code) (408) 646 2552	22c OFFICE SYMBOL 68Gd

Approved for public release; distribution is unlimited.

Coupled Acoustic and Ocean Thermodynamic Model

by

Jacques M. Fourniol
Capitaine de Corvette, French Navy

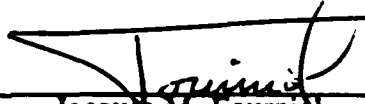
Submitted in partial fulfillment of the
requirements for the degrees of

MASTER OF SCIENCE IN OCEANOGRAPHY
and
MASTER OF SCIENCE IN ENGINEERING SCIENCE

from the

NAVAL POSTGRADUATE SCHOOL
June 1987

Author:



Jacques M. Fourniol

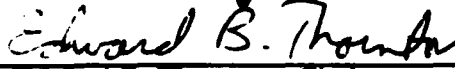
Approved by:



Roland W. Garwood, Co-Advisor



Lawrence J. Ziomek, Co-Advisor



Edward B. Thornton, Chairman,
Department of Oceanography



John P. Powers, Chairman, Department
of Electrical and Computer Engineering



Gordon E. Schacher,
Dean of Science and Engineering

ABSTRACT

An acoustic ray tracing algorithm is developed and coupled with a thermodynamic upper ocean mixed layer model. For a test case, the coupled mixed layer-acoustic model is applied to a specific area in the western Mediterranean Sea. Climatological atmospheric forcing is used to provide boundary conditions for the mixed layer for short periods of time (from few hours to three days) during different seasons. The response of the acoustic model to the predicted changes in the sound-speed profile is analyzed to show dependence of acoustic propagation upon the surface atmospheric forcing and the season. The atmospheric factors such as wind, rain, and solar irradiation have almost no effect on the propagation of rays emanating from a deep transmitter. In the case of a shallow source, the wind is the most dominating factor which influences the acoustic propagation. The effect of heavy rain with light wind is also examined.



Accession For		
NTIS	CRA&I	<input checked="" type="checkbox"/>
DTIC	TAB	<input type="checkbox"/>
Unannounced		<input type="checkbox"/>
Justification		
By		
Distribution/		
Availability Codes		
Dist	Avail and/or special	
A-1		

TABLE OF CONTENTS

I.	INTRODUCTION	10
II.	ACOUSTIC MODEL	11
	A. INTRODUCTION	11
	B. SPEED OF SOUND AS A FUNCTION OF DEPTH WITH CONSTANT GRADIENT	12
	C. ALGORITHM	15
	1. Case 1 : $g_{k-1} > 0, g_k > 0$	17
	2. Case 2 : $g_{k-1} < 0, g_k < 0$	21
	3. Case 3 : $g_{k-1} > 0, g_k < 0$	22
	4. Case 4 : $g_{k-1} < 0, g_k > 0$	23
	5. Surface and bottom reflections	25
	D. SUMMARY AND DIRECTIVES TO USE THE SUBROUTINE RAY	26
	1. Main characteristics	26
	2. Features of this subroutine	27
	3. Example	28
III.	OCEAN MIXED LAYER MODEL	30
	A. INTRODUCTION	30
	1. Characteristics of the oceanic mixed layer	30
	2. Generalities on the dynamics of the mixing	30
	3. The model and its features not previously demonstrated	33
	B. FORMULATION OF THE EQUATIONS USED IN THIS OBL MODEL	33
	1. Generalities	33
	2. Mean buoyancy and momentum equations	34
	3. Mean turbulent kinetic energy equation	37
	4. Modeling of the different terms of the integrated TKE equation	38

	5. Closure hypothesis	41
C.	SUMMARY OF MODELED EQUATIONS	41
IV.	COUPLING THE TWO MODELS	43
	A. GENERALITIES	43
	B. INITIAL CONDITIONS	43
	C. BOUNDARY CONDITIONS	45
	D. OTHER INPUT PARAMETERS	47
	E. OUTPUTS OF THE OBL MODEL	47
	F. SOUND-SPEED COMPUTATION	47
	G. RAY TRACING	47
	H. NOTE ON THE ALGORITHM USED IN THE ACOUSTIC MODEL	48
V.	APPLICATION OF THE COUPLED MODEL TO A SPECIFIC AREA 50	
	A. GENERALITIES	50
	B. SUMMARY OF THE DIFFERENT PARAMETERS USED IN THIS STUDY	52
	C. DECEMBER CASE	55
	1. Source at 10 meters	55
	2. Source at 40 meters	62
	3. Source at 100 meters	64
	4. Source on the SOFAR axis (150 meters)	64
	5. Source at 500 meters	70
	6. Conclusions for December	70
	D. FEBRUARY CASE	72
	1. Source at 10 meters	72
	2. Source at 200 meters	74
	3. Conclusions for February	78
	E. JUNE CASE	80
	1. Source at 10 meters	82
	2. Source on the SOFAR axis (90 meters)	85
	3. Conclusions for June	85

VI. CONCLUSION 89
A. ADVANTAGES OF THE COUPLED MODEL 89
B. WEAKNESS OF THE COUPLED MODEL 89
C. RECOMMENDATIONS 90
APPENDIX : RAY TRACING SUBROUTINE USE EXAMPLE 91
LIST OF REFERENCES 97
INITIAL DISTRIBUTION LIST 99

LIST OF TABLES

1. PARAMETERS AND DATA USED IN THE EXAMPLE OF SUBROUTINE RAY SHOWN IN FIGURE 2.11	28
2. WIND SPEED AND WIND STRESS CORRESPONDENCE	46
3. HEAT FLUXES CLIMATOLOGY FOR THE MEDITERRANEAN (W/M ²)	55
4. EVOLUTION OF THE MIXED LAYER DEPTH IN DECEMBER WITH A STRONG WIND	58
5. EVOLUTION OF THE MIXED LAYER DEPTH IN DECEMBER WITH LIGHT WINDS AND HEAVY RAIN FOR 12 HRS	61
6. EVOLUTION OF THE MIXED LAYER DEPTH IN FEBRUARY WITH A STRONG WIND	72
7. EVOLUTION OF THE MIXED LAYER DEPTH IN FEBRUARY WITH A LIGHT WIND	78
8. EVOLUTION OF THE MIXED LAYER DEPTH IN JUNE WITH STRONG WINDS	81
9. MAXIMUM AND MINIMUM ML DEPTHS AND TEMPERATURES IN JUNE FOR LIGHT WIND CONDITIONS WITH NO CLOUDS	82

LIST OF FIGURES

2.1	Ray path confined to the YZ plane	12
2.2	An infinitesimal element of arc length ds at an arbitrary point P along a ray path in YZ plane	13
2.3	Parameters describing a one-meter-depth increment positive gradient sound-speed profile for an upward travelling acoustic ray path	16
2.4	Case 1 : $g_{k-1} > 0, g_k > 0$	17
2.5	Turning point treatment	20
2.6	Case 2 : $g_{k-1} < 0, g_k < 0$	21
2.7	Case 3 : $g_{k-1} > 0, g_k < 0$	23
2.8	Case 4 : $g_{k-1} < 0, g_k > 0$	24
2.9	Perfect surface reflection possibilities	25
2.10	Perfect bottom reflection possibilities	26
2.11	Ray tracing provided by subroutine RAY	29
3.1	Idealized model for ocean mixed layer.	31
3.2	Mechanical energy budget for the ocean mixed layer	32
4.1	Coupling the OBL model with the ray tracing program	44
4.2	Simulated diurnal cycle	45
4.3	Piecewise linear approximation of a typical sound-speed profile	48
5.1	The northern region of the Algero-Provencal Basin	50
5.2	Seasonal variation of the temperature profile in the northern part of the Western Mediterranean	51
5.3	SSP for the Ligurian Sea, Western Mediterranean February to July from left to right	53
5.4	SSP for the Ligurian Sea, Western Mediterranean August to January from right to left	54
5.5	December, strong wind, source at 10 meters: $t = 0,24$ hrs, $\theta = 6^\circ$	56
5.6	December, transformation of R-SR rays, strong wind: $t = 0,24$ hrs	57
5.7	December, light wind, heavy rain for 12hrs, source at 10 meters: $t = 0,6$ hrs, $\theta = 5^\circ$	59

5.8	December, light wind, heavy rain for 12 hrs, source at 10 meters: t = 12,14 hrs, $\theta = 5^\circ$	60
5.9	December, strong wind, source at 40 meters: t = 0,24 hrs, $\theta = 6^\circ$	63
5.10	December, strong wind, source at 40 meters: t = 0,24 hrs, $\theta = 2.5^\circ$	65
5.11	December, light wind, heavy rain, source at 40 meters: t = 0,12 hrs, $\theta = 6^\circ$	66
5.12	December, strong wind, source at 100 meters: t = 0,24 hrs, $\theta = 6^\circ$	67
5.13	December, strong wind, source at 80 meters: t = 0,24 hrs, $\beta_0 = 91^\circ$ to 93°	68
5.14	December, strong wind, source at 150 m: t = 0,48 hrs, $\theta = 9^\circ$	69
5.15	December, strong wind, source at 500 m: t = 0,24 hrs, $\theta = 6^\circ$	71
5.16	February, strong wind, source at 10 meters: t = 0,24 hrs, $\theta = 12^\circ$	74
5.17	February, light wind, source at 10 meters: t = 0,12 hrs, $\theta = 8^\circ$	75
5.18	February, light wind, source at 10 meters: t = 0,8 hrs, $\theta = 6^\circ$	76
5.19	February, light wind, heavy rain, source at 10 meters: t = 0,12 hrs, $\theta = 8^\circ$	77
5.20	February, light wind, heavy rain, source at 200 meters: t = 0,12 hrs, $\theta = 8^\circ$	79
5.21	Variation of sound-channel width d for similar temperature changes in (a) the Mediterranean and (b) the Atlantic	80
5.22	June, strong wind, source at 10m: t = 0,24 hrs, $\theta = 8^\circ$	83
5.23	June, strong wind, source at 10m: t = 0,24 hrs, $\theta = 8^\circ$	84
5.24	June, strong wind, source at 90 meters: t = 0,24 hrs, $\theta = 8^\circ$	86
5.25	June, strong wind, source at 90 meters, t = 0,48 hrs, $\beta = 81^\circ, 82^\circ, 83^\circ, 97^\circ, 98^\circ, 99^\circ$	87
5.26	June, strong wind, sources at 10 and 90 meters t = 0,48 hrs, $\theta = 8^\circ$	88

I. INTRODUCTION

An acoustic ray tracing program is coupled with the Oceanic Boundary Layer Model developed by Garwood [Ref. 1]. The OBL model is a one-dimensional, second-order turbulence closure, vertically integrated model of the ocean surface turbulent boundary layer, using a two-component turbulent kinetic energy budget with a mean turbulent field closure.

Fisher [Ref. 2] investigated the variability and sensitivity of a coupled model system. He found that the OBL model, when integrated in time at a single point (Ocean Station Papa 50°N 145°W), predicted mixed-layer structure better than did the Expanded Ocean Thermal Structure (EOTS) system which was currently in use at the Fleet Numerical Oceanography Center (FNOOC). McManus [Ref. 3] evaluated the acoustic performance of a coupled model system at a line of stations in the northeast Pacific Ocean. In both cases, the thermodynamic model was initialized with observed temperature profiles, and the surface boundary conditions were given by the currently available meteorological informations. Then, the thermodynamic forecasts were input into acoustic models, such as RAYMODE or FACT, and the acoustic performance was analyzed using the median detection range (MDR) and the convergence zone range (CZR).

This research is the first attempt to link in a single program the OBL model with an acoustic model. Simplicity (compared to the operational models available in the U.S. Navy) and classification restrictions lead us to develop in Chapter II an algorithm for acoustic ray tracing. As no such routine was available at NPS, a copy is attached in the appendix for further use by students of the Air-Ocean Sciences Department. This simple subroutine allows the influence of the atmospheric forcing on the underwater sound propagation to be qualitatively analyzed. A summary of the leading principles and equations of the OBL model is given in Chapter III. Chapter IV develops in detail the actual coupling of the two models into a single computer code. Chapter V gives an example of the use of this coupled model applied to a specific area in the western Mediterranean Sea, for different periods of the year having particular acoustic properties. All the simulations were integrated in time using climatological data over short time periods varying from a few hours to three days.

II. ACOUSTIC MODEL

A. INTRODUCTION

Since we assumed in this research that the ocean is horizontally stratified, the temperature T and the salinity S are only functions of the depth y and cannot vary with the range z . Hence, the speed of sound c is only a function of depth y . In that case, according to Ziomek [Ref. 4: p.236], the general form of the equation for the horizontal range travelled by an acoustic ray is the following :

$$z = z_0 + b \int_{y_0}^y \frac{c(\zeta)}{[1-b^2c^2(\zeta)]^{1/2}} d\zeta \quad (2.1)$$

where b is the ray parameter and is given by

$$b = \sin\beta(y_0) / c(y_0), \quad (2.2)$$

(y_0, z_0) are the coordinates of the source, and $\beta(y_0)$ is the initial angle of propagation.

Thus, theoretically, knowing the sound-speed profile versus the depth, we can plot the curve giving the path of an acoustic ray.

We chose not to use equation (2.1) for the following reasons:

According to Snell's law,

$$\frac{\sin\beta(y)}{c(y)} = \frac{\sin\beta(y_0)}{c(y_0)} = b \quad (2.3)$$

and, at a turning point, $\beta(y_{tp}) = \pi/2$ and $c(y_{tp}) = 1/b$ such that the denominator of the integrand of (2.1) goes to zero and the integration cannot be carried out. Thus (2.1) is only valid between two turning points.

Numerically, the integration of (2.1) would be carried out between all the turning points of the ray by discretizing the sound-speed profile $c(y)$ with as small a depth increment as required to get an acceptable result. Furthermore, during the integration, we would have to test for the occurrence of a turning point.

However, a sound-speed profile can be approximated by straight line segments matching the profile as best as possible. The more segments chosen, the better the computation. Roughly, we often choose 10 to 15 segments depending on the shape of the profile. Then, as explained in the next section, the integration of (2.1) can be solved analytically for each segment of straight line and leads to very simple equations.

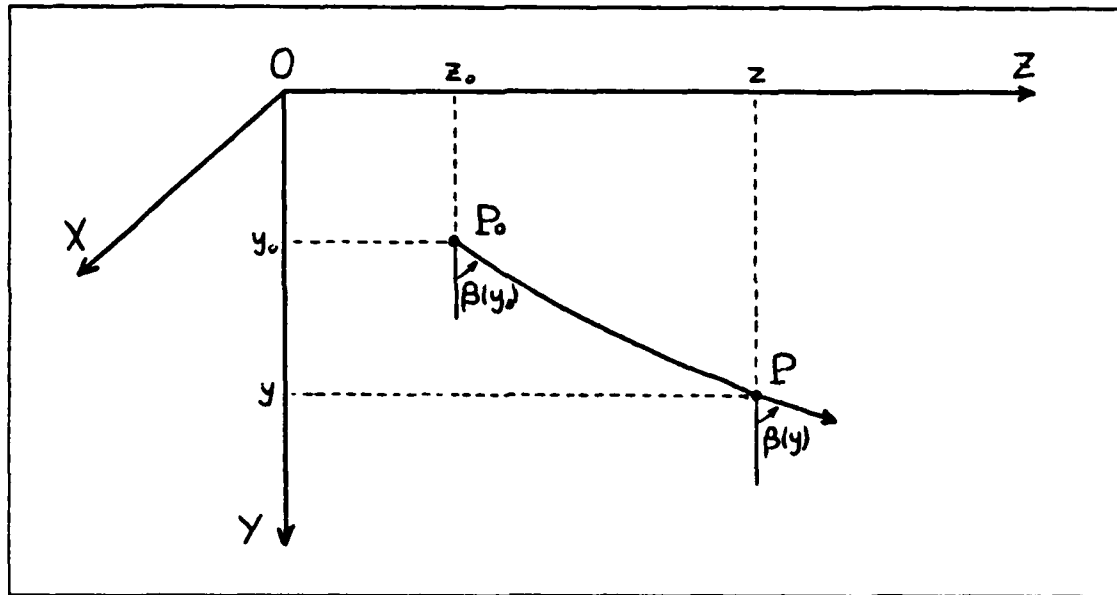


Figure 2.1 Ray path confined to the YZ plane.

We shall keep in mind that this acoustic model has to be coupled with an Oceanic Planetary Boundary Layer (OPBL) model [Ref. 1] which resolves the temperature, salinity, and depth of the upper mixed layer of the ocean using a one-meter-step increment for the depth.

These are the reasons why we chose to discretize the sound-speed profile with a one-meter-depth increment, assume the profile to be a straight line segment within each depth increment, and we use the equations derived in the next section instead of numerically evaluating the integral of (2.1). We found this method easier for handling the turning point problem.

B. SPEED OF SOUND AS A FUNCTION OF DEPTH WITH CONSTANT GRADIENT

The sound-speed profile is given by

$$c(y) = c_0 + g \times (y - y_0) \quad (2.4)$$

where g is a constant (with units of s^{-1}) referred to as the gradient since

$$\frac{dc(y)}{dy} = g. \quad (2.5)$$

Starting with Snell's law (2.3), differentiation leads to:

$$\cos\beta(y) d\beta = b dc(y) = bg dy. \quad (2.6)$$

Referring to Figure 2.2, it can be easily seen that :

$$\frac{dy}{ds} = \cos\beta(y). \quad (2.7)$$

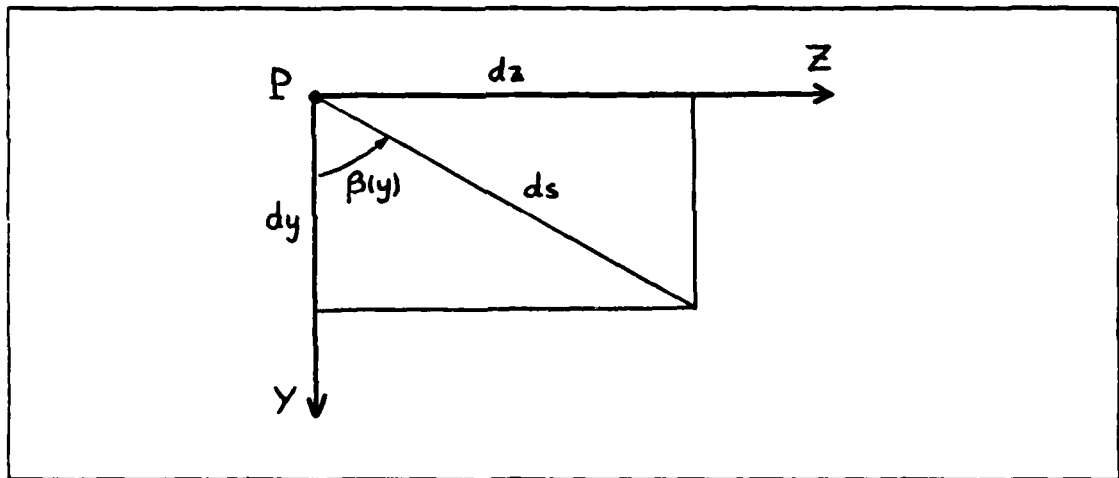


Figure 2.2 An infinitesimal element of arc length ds at an arbitrary point P along a ray path in YZ plane.

Substituting (2.7) in (2.6) yields

$$\frac{d\beta(y)}{ds} = bg. \quad (2.8)$$

Equation (2.8) indicates that the curvature along a ray path is constant. Thus, the ray path is an arc of a circle. From Figure 2.2, we have

$$dz = \tan\beta(y) dy = \sin\beta(y) \frac{dy}{\cos\beta(y)} . \quad (2.9)$$

Using (2.6), we get

$$dz = \sin\beta(y) \frac{d\beta(y)}{bg} . \quad (2.10)$$

Integration leads to

$$z = z_0 + \int_{\beta_0}^{\beta} \frac{\sin\beta}{bg} d\beta \quad (2.11)$$

where $\beta_0 = \beta(y_0)$ is the initial angle of propagation at the source, and $\beta = \beta(y)$ is the angle of propagation at position P. This leads to

$$z = z_0 + \frac{1}{bg} (\cos\beta_0 - \cos\beta) . \quad (2.12)$$

Solving for the depth y in (2.4) yields

$$y = y_0 + \frac{1}{g} (c(y) - c_0) , \quad (2.13)$$

and, using Snell's law (2.3), we get

$$y = y_0 + \frac{1}{bg} (\sin\beta - \sin\beta_0) . \quad (2.14)$$

We can verify that (2.12) and (2.14) are the parametric equations (parameter β) of the circle given by :

$$\left[y - \left(y_0 - \frac{\sin \beta_0}{bg} \right) \right]^2 + \left[z + \left(z_0 + \frac{\cos \beta_0}{bg} \right) \right]^2 = \left(\frac{1}{bg} \right)^2 \quad (2.15)$$

centered at $\left(y_0 - \frac{\sin \beta_0}{bg}, -\left(z_0 + \frac{\cos \beta_0}{bg} \right) \right)$ and having a radius of $1/bg$.

C. ALGORITHM

For this research, we used a modified version of the basic FORTRAN subroutine RAY given in appendix A. In this section we are going to analyze in detail the different parts of the algorithm used in the subroutine RAY.

The goal of this subroutine is to plot the acoustic ray path, that is, the curve giving the range z in kilometers versus the depth y in meters of an acoustic ray emanating from a source at a depth y_0 at a given initial angle of propagation. The ray path plot is presented beside the graph of the sound-speed profile $c(y)$ in m. sec versus depth y in meters.

As we mentioned previously, we used a one-meter-step depth increment and kept track of the depth all along the ray by using an increasing or decreasing index k depending on the ray going upward or downward. The index k is, in fact, the integer value of the depth.

The angles of propagation β and β_0 are referenced from the Y axis. For plotting purposes, we defined the depth vector $\{ y_i, i = 0, NN \}$ and the range vector $\{ z_i, i = 0, NN \}$. At the i^{th} point of the ray path, the depth index k is

$$k = y_i, \quad (2.16)$$

the "initial" angle of propagation is β_0 , the sound-speed is c_k and, its gradient, g_k , is given by

$$g_k = c_{k+1} - c_k. \quad (2.17)$$

At the $(i+1)^{\text{th}}$ point on the ray path, the depth index is $k \pm 1$ the "final" angle of propagation is β , the sound-speed is $c_{k \pm 1}$ and the gradient is $g_{k \pm 1}$. An illustration of these different parameters is given in Figure 2.3.

For that case, according to (2.3) and (2.12), we would have

$$y_{i+1} = k - 1 \quad (2.18)$$

and

$$z_{i+1} = z_i + \frac{1}{bg_{k-1}} (\cos\beta_0 - \cos\beta) \quad (2.19)$$

with

$$\frac{\sin\beta}{c_{k-1}} = \frac{\sin\beta_{\text{source}}}{c_{\text{source}}} = b. \quad (2.20)$$

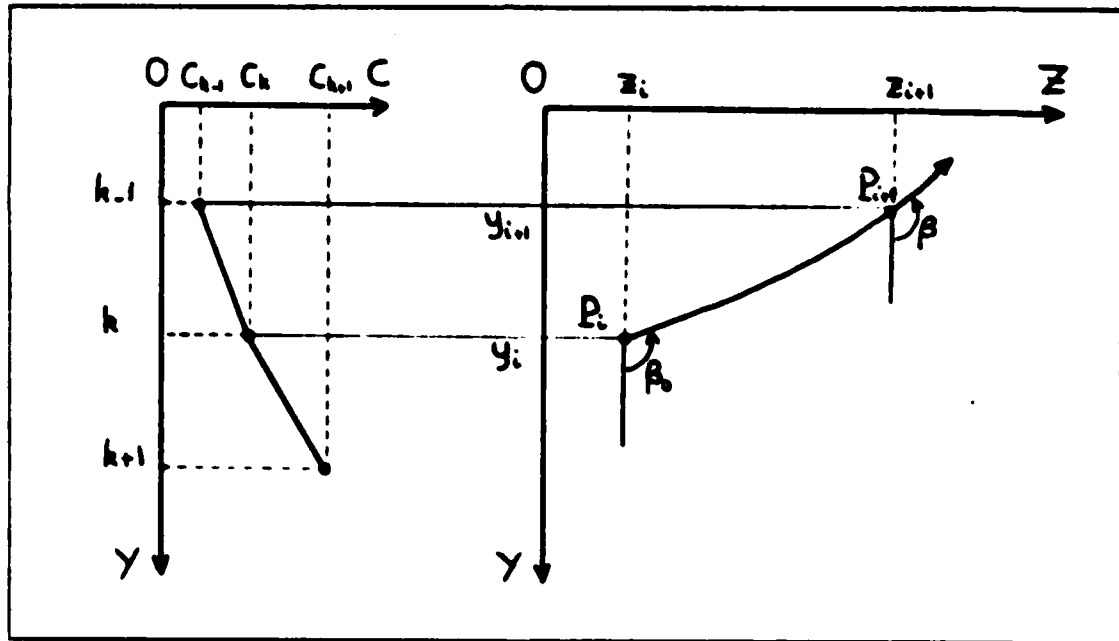


Figure 2.3 Parameters describing a one-meter-depth increment positive gradient sound-speed profile for an upward travelling acoustic ray path.

Now we are going to examine in detail the different cases occurring in the subroutine leading to some IF...THEN...ELSE... statements, depending on the sign of the gradient (or the curvature) and the upward or downward direction of the ray at the i^{th} point.

1. Case 1 : $g_{k-1} > 0, g_k > 0$.

At the i^{th} point of the ray path P_i , corresponding to the depth index k , the gradient above is (see Figure 2.4)

$$g_{k-1} = c_k - c_{k-1} \quad (2.21)$$

and the gradient below is

$$g_k = c_{k+1} - c_k \quad (2.22)$$

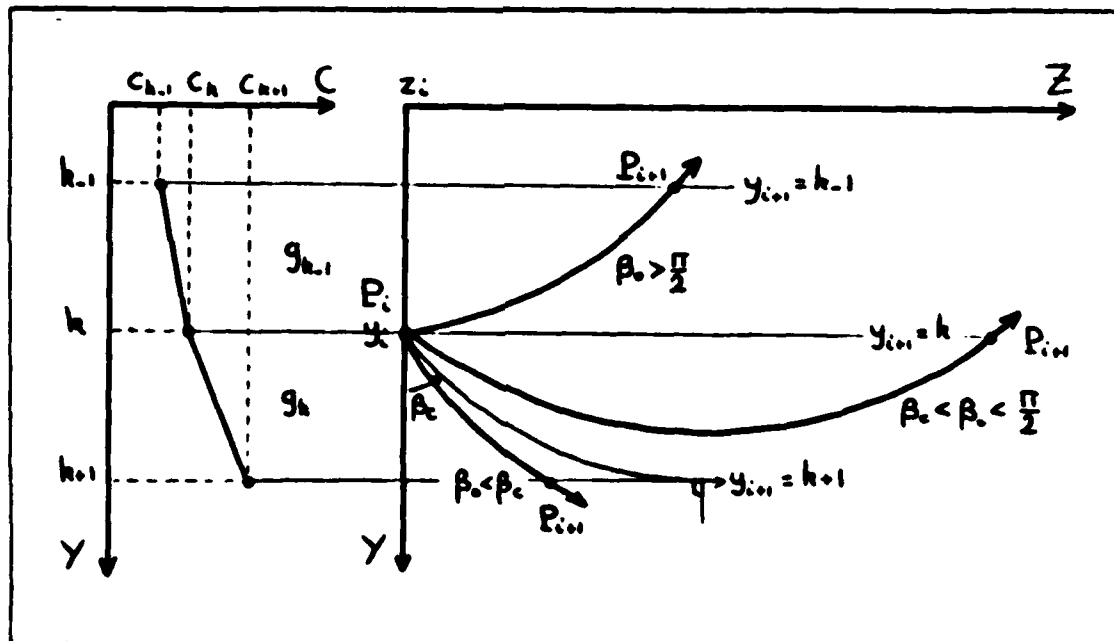


Figure 2.4 Case 1 : $g_{k-1} > 0, g_k > 0$.

We have three different cases to consider depending on the value of β_0 with regard to $\pi/2$ and β_c . The critical angle β_c is the value of the initial angle of propagation at P_i leading to a final angle $\beta = \pi/2$ one meter deeper, that is, leading to a turning point one meter deeper.

According to Snell's law,

$$\sin\beta_c = \frac{c_k}{c_{k+1}} \quad (2.23)$$

or

$$\beta_c = \arcsin \frac{c_k}{c_{k+1}} . \quad (2.24)$$

Let us examine the three cases $\beta_0 > \pi/2$, $\beta_0 < \beta_c$ and $\beta_c < \beta_0 < \pi/2$ since a strict equality does not apply for real numbers in FORTRAN language.

a. $\beta_0 > \pi/2$:

According to (2.3) and since the ARCSIN function gives a result between 0 and $\pi/2$, the angle of propagation at P_{i+1} is :

$$\beta = \pi - \arcsin(bc_{k-1}) . \quad (2.25)$$

Substituting for β in (2.12), we get the coordinates of the next point P_{i+1} :

$$y_{i+1} = k-1 \quad (2.26)$$

and

$$z_{i+1} = z_i + \frac{1}{b\beta_{k-1}} \{ \cos\beta_0 + \cos[\arcsin(bc_{k-1})] \} \quad (2.27)$$

with

$$b = \sin\beta_{\text{source}} / c_{\text{source}} . \quad (2.28)$$

b. $\beta_0 < \beta_c$:

This time, using the same equations (2.3) and (2.12) at the point P_{i+1} , we have :

$$\beta = \arcsin(bc_{k+1}) , \quad (2.29)$$

$$y_{i+1} = k+1 . \quad (2.30)$$

and

$$z_{i+1} = z_i + \frac{1}{bg_k} \{ \cos\beta_0 - \cos[\arcsin(bc_{k+1})] \} . \quad (2.31)$$

c. $\beta_c < \beta_0 < \pi/2$:

In this case, we have to deal with a turning point within the segment $P_i P_{i+1}$.

Let us derive the general formula for computing z_{i+1} when a turning point is encountered. This formula will be used when we study the cases generated by the other sign possibilities of the gradient g .

Applying (2.12) first from P_0 to P' , then from P' to P we have (see Figure 2.5) :

$$z' = z_0 + \frac{1}{bg} (\cos\beta_0 - \cos\pi/2) \quad (2.32)$$

and

$$z = z' + \frac{1}{bg} [\cos\pi/2 - \cos(\pi - \beta_0)] . \quad (2.33)$$

or

$$z' = z_0 + \frac{1}{bg} \cos \beta_0 \quad (2.34)$$

and

$$z = z' + \frac{1}{bg} \cos \beta_0 \quad (2.35)$$

Substituting (2.34) in (2.35) yields

$$z = z_0 + \frac{2}{bg} \cos \beta_0 \quad (2.36)$$

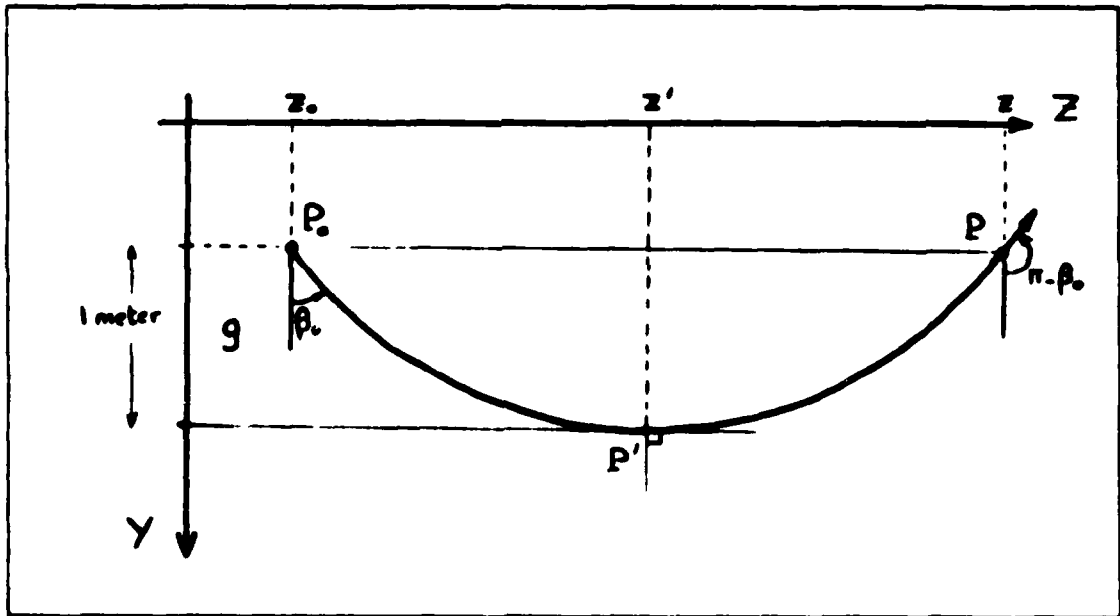


Figure 2.5 Turning point treatment.

Going back to our case of interest and using (2.36), we get the coordinates of P_{i+1} :

$$y_{i+1} = y_i = k \quad (2.37)$$

$$y_{i+1} = k+1, \quad (2.41)$$

and

$$z_{i+1} = z_i + \frac{1}{bg_k} \{ \cos\beta_0 - \cos[\arcsin(bc_{k+1})] \}. \quad (2.42)$$

b. $\beta_0 > \beta_c$:

$$\beta = \pi - \arcsin(bc_{k-1}), \quad (2.43)$$

$$y_{i+1} = k-1, \quad (2.44)$$

and

$$z_{i+1} = z_i + \frac{1}{bg_{k-1}} \{ \cos\beta_0 + \cos[\arcsin(bc_{k-1})] \}. \quad (2.45)$$

c. $\pi/2 < \beta_0 < \beta_c$:

$$y_{i+1} = y_i = k \quad (2.46)$$

and

$$z_{i+1} = z_i + \frac{2}{bg_{k-1}} \cos\beta_0. \quad (2.47)$$

3. Case 3: $g_{k-1} > 0, g_k < 0$

According to Figure 2.7, we now have only two separate cases to consider, depending on the value of β_0 with regard to $\pi/2$. Returning to the two previous cases, we will find some similarities.

a. $\beta_0 > \pi/2$:

This case is similar to case 1.a, and equations (2.25), (2.26), and (2.27) apply.

b. $\beta_0 < \pi/2$:

This case is similar to case 2.a, and equations (2.40), (2.41), and (2.42) apply.

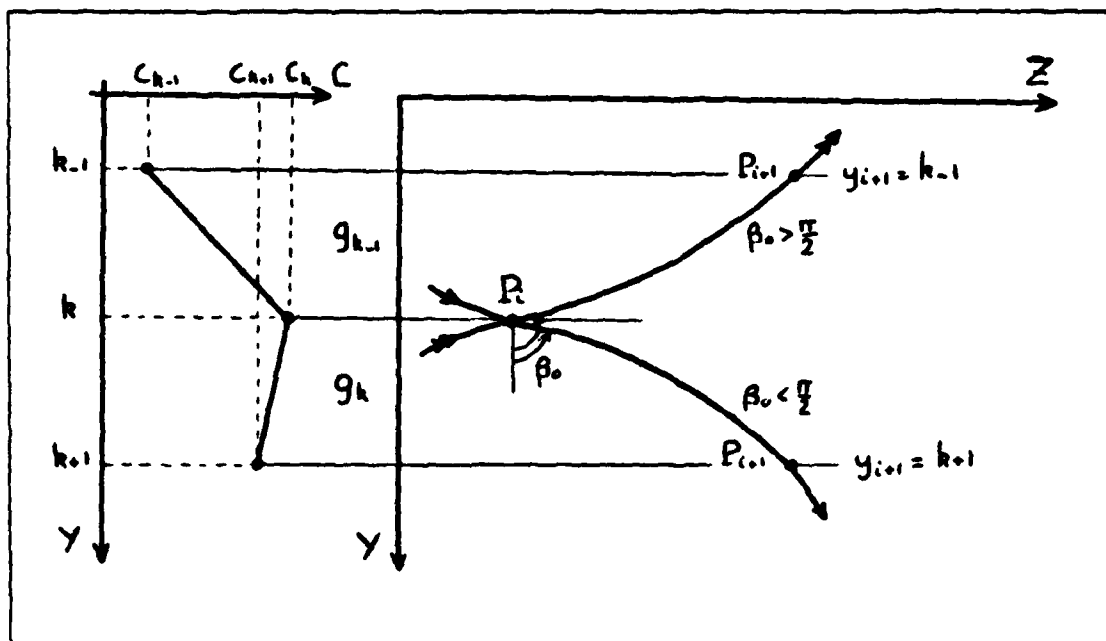


Figure 2.7 Case 3 : $g_{k-1} > 0, g_k < 0$.

4. Case 4 : $g_{k-1} < 0, g_k > 0$

According to Figure 2.8, we now have four different cases to examine with two possibilities for β_c .

$$\beta_c = \pi - \arcsin \frac{c_k}{c_{k-1}} \quad (2.48)$$

or

$$\beta_c = \arcsin \frac{c_k}{c_{k+1}} \quad (2.49)$$

5. Surface and bottom reflections

The last point we need to discuss is how to handle surface and bottom reflections, that is, when the depth index k reaches the values of 0 or N . The value N corresponds to the maximum depth given in the profile and is assumed to be the depth of the sea floor. In the case where the sound-speed profile does not extend to the bottom, it is always possible to extrapolate the sound-speed profile to the bottom using the gradient of the profile corresponding to the last straight line segment or, using an average value given by the climatology.

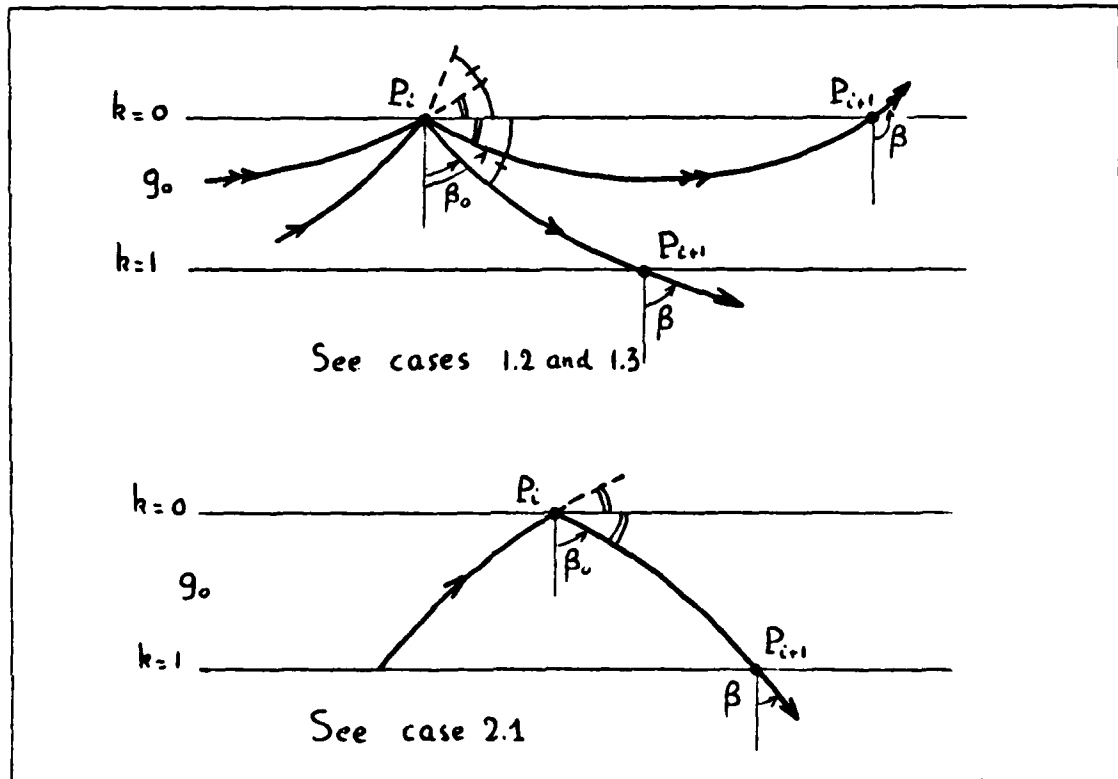


Figure 2.9 Perfect surface reflection possibilities.

a. Surface reflection

In this simple acoustic model, we assume a perfect surface reflection. Thus, when the depth index k reaches the value 0, we just have to maintain symmetry (i.e., the angle of reflection is equal to the angle of incidence) with regard to the horizontal to get the correct angle β_0 before applying the same equations as in cases 1.b, 1.c and 2.a of Figure 2.9.

b. Bottom reflection

Following the same idea, we assume a perfect bottom reflection. Thus when the depth index k reaches its maximum value N , we maintain symmetry (i.e., the angle of reflection is equal to the angle of incidence) with regard to the horizontal (see Figure 2.10).

Notice that the fictitious gradients g_{-1} and g_N have been created in the program to handle the cascade of IF...THEN...ELSE... statements.

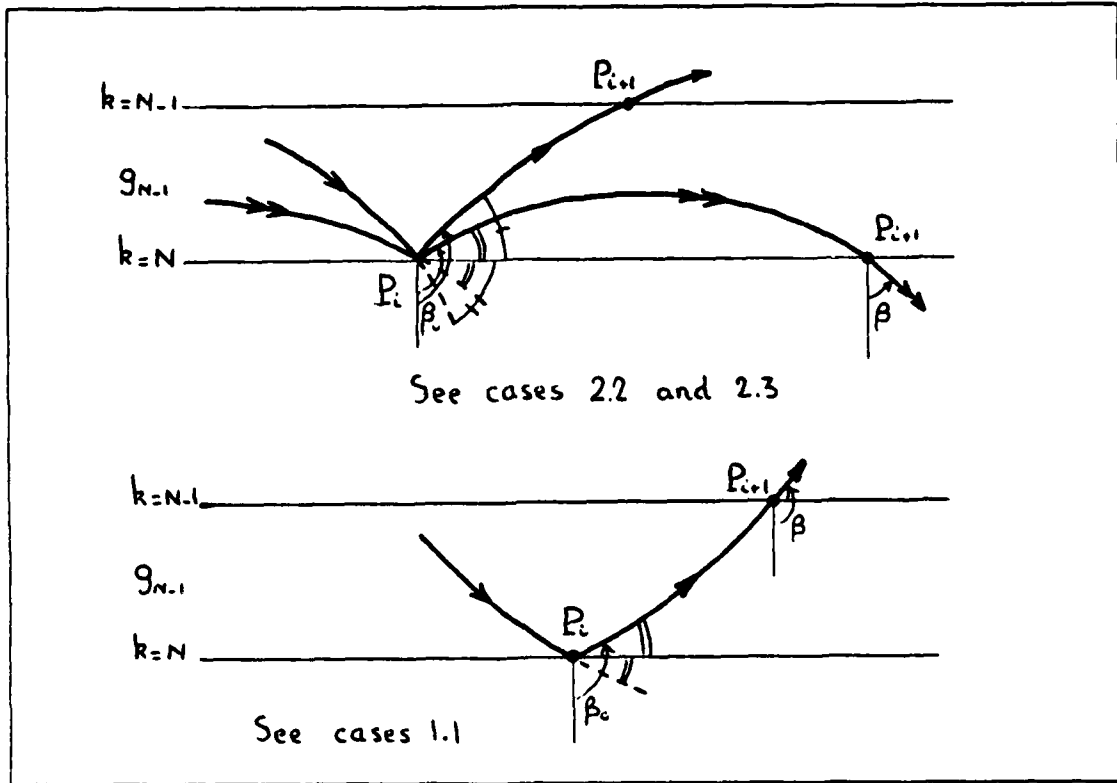


Figure 2.10 Perfect bottom reflection possibilities.

D. SUMMARY AND DIRECTIVES TO USE THE SUBROUTINE RAY

1. Main characteristics

The computation in the subroutine RAY is based on representing an arbitrary sound-speed profile by straight line segments in one-meter depth increments and thus allows the use of any complicated sound-speed profile to obtain a precise and smooth acoustic ray trace.

A plot of the sound-speed profile is provided at the same time as the plot of the bundle of rays.

The main assumptions underlying this program are the following :

- perfect surface reflection,
- perfect bottom reflection,
- flat bottom.

2. Features of this subroutine

This subroutine uses many DISSPLA graphics statements. Hence, the main program calling subroutine RAY has to be executed using the command DISSPLA. A choice of multiple display devices is provided to the user through the use of comment cards in front of the statements CALL COMPRS, CALL TEK618, or CALL CX41(4107).

The variables required when using RAY are the following :

- Y0 : depth of the source in meters,
- M : number of ray path desired,
- BET : array (size M) of the initial angles of propagation β_{source} in degrees,
- B0 : initial angle of the upper ray of the bundle,
- DB : increment of initial angles in BET,
- MM + 1 : number of points in the provided sound-speed profile,
- CC : provided values of sound speed in m/sec,
- YY : corresponding depth in meters,
- RANGE : maximum range desired in kilometers,
- NN : index of range,
- Y : array (size NN) of depth in meters,
- Z : array (size NN) of horizontal distances in kilometers,
- N : integer value of the depth of the sea floor in meters,
- C : array (size N) of sound speed (m/sec),
- G : array (size N) of its gradient (sec^{-1}),
- YC : array (size N) of depths (meters).

The bundle of rays to be traced is defined by the number of rays M, the initial angle B0 of the upper ray of the bundle, and the angle increment DB between two rays. Inside the subroutine, we can also set different equations to define a bundle of rays. And finally, by deleting these few lines involved with these computations, we can provide our own array BET of initial angles β_{source} .

No relation has been derived between NN and the maximum range RANGE since this relation depends on many different parameters such as the β_{source} 's, the sound-speed profile, and the maximum range. If during a plot a ray ends before reaching the right side of the graph (especially the steepest rays), a higher number NN has to be set. For instance, a value NN = 5000 seems to handle most of the reasonable steep β_{source} given for a maximum range of 30 km.

The arrays Y and Z have been created for computing and plotting the ray paths and the arrays C, G and YC are for plotting the sound-speed profile.

3. Example

A result of the RAY subroutine is displayed in Figure 2.11. The provided parameters and sound-speed profile are listed in Table 1 .

TABLE 1
PARAMETERS AND DATA USED IN THE EXAMPLE
OF SUBROUTINE RAY SHOWN IN FIGURE 2.11

Y0	30.	YY	0.	CC	1482.
M	10		30.		1482.9
NN	5000		55.		1484.1
RANGE	30.		90.		1480.5
N	300		150.		1482.0
MM	6		225.		1484.1
			300.		1486.2

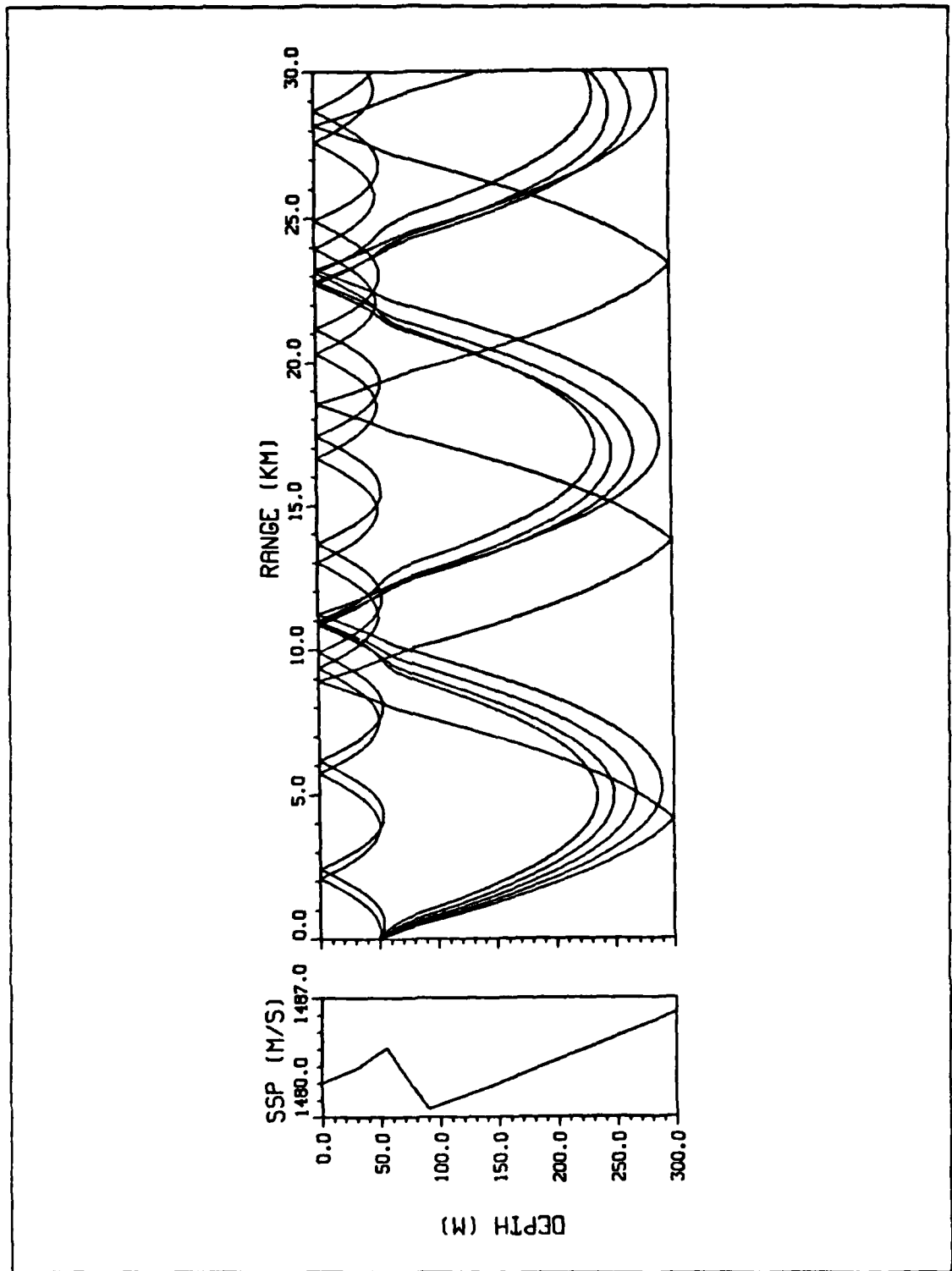


Figure 2.11 Ray tracing provided by subroutine RAY.

III. OCEAN MIXED LAYER MODEL

A. INTRODUCTION

The study of the oceanic turbulent boundary layer is a relatively recent field in Physical Oceanography. The model used for this research has been developed by Garwood [Refs. 1,5]. These papers give the formulation of a unified mathematical model of the one-dimensional, non-stationary, oceanic turbulent boundary layer.

The study of these top few tens of meters of the ocean is of considerable scientific interest. It influences and can be related to the general circulation of the ocean [Ref. 6]. The thermal structure associated with this boundary layer must be considered when making medium and long-range weather forecast, since a large part of the atmospheric energy supply comes from the heat exchanged with the ocean. This layer is also a region of primary biological productivity, which is of significant ecological and economic importance. Finally, as an important military application, this study can be used in the modeling of acoustic propagation in the ocean, which is the goal of this research.

1. Characteristics of the oceanic mixed layer

The oceanic mixed layer is that fully turbulent region of the upper ocean that is bounded above by the air-sea interface and below by a dynamically stable water mass. The wind and intermittent upward surface buoyancy flux through the surface (surface cooling at night or in winter time for example) are the sources of mechanical energy for the generation of these turbulences. Figure 3.1 gives a general picture idealizing density and mean velocity profiles of the ocean mixed layer.¹

2. Generalities on the dynamics of the mixing

The depth of the ocean wind-mixed surface layer is typically on the order of ten to one hundred meters. The horizontal scale size is that of the internal Rossby radius, typically 20 to 50 km. These two dominant scale sizes are much smaller than the horizontal scale size of the driving meteorological disturbances, water mass features, and distances to lateral boundaries. The approximation of local horizontal

¹In this chapter, in order to be consistent with the notation used in [Refs. 1,5] as in most of the geophysical sciences publications, we chose z to be the upward vertical axis and (x,y) to be the horizontal coordinates as depicted in Figure 3.1. The vertical component of the fluid velocity will be w and the horizontal components will be u and v .

homogeneity for all mean variables is usually accurate and is a basic assumption in this model.

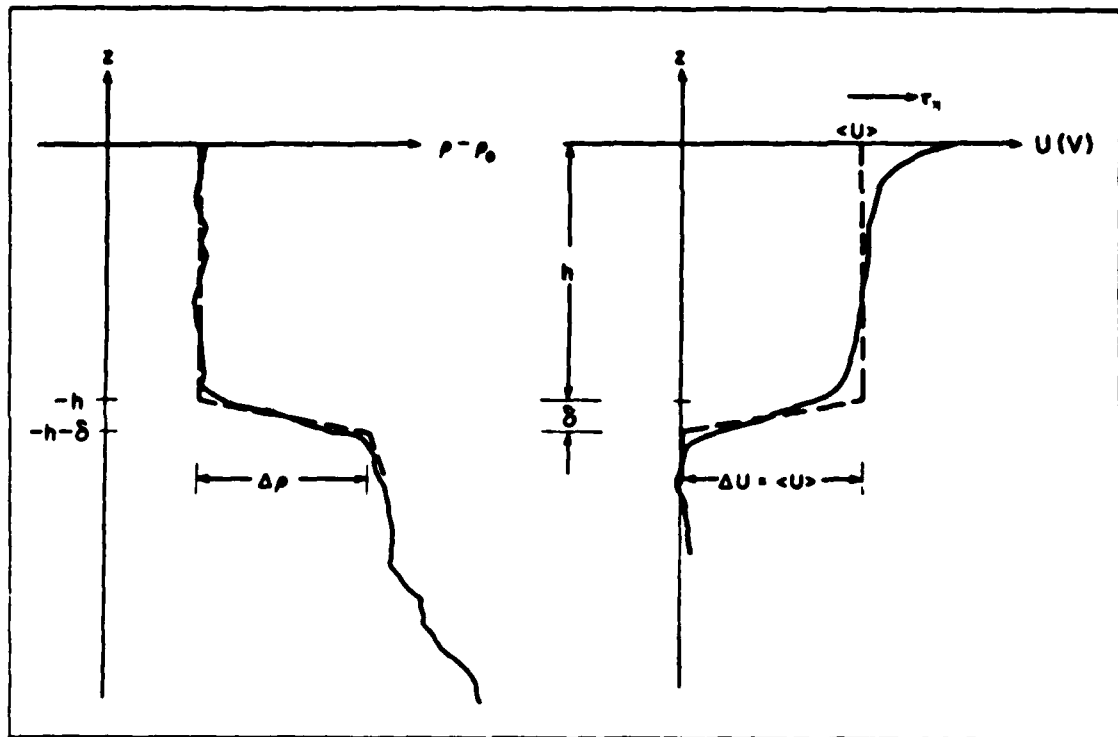


Figure 3.1 Idealized model for ocean mixed layer..

A sharp density discontinuity of thickness δ (see Figure 3.1) separates the layer from a stable non turbulent thermocline. Minimal stress at the bottom together with high turbulence intensity leads also to an approximate vertical uniformity in mean velocity and density. We shall note that only small gradients in these mean variables give rise to large turbulent fluxes.

The mechanical energy budget for the ocean mixed layer is depicted in Figure 3.2. Deepening of the mixed layer is accomplished by entrainment of the more dense underlying water into the turbulent region above. This process leads to a potential energy increase and cannot take place without an energy source: the turbulent kinetic energy of the mixed layer above.

Retreat occurs when the vertical component of the turbulence is insufficient to transport heat, momentum, and turbulence to an earlier-established depth of mixing. This happens when downward heat flux (buoyant damping) and dissipation effects

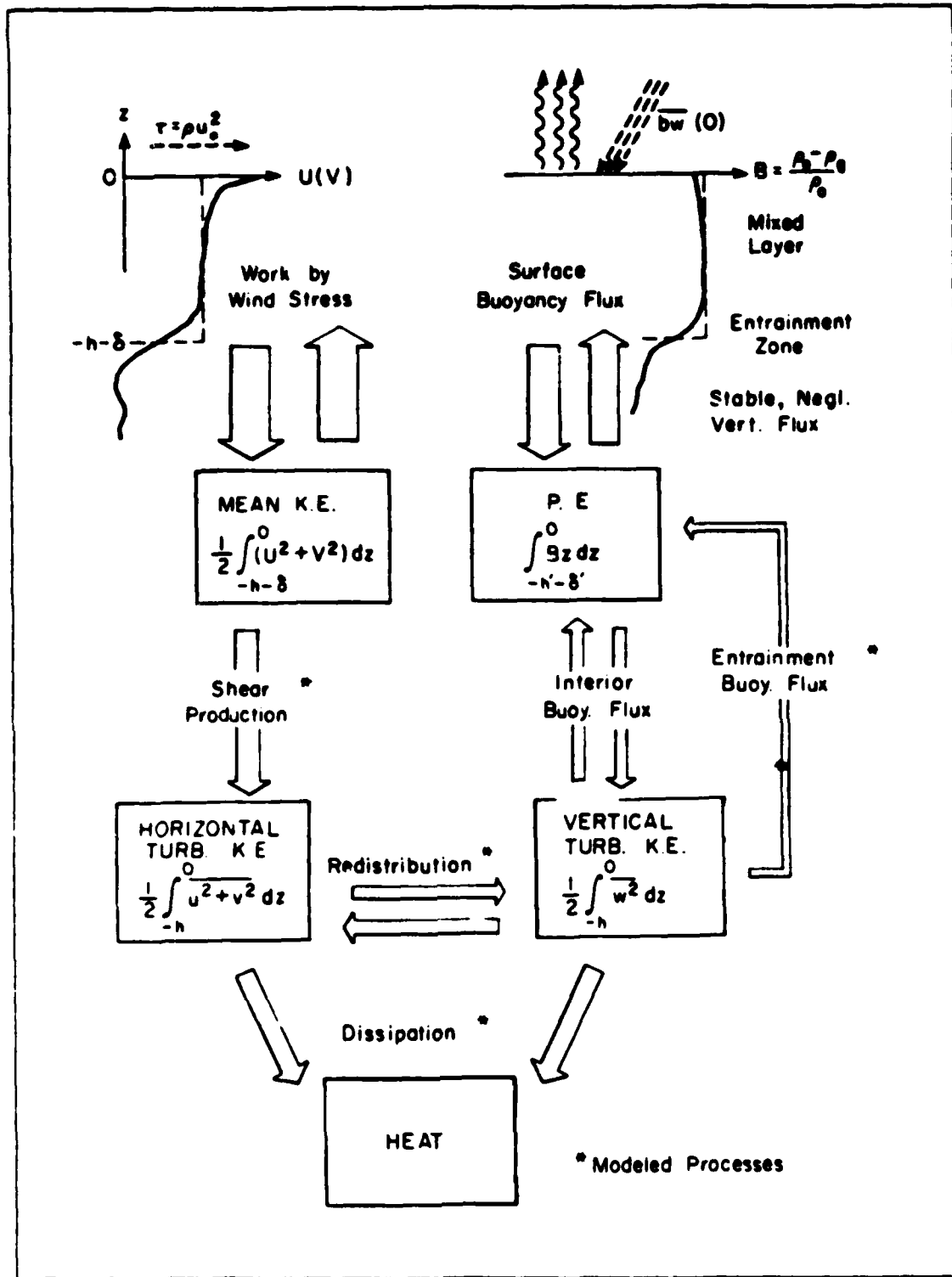


Figure 3.2 Mechanical energy budget for the ocean mixed layer.

exceed the wind-stirring shear-production of turbulence, creating a stratification of the upper ocean.

Thermal energy and mechanical energy received from the atmosphere not only control the local dynamics, but the layer itself modulates the flux of this energy to the deeper water masses. Entrainment also converts some of the mean flow energy into turbulent energy, over and above the wind-stress production.

Finally, substantial barotropic and baroclinic features, such as tidal motion and internal waves, can be linearly superimposed. The mean fields of concern are therefore the horizontally homogeneous components of the total fields.

3. The model and its features not previously demonstrated

The vertical and horizontal components of the turbulent kinetic energy (TKE) are determined implicitly, along with layer depth, mean momentum, and mean buoyancy. Layer growth and retreat are predicted.

Specific features of the TKE budget include mean turbulent field modeling of the dissipation term, the energy redistribution term, and the term for the convergence of buoyancy flux at the stable interface as shown in a following section. Then an entrainment hypothesis dependent upon the relative distribution of the TKE between horizontal and vertical components permits the closure of the system of equations.

The model differs from earlier models in the following ways. First, the amount of wind generated TKE to be used in mixing is a function of the ratio of the mixed layer depth to the Obukhov mixing length L . Second, viscous dissipation is dependent on a local Rossby number. Finally, separate vertical and horizontal equations for TKE are used, permitting a more consistent interpretation of both entraining and retreating mixed layers.

B. FORMULATION OF THE EQUATIONS USED IN THIS OBL MODEL

1. Generalities

The underlying principles employed in studying the mixed layer are the combined conservation of mass, momentum, thermal energy, and mechanical energy. Most of the physics behind such a one-dimensional model is based on the flux form of the Navier-Stokes equations with the Boussinesq approximation. The horizontal homogeneity mentioned previously permits the neglect of the horizontal gradients of the mean fields.

Conservation of buoyancy is employed as a generalization of the conservation of heat alone. The buoyancy equation is generated from the heat and salt equations together with an equation of state,

$$\rho = \rho_0 [1 - \alpha(\theta - \theta_0) + \beta(s - s_0)] . \quad (3.1)$$

and the definition for buoyancy,

$$b = g(\rho_0 - \rho) / \rho_0 . \quad (3.2)$$

where ρ_0 is a representative density at the time and location of consideration, g is acceleration due to gravity, α and β are the expansion coefficients for heat and salt.

All variables are separated into mean and fluctuating components :

• temperature	$\theta = T + T'$
• salinity	$s = S + s'$
• pressure	$p = P + p'$
• velocities	$u = U + U + u'$
	$v = V^g + V + v'$
	$w = W^g + w'$
• buoyancy	$b = B + b'$

Subscript g denotes geostrophic components.

2. Mean buoyancy and momentum equations

The first law of thermodynamics for an incompressible fluid and the conservation of salt mass, neglecting molecular fluxes, lead to the mean buoyancy equation :

$$\partial B / \partial t = -\partial \overline{b'w'} / \partial z + \alpha g Q / \rho_0 C_p . \quad (3.3)$$

By invoking the Boussinesq approximation, dropping the negligible viscous terms, assuming incompressibility, and subtracting the geostrophic equations from the total momentum equations, we obtain the mean momentum equations :

$$\partial U / \partial t = fV - \partial \overline{u'w'} / \partial z \quad (3.4)$$

$$\partial V / \partial t = -fU - \partial \overline{v'w'} / \partial z . \quad (3.5)$$

Integration of (3.3), (3.4) and (3.5) over the entrainment zone from $z = -h-\delta$ to $z = -h$ leads to the jump conditions for the turbulent fluxes at the bottom of the mixed layer :

$$-\overline{b'w'}(-h) = \Delta B \partial h / \partial t \quad (3.6)$$

$$-\overline{u'w'}(-h) = \Delta U \partial h / \partial t \quad (3.7)$$

$$-\overline{v'w'}(-h) = \Delta V \partial h / \partial t \quad (3.8)$$

where

$$b' = \alpha g T' - \beta g s' \quad (3.9)$$

and

$$\Delta B = \alpha g \Delta T - \beta g \Delta S \quad (3.10)$$

The assumption of vertical homogeneity in the mixed layer permits the integration of (3.3), (3.4) and (3.5) from $z = -h-\delta$ to $z = 0$, including the effects of entrainment stresses (3.7) and (3.8), and entrainment buoyancy flux (3.6). This yields the bulk relationships for mean buoyancy :

$$h \partial \langle B \rangle / \partial t + \Lambda \Delta B \partial h / \partial t = \alpha g Q_0 / \rho_0 C_p - \overline{b'w'}(0) \quad (3.11)$$

$$h \partial \langle U \rangle / \partial t + \Lambda \Delta U \partial h / \partial t = -h \langle V \rangle - \overline{u'w'}(0) \quad (3.12)$$

$$h \partial \langle V \rangle / \partial t + \Lambda \Delta V \partial h / \partial t = -h \langle U \rangle - \overline{v'w'}(0) \quad (3.13)$$

where

$$Q_0 = Q_s - (Q_e + Q_h + Q_b) \text{ in } W/m^2. \quad (3.14)$$

The value of Q_0 is the net solar irradiance at the surface, minus the long wave back radiation, minus the sensible heat flux, minus the latent heat flux.

The function Λ is the Heaviside step function :

$$\Lambda = 1 \text{ if } \partial h / \partial t > 0 ,$$

$$\Lambda = 0 \text{ if } \partial h / \partial t \leq 0 .$$

The brackets $\langle \rangle$ denotes a vertical mean through the mixed layer,

$$\langle \rangle = \frac{1}{h+\delta} \int_{-h-\delta}^0 () dz \quad (3.15)$$

and $\overline{\quad}$ denotes horizontal mean,

$$\overline{()} = \frac{1}{xy} \int_x \int_y () dx dy . \quad (3.16)$$

As the time step used in the model is one hour, the surface boundary conditions are prescribed hourly :

$$-\overline{u'w'}(0) = \tau_x(t) \rho_0 \quad (3.17)$$

$$-\overline{v'w'}(0) = \tau_y(t) \rho_0 \quad (3.18)$$

$$-\overline{b'w'}(0) = g [\beta \overline{s'w'}(0,t) - \alpha \overline{w'T'}(0,t)] \quad (3.19)$$

with

$$\tau = \rho_a C_d U_{10}^2 \quad (3.20)$$

where ρ_a is the air density, C_d a drag coefficient and U_{10} the wind speed at 10 meters, and with

$$\overline{s'w'}(0) = S(E - P) \quad (3.21)$$

where $E - P$ = evaporation minus precipitation in cm/sec.

3. Mean turbulent kinetic energy equation

Subtracting the scalar product of (u, v, w) with the mean momentum equations from the mean equation for the total mechanical energy yields the mean TKE equation:

$$\frac{1}{2} \frac{\partial \overline{E}}{\partial t} = -[\overline{u'w'} \frac{\partial U}{\partial z} + \overline{v'w'} \frac{\partial V}{\partial z}] + \overline{b'w'} - \frac{\partial}{\partial z} [\overline{w'(\frac{p'}{\rho_0} + \frac{E}{2})}] - \epsilon \sim 0 \quad (3.22)$$

where (I) (II) (III) (IV)

$$E = u'^2 + v'^2 + w'^2. \quad (3.23)$$

The budgets for the individual components of TKE can also be formed :

$$\frac{1}{2} \frac{\partial \overline{u'^2}}{\partial t} = -\overline{u'w'} \frac{\partial U}{\partial z} - \frac{\partial}{\partial z} (\frac{\overline{w'u'^2}}{2}) + \frac{\overline{p'\partial u'}}{\rho_0 \partial x} - \frac{\epsilon}{3} + \Omega_3 \overline{u'v'} - \Omega_2 \overline{u'w'} \quad (3.24)$$

$$\frac{1}{2} \frac{\partial \overline{v'^2}}{\partial t} = -\overline{v'w'} \frac{\partial V}{\partial z} - \frac{\partial}{\partial z} (\frac{\overline{w'v'^2}}{2}) + \frac{\overline{p'\partial v'}}{\rho_0 \partial y} - \frac{\epsilon}{3} - \Omega_3 \overline{u'v'} \quad (3.25)$$

$$\frac{1}{2} \frac{\partial \overline{w'^2}}{\partial t} = \overline{b'w'} - \frac{\partial}{\partial z} (\frac{\overline{w'^3}}{2} + \frac{\overline{w'p'}}{\rho_0}) + \frac{\overline{p'\partial w'}}{\rho_0 \partial z} - \frac{\epsilon}{3} + \Omega_2 \overline{u'w'} \quad (3.26)$$

(V) (IV)

where $\Omega = (\Omega_1, \Omega_2, \Omega_3)$ is the rotation vector for the earth.

The time rate of change of TKE is usually smaller than the other terms and may be neglected. The term (I) represents the rate of mechanical production and is the dominant source of TKE. It is the rate of conversion of mean to TKE by the down-

gradient turbulent flux of momentum. The term (II) represents the buoyancy flux and can be either a source or a sink. This term can become an important source as in the case of strong convective cooling in the autumn. The term (III) is the divergence of the turbulent flux of TKE or turbulent diffusion of itself. Locally, at the bottom of the layer during occasions of entrainment, a net convergence of flux of energy is necessary to maintain the downward buoyancy flux for deepening the mixed layer. The term (IV) represents viscous dissipation. Because local isotropy is assumed for the dissipation range, ϵ is divided equally among the component budgets. The terms (V) are very important terms which sum to zero by continuity in the TKE equation. They cause a redistribution of energy among u'^2 , v'^2 and w'^2 . The terms (VI) are also redistribution terms, but they are due to rotation of the earth. In this study, we will neglect them because of the usually short integral time scale in comparison with the time periods of interest.

Assumption of vertical homogeneity in the mixed layer permits the vertical integration from $z = -h-\delta$ to $z = 0$ of (3.24)+(3.25) and (3.26). By this step we introduce a new variable h , the depth of the mixed layer.

Up to that point, if we set q^2 , the horizontal component of TKE, such as

$$q^2 = u'^2 + v'^2, \quad (3.27)$$

we have six variables h , $\langle B \rangle$, $\langle U \rangle$, $\langle V \rangle$, $\langle \overline{w'^2} \rangle$ and $\langle \overline{q^2} \rangle$ for five equations (3.11), (3.12), (3.13), vertical integral of (3.24)+(3.25) and (3.26). Therefore a sixth equation is needed to close the system. Besides, we also need a suitable modeling of the different terms of the integrated TKE equation. Following Garwood's arguments [Refs. 1,5], a synthesis of these derivations is given in the next sections.

4. Modeling of the different terms of the integrated TKE equation

a. Shear production and turbulent diffusion

The vertical integral of terms (I) and (III) may be combined to give the net "wind-generated" rate of production :

$$G = \int_{-h-\delta}^0 [(I) + (III)] dz \quad (3.28)$$

or

$$G = m_3 u^{*3} + 1/2 [(\Delta U)^2 + (\Delta V)^2] \partial h / \partial t \quad (3.29)$$

where u^* is the friction velocity defined as :

$$u^* = [\overline{u'v'}(0)^2 + \overline{v'w'}(0)^2]^{1/2} . \quad (3.30)$$

b. Net buoyant damping

The integral of (II) over the mixed layer gives the net buoyant damping for the whole layer :

$$B = \int_{-h-\delta}^0 (II) dz \quad (3.31)$$

or

$$B = \frac{h}{2} [\Delta B \frac{\partial h}{\partial t} - \overline{b'w'}(0)] + \frac{\alpha g}{\rho_0 C_p} \int_{-h-\delta}^0 \left[\frac{Qh}{2} - \int_z^0 Q d\lambda \right] dz \quad (3.32)$$

which can be rewritten as

$$B = 1/2 h \overline{b'w'}(-h) - 1/2 h u^* b^* \quad (3.33)$$

where $u^* b^*$ is the downward surface flux of buoyancy :

$$b^* u^* = -\overline{b'w'}(0) + \alpha g \rho_0 C_p R Q_s [1 + e^{-\gamma h (1 + 2\gamma h)} - 2\gamma h] . \quad (3.34)$$

The radiation absorption $Q(z)$ has been modeled as

$$Q = \gamma R Q_s e^{\gamma z} \quad (3.35)$$

where γ is the extinction coefficient for net solar radiation, and $R Q_s$ is the short wave fraction of the net solar irradiance. This model assumes that the net long-wave solar radiation is absorbed at the surface, which leads to :

$$-\overline{b'w'}(0) = \alpha g \rho_0 C_p [(1-R) Q_s - (Q_e + Q_b + Q_h)] + \beta g S (P-E) \quad (3.36)$$

where $(1-R)Q_s$ corresponds to the short-wave incoming radiation. On the other hand, the short-wave radiation penetrates below the surface where it is absorbed following the exponential decay (3.35).

c. Viscous dissipation

For a fully turbulent mixed layer, viscous dissipation of the turbulence occurs primarily in the small eddies which are locally isotropic. The net rate of dissipation is modelled as follows:

$$D = \int_{h-\delta}^0 \varepsilon \, dz = m_1 \langle \bar{E} \rangle^{3/2} + m_5 f h \langle \bar{E} \rangle \quad (3.37)$$

or

$$D = m_1 \langle \bar{E} \rangle^{3/2} (1 + R_0^{-1} m_5 / m_1 u^* / \langle \bar{E} \rangle^{1/2}) \quad (3.38)$$

where $R_0 = u^*/hf$ is a Rossby number for the turbulent boundary layer. The first term in D arises from the fact that the time scale of the largest eddies can be proportional to the mixed layer depth divided by the rms turbulent velocity $\langle \bar{E} \rangle^{1/2}$. The second one comes from the assumption that, in deeper boundary layers, planetary rotation (time scale $1/f$) turns the mean shear direction with depth and thus influences the geometrical aspects of the integral scale.

d. Redistribution of TKE

The vertical integral of the pressure redistribution term

$$R_i = \int_{h-\delta}^0 \frac{\overline{p' \partial u_i}}{\rho_0 \partial x_i} \, dz \quad (3.39)$$

is an important source or sink term for the individual TKE budgets, even though $R_1 + R_2 + R_3 = 0$. The bulk formulation is

$$R_i = m_2 \langle \bar{E} \rangle^{1/2} (\langle \bar{E} \rangle - 3 \langle u_i'^2 \rangle). \quad (3.40)$$

The rotational redistribution terms are assumed to be of higher order, and are neglected in this study.

5. Closure hypothesis

Garwood [Ref. 1] achieves closure of the problem by formulating the following entrainment equation :

$$\partial h / \partial t = m_4 \langle w'^2 \rangle^{1/2} \langle \bar{E} \rangle / h \Delta B . \quad (3.41)$$

C. SUMMARY OF MODELED EQUATIONS

We have six variables h , $\langle B \rangle$, $\langle U \rangle$, $\langle V \rangle$, $\langle \overline{w'^2} \rangle$, $\langle \overline{q^2} \rangle$ and a final set of six equations :

- mean momentum equations :

$$h \partial \langle U \rangle / \partial t + \Lambda \Delta U \partial h / \partial t = -fh \langle V \rangle - \overline{u'w'}(0) \quad (3.42)$$

$$h \partial \langle V \rangle / \partial t + \Lambda \Delta V \partial h / \partial t = -fh \langle U \rangle - \overline{v'w'}(0) \quad (3.43)$$

- mean buoyancy equation :

$$h \partial \langle B \rangle / \partial t + \Lambda \Delta B \partial h / \partial t = \alpha g Q_0 / \rho_0 C_p - \overline{b'w'}(0) \quad (3.44)$$

- horizontal integrated TKE component :

$$\frac{1}{2} \frac{\partial}{\partial t} (h \langle \overline{q^2} \rangle) = m_3 u^{*3} + \frac{(\Delta U)^2 + (\Delta V)^2}{2} \frac{\partial h}{\partial t} \quad (3.45)$$

$$- m_2 (\langle \bar{E} \rangle - 3 \langle \overline{w'^2} \rangle) \langle \bar{E} \rangle^{1/2} - 2m_1/3 (\langle \bar{E} \rangle^{1/2} + m_5/m_1 fh) \langle \bar{E} \rangle$$

- vertical integrated TKE component :

$$\frac{1}{2} \frac{\partial}{\partial t} (h \langle \overline{w'^2} \rangle) = 1/2 h \overline{b'w'}(-h) - 1/2 h u^* b^* + m_2 (\langle \bar{E} \rangle - 3 \langle \overline{w'^2} \rangle) \langle \bar{E} \rangle^{1/2} \quad (3.46)$$

$$- m_1/3 (\langle \bar{E} \rangle^{1/2} + m_5/m_1 fh) \langle \bar{E} \rangle .$$

- entrainment equation :

$$\partial h / \partial t = m_4 \langle \overline{w'^2} \rangle^{1/2} \langle \overline{E} \rangle / h \Delta B . \quad (3.47)$$

The different constants used in the model are the following :

- ρ_a Representative density of air
- ρ_0 Representative density of sea-water
- α, β Coefficients of thermal expansion
- g Gravitational acceleration
- C_p Specific heat at constant pressure
- C_d Drag coefficient
- f Coriolis parameter depending on latitude

We can tune the model by specifying the different parameters m_1, m_3, m_4, m_5 as well as the extinction coefficient for net solar radiation γ , and the short-wave fraction of the solar radiation R .

Initial profiles of temperature $T(z)$ ($^{\circ}\text{C}$ vs cm) and salinity $S(z)$ (g/kg vs cm) have to be provided. The depth increment in the model is 100 cm . Finally, as the time step is one hour, the following boundary conditions have to be prescribed hourly :

- τ Wind stress in dynes/cm^2
- Q_s Incoming solar radiation in W/m^2
- Q_b Back radiation in W/m^2
- Q_e Latent heat flux
- Q_h Sensible heat flux
- E Evaporation in mm/hour
- P Precipitation in mm/hour

The values of u^* and u^*b^* can be computed using equations (3.17), (3.18), (3.30), (3.37) and (3.36).

IV. COUPLING THE TWO MODELS

A. GENERALITIES

The goal of this research is to couple the Oceanic Boundary Layer (OBL) model derived by Garwood in 1977 with an acoustic ray tracing program allowing us to analyze some effects of the atmospheric factors on the oceanic environment and, therefore, acoustic propagation in the ocean.

The two previous chapters gave us a theoretical approach concerning these two models. Now, we are going to highlight the coupling of these two models, the inputs that the coupled model needs, and the outputs we can get from it. The block diagram of Figure 4.1 depicts the over plan, as followed in the next sections.

Initially, we enter the OBL model with a set of boundary conditions, with some initial conditions, and with a set of parameters including the time-step of integration of the OBL model and the time interval between each resulting ray trace. From the predicted output of temperature and salinity profiles, we compute a sound-velocity profile which allows us to trace the paths of acoustic rays according to a set of geometrical parameters such as the source depth, the maximum range, and the initial angle of a ray.²

B. INITIAL CONDITIONS

We have to initialize the coupled model with a temperature profile, that is, temperature T in Celsius versus depth z with a one-meter increment and a salinity profile, that is, salinity S in g/kg versus depth z with a one-meter increment. These profiles can be obtained from climatological data [Ref. 7], as the ones we used to analyze some applications of this coupled model, or from an XBT (expendable bathythermograph) and a salinity profile from climatology. We can also assume a constant salinity profile based on an average salinity in the area studied because of the small effect of salinity variations on sound-velocity computation.

²In all of the previous chapters, we wanted to be consistent with the coordinate systems used in each reference, that is, [Ref. 4] for Chapter II and [Refs. 1,5] for Chapter III. In Chapter II, y is the downward vertical axis and, in Chapter III, z is the upward vertical axis. Since the coupling is done through the output T and S profiles of the OBL model feeding the input profiles of the acoustic model, this notation conflict does not affect the coupling by itself, nor the codes of the coupled programs.

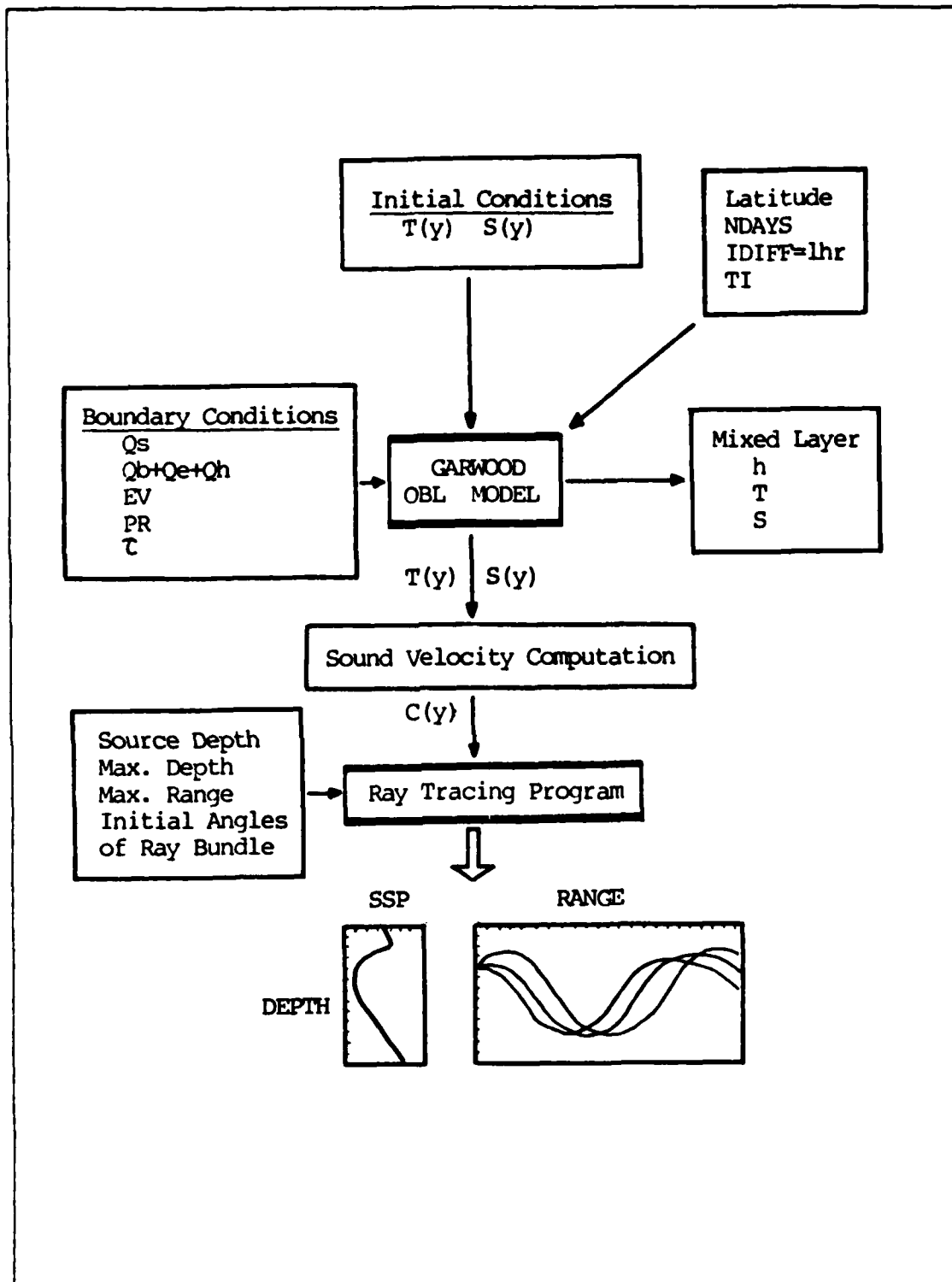


Figure 4.1 Coupling the OBL model with the ray tracing program.

C. BOUNDARY CONDITIONS

The boundary conditions or atmospheric forcing factors we have to provide are listed below.

The hourly solar radiation flux Q_s has to be given in W/m^2 versus time in hours. The climatology gives us generally a daily average Q_{savg} . In our study we will simulate a diurnal cycle for Q_s based on the following formula :

$$\begin{aligned} Q_s &= Q_{smax} \sin(\pi t/12) & \text{if } 0 < t < 12 \text{ hours,} \\ Q_s &= 0 & \text{if } 12 < t < 24 \text{ hours.} \end{aligned} \quad (4.1)$$

as depicted in Figure 4.2.

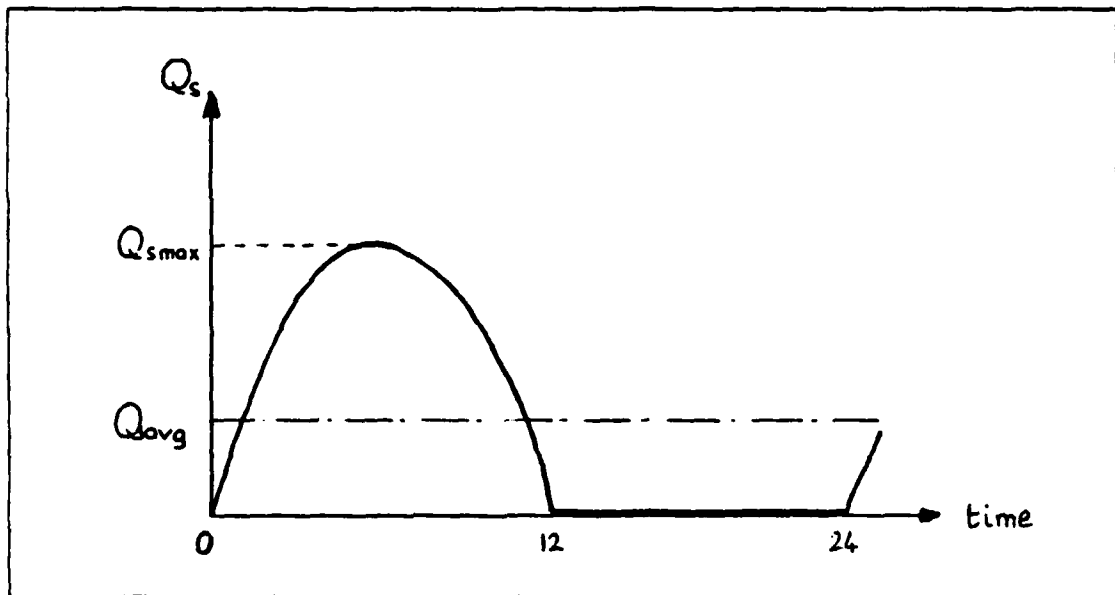


Figure 4.2 Simulated diurnal cycle.

A straight-forward integration leads to the following relation :

$$Q_{smax} = \pi Q_{savg} \quad (4.2)$$

Simulation of clouds is done by allowing only a part of this Q_s as input solar radiation (20 to 50% of Q_s for example) at the sea surface.

The values of the latent flux of heat Q_e , the sensible flux of heat Q_h and the back radiation Q_b have to be provided on an hourly basis. In the simulations of the next chapter, we will pick some average values of the sum $Q_e + Q_h + Q_b$ from the climatology, depending on what time of the year we are working with.

The evaporation rate EV in mm/hour is also evaluated from climatological data, and precipitation rate PR in mm/hour can be simulated. Heavy rain cases will be considered also because of some interesting effects.

TABLE 2
WIND SPEED AND WIND STRESS CORRESPONDENCE

Wind Speed		Wind Stress
knots	m/s	g/cm/sec ²
5	2.5	0.106
10	5	0.423
15	7.5	0.959
20	10	1.694
25	12.5	2.647
30	15	3.811
35	17.5	5.188
40	20	6.776

The wind stress τ in g/cm/sec² has to be provided hourly also. In our simulations, we will consider both constant strong wind as well as light wind conditions. Based on equation (4.3)

$$\tau = \rho_a C_d U_{10}^2 \quad (4.3)$$

where an air density ρ_a of 1.21 kg/m³ and a drag coefficient C_d of 1.4×10^{-3} have been chosen. The correspondence between wind speed and wind stress is given in Table 2.

D. OTHER INPUT PARAMETERS

The other parameters we have to input in the coupled model are the latitude of the area studied, the number of days **NDAYS** during which we want to integrate the model, the interval of integration used by the model (**IDIFF** = 1 hour in this study), and the frequency **TI** in hours with which we want to output some graphic results from the acoustic ray tracing program.

E. OUTPUTS OF THE OBL MODEL

From the OBL model we can get the hourly values of the predicted depth, temperature and salinity of the mixed layer, and we are able to follow the evolution of these different parameters on tabulated outputs.

The link with the acoustic model is done through the hourly computed profiles $T(z)$ and $S(z)$. Depending on the frequency **TI**, these profiles (renamed $T(y)$ and $S(y)$ for notational consistency as mentioned in a previous note) are used to compute the sound-speed profile $c(y)$ by a special subroutine **SVEL**.

F. SOUND-SPEED COMPUTATION

In the subroutine computing the sound-speed, we used the equation derived by Chen and Millero [Ref. 8]. The sound-speed obtained agrees with the data of Del Grosso at one atmosphere [Ref. 9] and with the data of Wilson at high pressures [Ref. 10]. Other formulas for sound-speed are mentioned by Urick [Ref. 11], but the one we used is most often suggested for oceanographic calculations. Further more, comparisons of graphic outputs do not reveal any significant differences between the results obtained by using these various equations.

G. RAY TRACING

The computed sound-speed profile $c(y)$ is used as a main input in the acoustic model. Depending on the case we want to study, a set of geometrical parameters has to be provided such as the source depth **Y0**, the maximum range **RANGE**, and the maximum depth **N**. The bundle of rays to be plotted is defined by the number of rays **M**, the initial angle **B0** of the upper ray of the bundle, and the angle increment **DELB** between two rays. Different equations for defining a bundle of rays can be set inside the subroutine. Thus, it is always possible to pick up a specific bundle of rays to highlight some effects of the atmospheric forcing on some precise type of rays and demonstrate some acoustic energy redistribution.

Since, in this research, we want to give an example of the application of the use of this coupled model, we will choose generally a ray-bundle width of 5 to 8 degrees which should correspond to an active sonar operating at a frequency in the range of 5 kHz.

Finally, the main output of the coupled model is a plot of the sound-speed profile aside an acoustic ray tracing for a given set of parameters defined previously.

H. NOTE ON THE ALGORITHM USED IN THE ACOUSTIC MODEL

Usually, in most acoustic models, the input sound-speed profile is approximated by a piecewise linear curve as depicted in Figure 4.3.

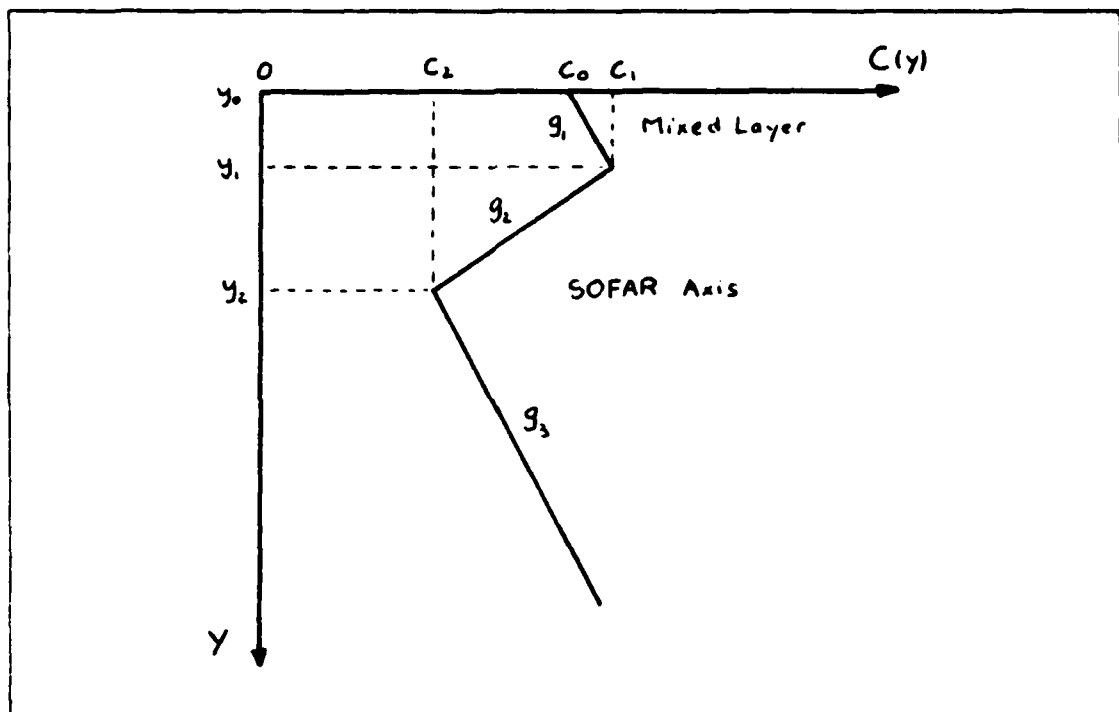


Figure 4.3 Piecewise linear approximation of a typical sound-speed profile.

Thus, the profile can be modeled mathematically by the following equation :

$$c(y) = c_{i-1} + g_i(y - y_{i-1}) \quad , \quad y_{i-1} \leq y \leq y_i \quad (4.4)$$

and is composed of several distinct straight line segments, each with its own constant gradient g_i . In each such delimited slab i , because of the constant gradient g_i , the ray path is an arc of a circle for which an equation is easy to compute and fast to plot. Since a profile is usually divided into a few discrete slabs (for example, 10), a more computationally efficient subroutine could be derived from the one discussed in Chapter II. This subroutine would invoke gradient sign checking and initial angle comparison to the horizontal only when a ray crosses a boundary between two slabs.

In our study, this checking and comparison are done at each depth increment (1 m) as well as the plotting of a new point belonging to the ray path. It is certainly a much slower algorithm than the previous one, but we had to consider that, even if the output profiles $T(y)$ and $S(y)$ of the Garwood OBL model can be approximated as piecewise linear, the output sound-speed profile $c(y)$ cannot be considered as piecewise linear. This is because $c(y)$ is a highly non-linear function of T , S , and y . This characteristic can be demonstrated by using a simple equation like the one derived by Coppens [Ref. 12]

$$c(T,S,y) = 1449.05 + 4.57T - 0.0521T^2 + 0.00023T^3 + (1.333 - 0.0126T)(S - 35) + 0.0163y . \quad (4.5)$$

This may be rewritten as

$$c = a + bT + cT^2 + dT^3 + eS + fTS + gy . \quad (4.6)$$

Differentiation of c versus depth y yields

$$dc/dy = g + (b + 2cT + 3dT^2 + fS) dT/dy + (e + fT) dS/dy . \quad (4.7)$$

Hence, in a particular slab i , even if $(dT/dy)_i$ and $(dS/dy)_i$ are constant, it can be seen from (4.7) that $(dc/dy)_i$ is not a constant because T and S are not constant in the slab, but are linear functions of depth y .

Finally, the acoustic model developed in Chapter II permits the use of XBT profiles discretized with a depth increment of one meter or more. Use of climatology is often unrealistic due to multiple averaging and too coarse vertical resolution.

V. APPLICATION OF THE COUPLED MODEL TO A SPECIFIC AREA

A. GENERALITIES

In order to investigate the typical results we can obtain from this coupled-model, we shall simulate some cases in the Western Mediterranean Sea. The chart presented in Figure 5.1 shows the site to be studied: $\varphi = 42.5^\circ\text{N}$, $\lambda = 007.5^\circ\text{E}$.

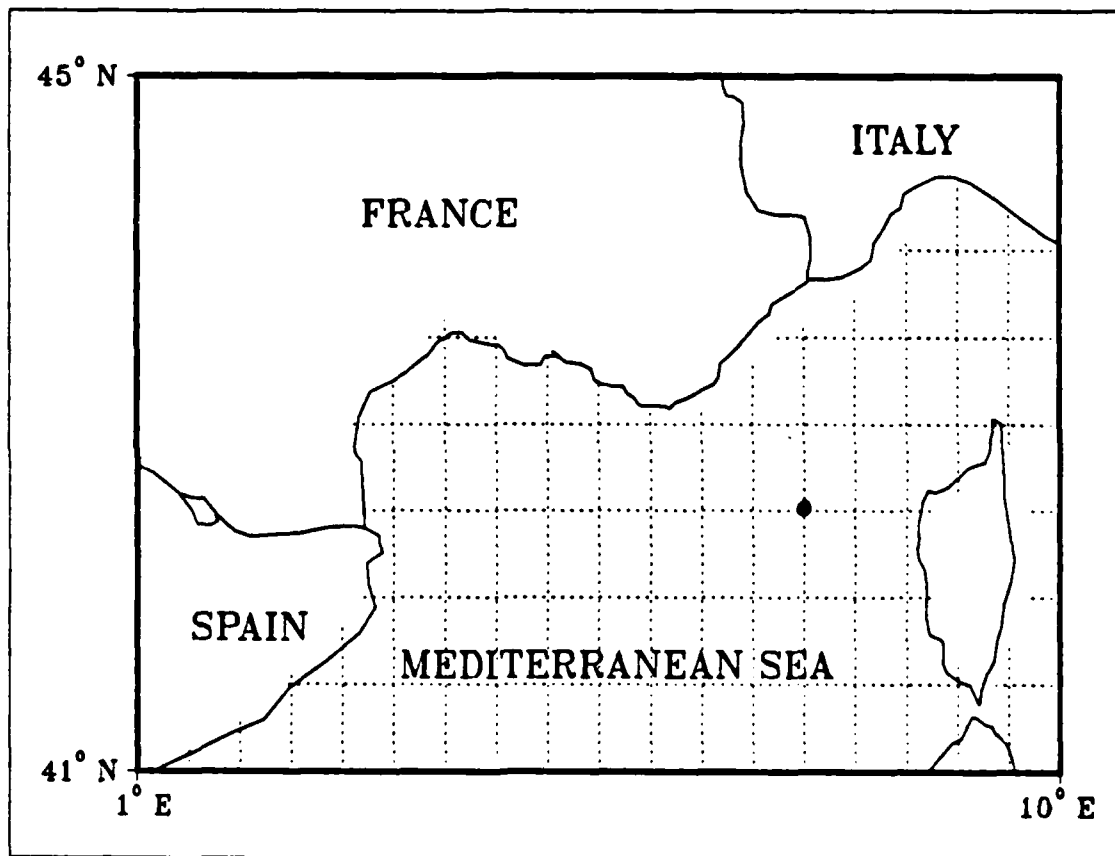


Figure 5.1 The northern region of the Algero-Provencal Basin.

The Mediterranean Sea is one of the major, deep closed seas of the world. The water mass interacts with the open ocean only through the Strait of Gibraltar, which has a sill depth (300 m) much shallower than the average depth of the rest of these closed waters. The water below this sill remains almost homogeneous in temperature and salinity. The western Mediterranean is an area having very specific oceanographic

and atmospheric features. Figure 5.1 depicts the north part of the Algero-Provencal Basin, which is one of the two large deep basins of the Western Mediterranean. The basin bottom contains wide, flat abyssal plains, averaging 2700 meters in depth. The water mass is clearly bounded by land and islands, and this sea is well ventilated due to the quantity of deep water formed at the surface by winter cooling. As described in [Ref. 13], during winter, the Alpine relief brings intrusions of polar continental air masses into contact with the surface waters of the northern part of the Mediterranean. Strong, cold, dry, continental winds (mistral) can blow for a few days, cooling the surface water and leading to a vigorous convective mixing. Such a strong sinking motion of surface water can mix and cool uniformly as much as the upper thousand meters of the water column. The sea-state is often characterized by a short wavelength swell which causes a very rough sea during storms. Another interesting result of the interaction between the atmosphere and the sea is that the Mediterranean water is characterized by high temperatures (13°C at 1000m) and high salinities (38.4-38.45 g/kg) which are surpassed only in the Red Sea. This is due to the large heat input and an excess of evaporation over fresh water input (precipitation and river contribution).

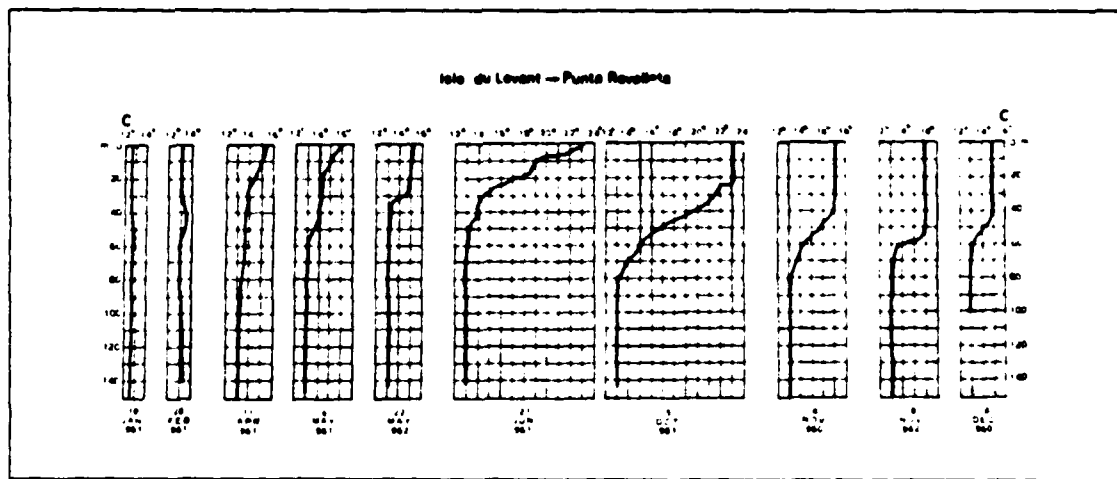


Figure 5.2 Seasonal variation of the temperature profile in the northern part of the Western Mediterranean.

Figure 5.2 from [Ref. 14] gives an example of the seasonal variations observed in the Ligurian Sea, that is, the northern part of the Algero-Provencal Basin. It can be observed that, in this region, the water column is completely isothermal in winter. A warmer surface layer evolves progressively during springtime. In autumn, it decreases

in temperature but increases in depth until winter conditions are reached again. The summer temperature profile is characterized by a top layer about 20 to 40 meters thick overlying a thermocline with large temperature gradients (up to 1 to 2°C.m).

The Mediterranean Sea is also of interest for the numerous naval operations conducted in that area. For this reason, it is of interest to study some of the features of the acoustic propagation that are related to atmospheric factors. For example, in this region, the heating by the sun of the upper layers of water, together with an absence of mixing by the wind, causes a strong near-surface negative sound-speed gradient to develop during the spring and summer months. This thermocline overlies isothermal water at greater depths. The result is a strong shallow internal sound channel (SOFAR channel: sound fixing and ranging) with its axial depth near 150 meters. During the autumn, the profile returns to its winter time conditions, with isothermal water and positive sound-speed gradient extending to the surface of the water column, leading to a half-duct type of propagation. During the summer season the near-surface negative gradient and the resulting strong downward refraction greatly limit the detection range of surface ship hull-mounted sonars. By way of compensation, the summer time channel in the Mediterranean produces convergence zones for a near-surface source similar to the deep-ocean sound channel, although the range of the zone is much less because of the smaller vertical extent of the channel compared to the open ocean. Therefore, from the point of view of sound propagation, the important factor here is the existence of a predominantly isothermal and isohaline water mass at depth, which results in a sound-speed profile characterized by a deep constant-gradient section. Only the upper section of the profile will contain irregularities as depicted in Figures 5.3 and 5.4. See [Refs. 11,14] for more details.

B. SUMMARY OF THE DIFFERENT PARAMETERS USED IN THIS STUDY

In the simulations discussed in the next sections, we used the parameters listed in Table 3. Four different cases are to be analyzed, corresponding to the months of December, February, June, and September. The boundary conditions are assumed to be climatological and were obtained from [Refs. 16,17,18,19]. A precipitation rate of 2 mm hour over 12 hours will be assumed for heavy rain cases. Values of 20 to 50% of Q_s will be used to simulate the reduction of radiation incident on the sea surface due to the presence of clouds. The initial profiles of temperature and salinity come from the climatology used by the Fleet Numerical Oceanographic Center (FNOC). Finally, we will avoid the complication of bottom reflection by assuming an infinitely deep ocean.

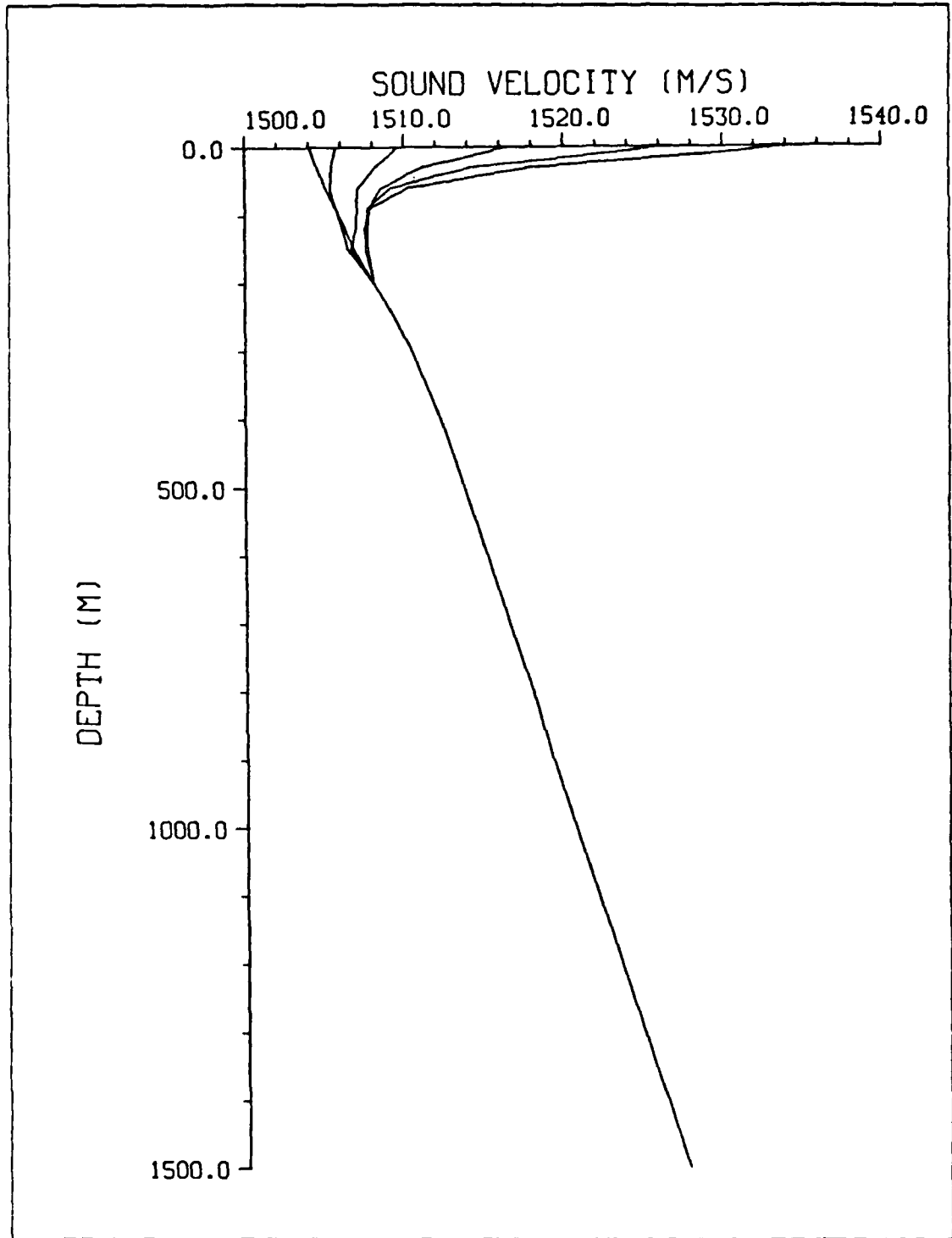


Figure 5.3 SSP for the Ligurian Sea, Western Mediterranean
February to July from left to right.

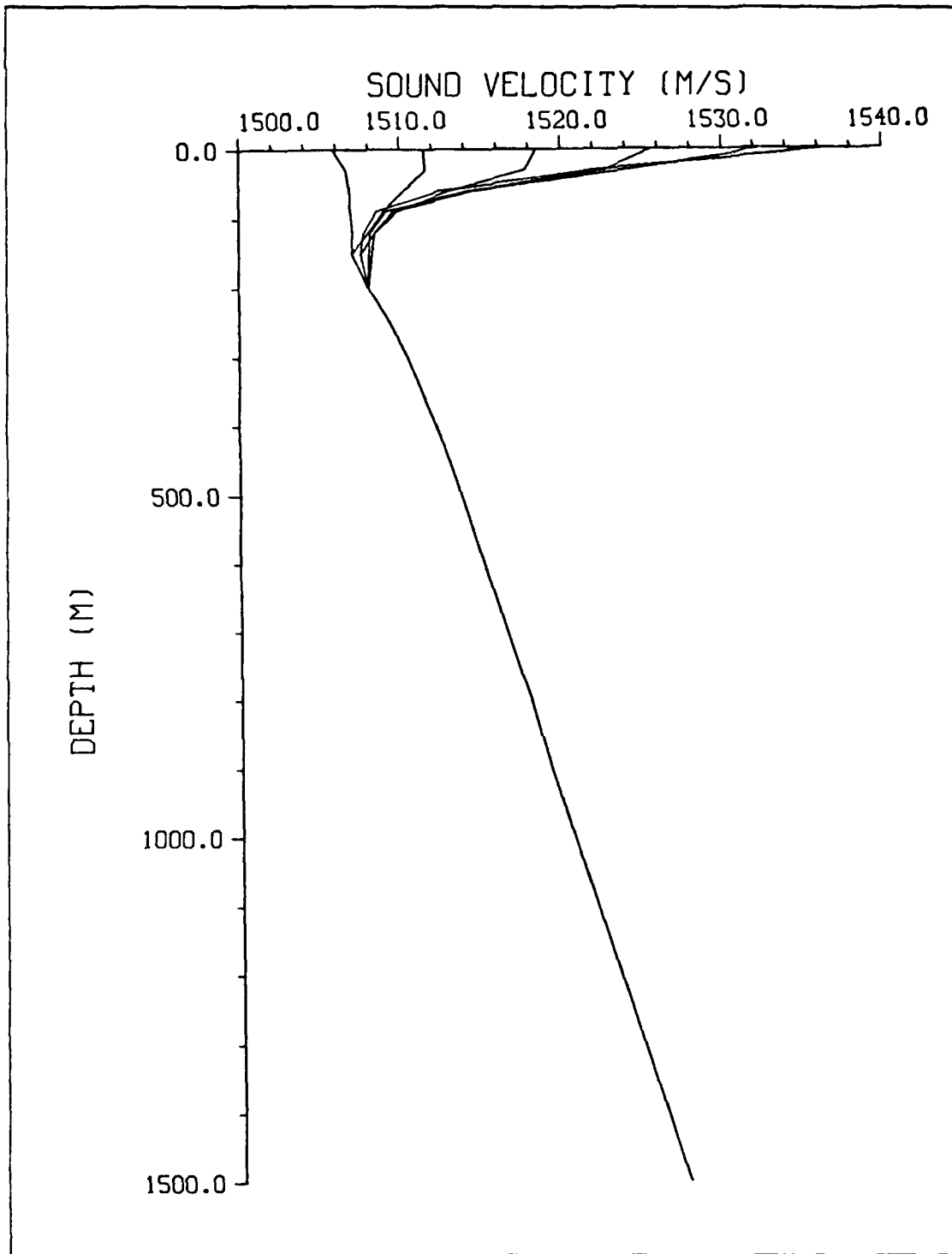


Figure 5.4 SSP for the Ligurian Sea, Western Mediterranean
August to January from right to left.

C. DECEMBER CASE

1. Source at 10 meters

This case simulates a surface-ship hull-mounted sonar and we will consider strong wind (30 knots) as well as light wind (5 knots) conditions.

TABLE 3
HEAT FLUXES CLIMATOLOGY FOR THE MEDITERRANEAN
(W/M^2)

	December	February	June	September
Q_s	130	190	250	190
Q_{smax}	400	600	780	600
$Q_h + Q_e$	190	120	80	120
$Q_b + Q_h + Q_e$	280	190	130	190
Q_{net}	-150	0	120	0
EV(mm/hr)	0.3	0.2	0.1	0.2

a. Strong wind conditions (30 knots)

The evolution of the mixed layer depth h for different cases is shown in Table 4. In the case of no clouds and no rain, we find that the mixed layer depth increases significantly due to the combined effects of the strong winter time surface cooling ($Q_{net} = -150W/m^2$) plus the effect of the wind stirring.

Figure 5.5 shows the effect of this mixing and cooling on the acoustic ray paths. The first graph shows the acoustic propagation at time = 0 hour for a beamwidth $\theta = 6^\circ$, and the second graph shows the propagation after 24 hours of strong wind. By counting the rays, we find that 39% of the acoustic energy has been redistributed. More rays are filling a deeper mixed layer, and the convergence zone (CZ)³ has weakened. There is no effect on the CZ range which remains between 15 and 20 km.

Figure 5.6 shows, with more detail, the transformation of a bundle of refracted-surface reflected (R-SR) rays (initial angles between 87° and 89.3°) after 24 hours of strong wind. For a total of 24 R-SR rays, 13 rays are now trapped in the

³The term convergence zone (CZ) is applied to a phenomenon of focalization of the underwater sound in annular domains.

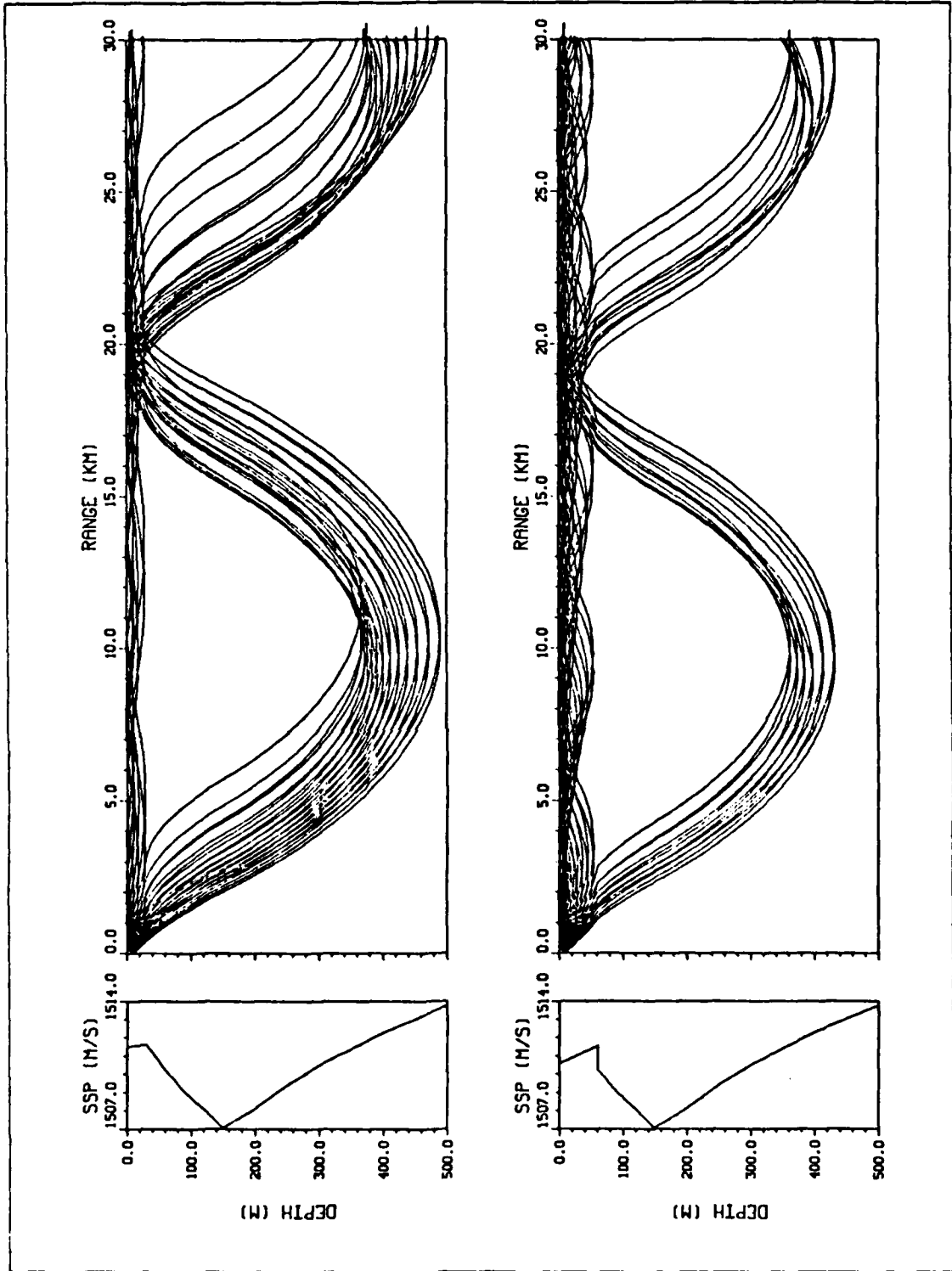


Figure 5.5 December, strong wind, source at 10 meters: $t = 0,24$ hrs, $\theta = 6^\circ$.

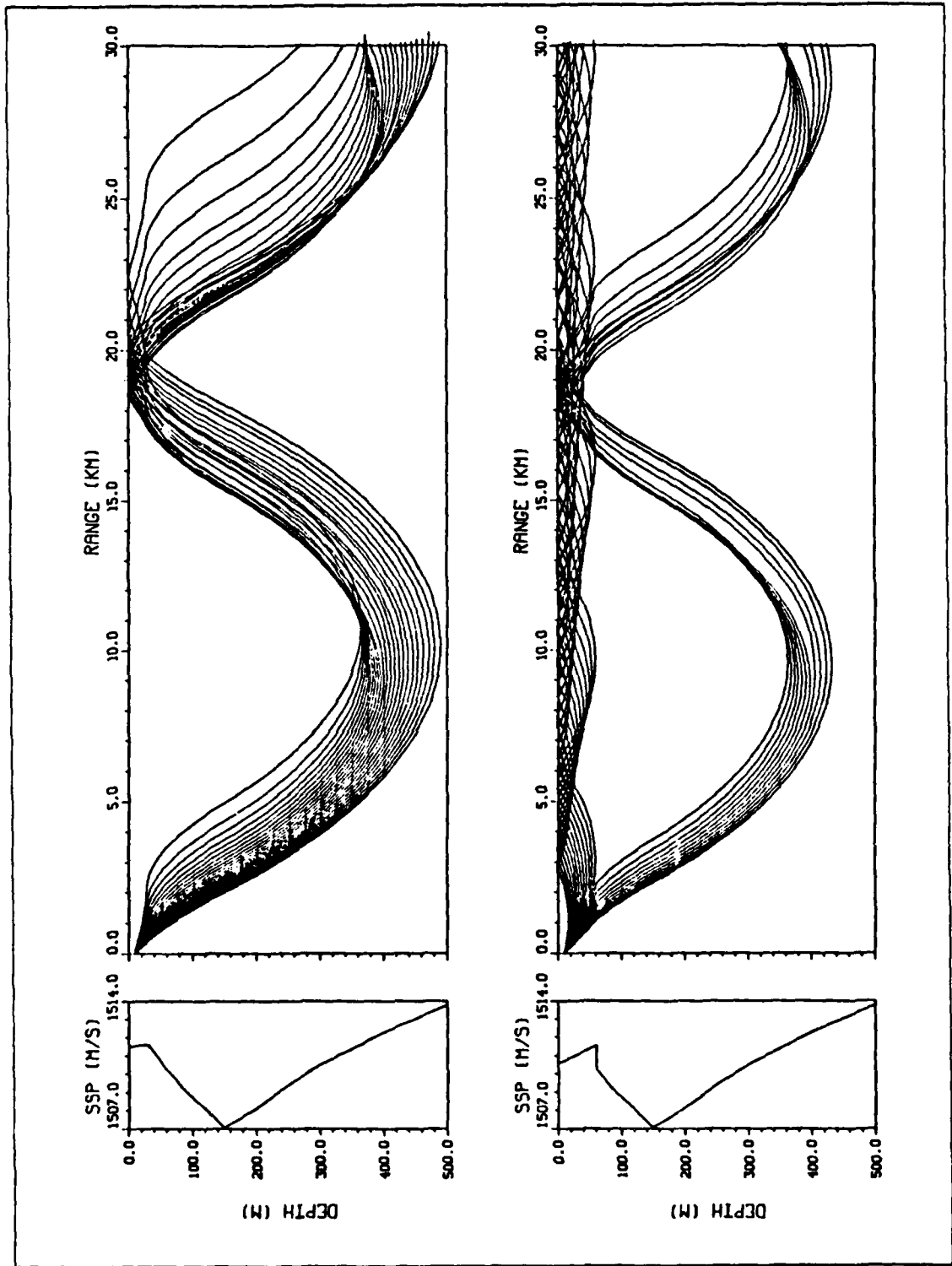


Figure 5.6 December, transformation of R-SR rays, strong wind: $t = 0,24$ hrs.

mixed layer, increasing the possibility of detection on a shallow target for a surface-ship sonar. On the second graph of Figure 5.6, the weakening of the CZ is quite apparent.

TABLE 4
EVOLUTION OF THE MIXED LAYER DEPTH
IN DECEMBER WITH A STRONG WIND

$t(\text{hr})$	no rain	no rain	no rain	heavy rain for 12 hrs
	no clouds	50% Q_s	20% Q_s	20% Q_s
	$h(\text{m})$	$h(\text{m})$	$h(\text{m})$	$h(\text{m})$
0	37.0	37.0	37.0	37.0
12	51.7	52.5	53.1	50.6
24	60.3	61.2	61.7	59.4
36	65.7	67.0	67.7	65.7
48	70.8	72.0	72.8	70.9
60	74.3	76.0	76.9	75.1
72	78.2	79.5	80.4	78.7

From Table 4, we can see that adding clouds to the simulation increases the surface cooling and thus accelerates a somewhat the deepening of the mixed layer due to the added production of turbulence by wind stirring. The effect of superimposing heavy rain for 12 hours is a slight damping of the mixed layer deepening rate. The main conclusion of these last test cases is that, with strong winds, the overall effect of clouds and rain is not too significant and the general shape of the acoustic ray trace does not change.

b. Light wind conditions (5 knots)

Light wind conditions allow us to analyze the interesting effect of heavy rain on the acoustic propagation. The evolution of the mixed layer depth is shown in Table 5 .

Figures 5.7 and 5.8 show the effect of a heavy rain on a winter time sound-speed profile.

The gradient of the sound-speed versus depth can be expressed as :

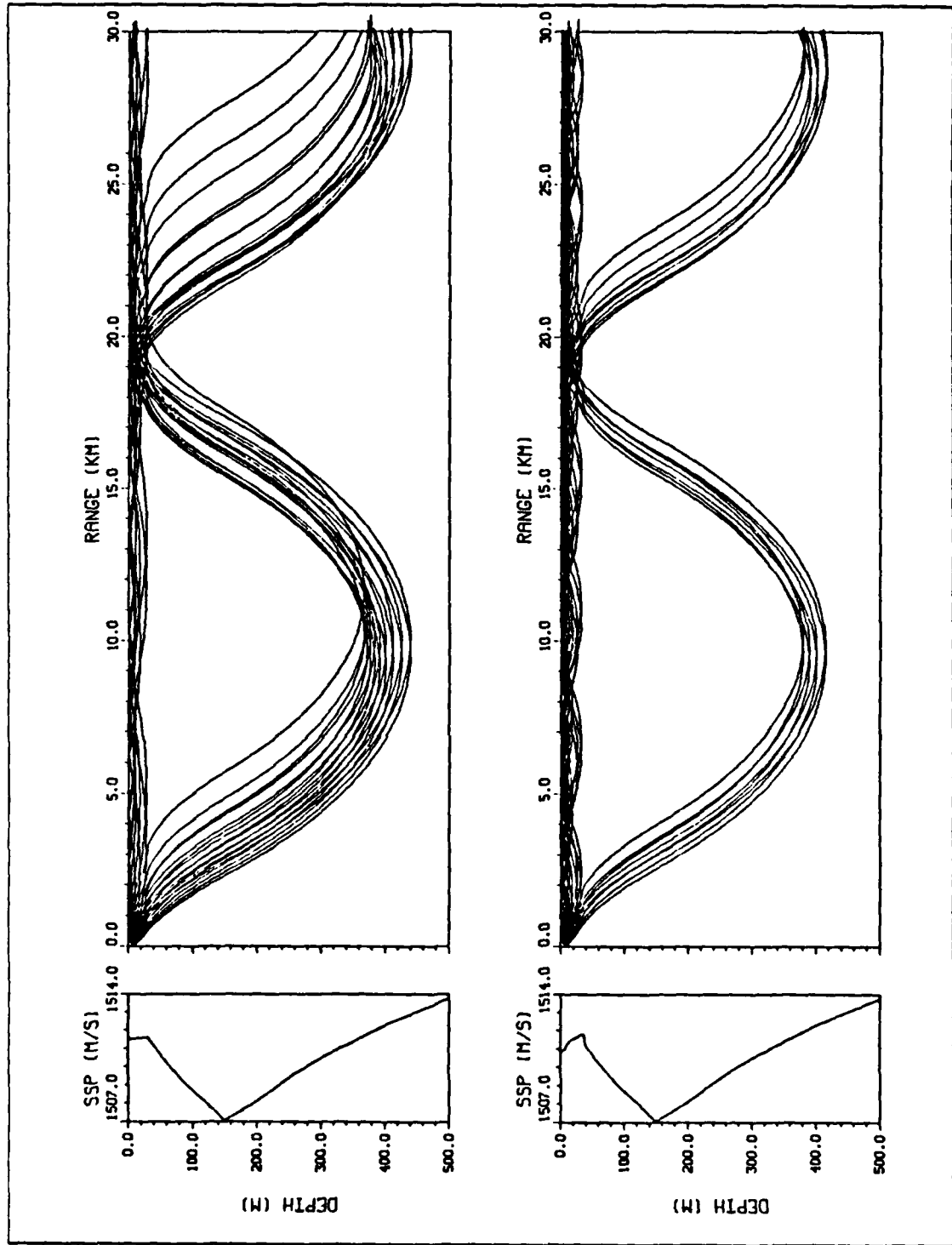


Figure 5.7 December, light wind, heavy rain for 12hrs,
 source at 10 meters: $t = 0,6$ hrs, $\theta = 5^\circ$.

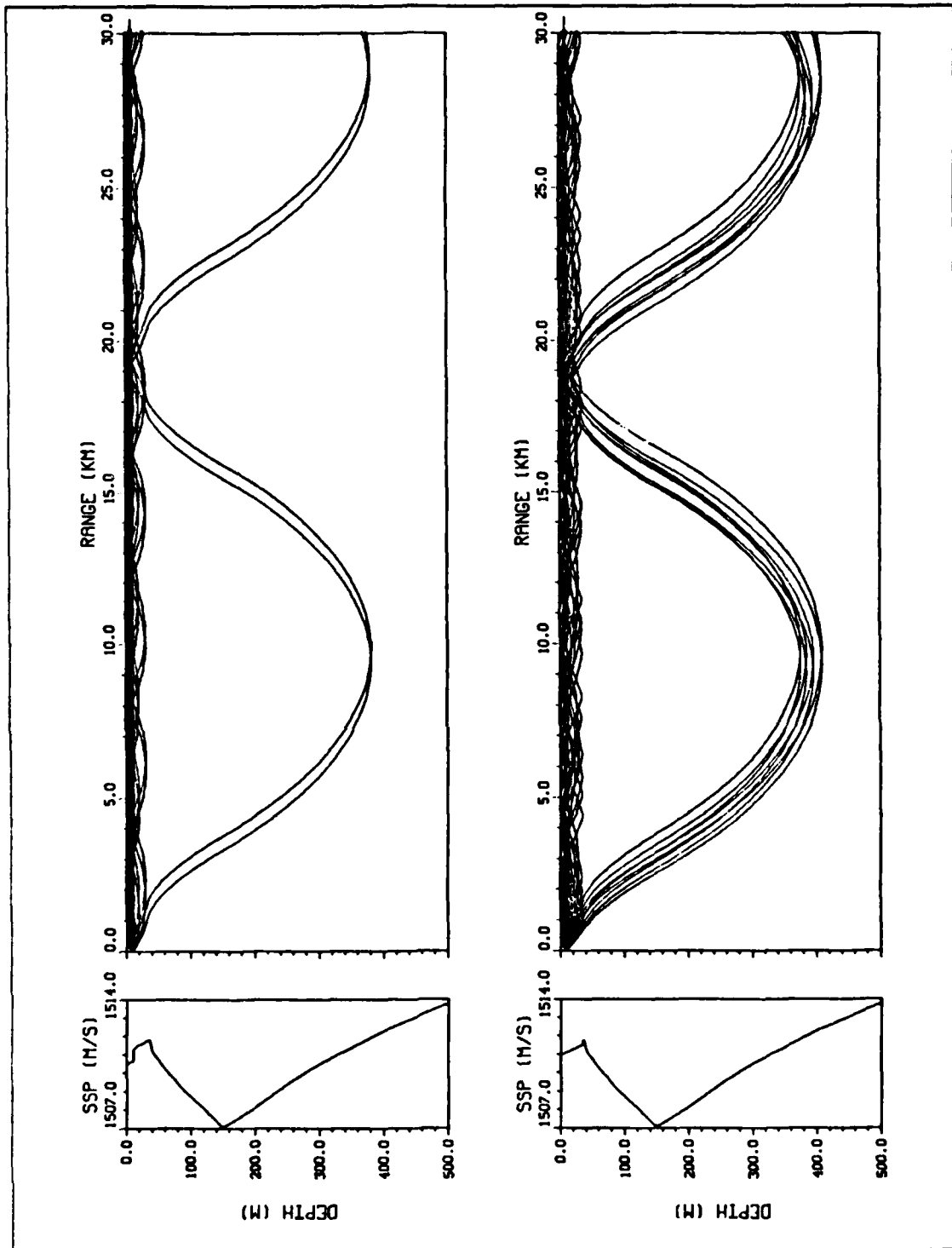


Figure 5.8 December, light wind, heavy rain for 12hrs,
 source at 10 meters: $t = 12, 14$ hrs, $\theta = 5^\circ$.

$$dc/dy = \partial c/\partial T dT/dy + \partial c/\partial S dS/dy + \partial c/\partial p dp/dy \quad (5.1)$$

where the average values of the partial derivatives are the following :

$$\partial c/\partial T = 4.0 \text{ m/sec/}^\circ\text{C} , \quad (5.2)$$

$$\partial c/\partial S = 1.2 \text{ m/sec/g/kg} , \quad (5.3)$$

and

$$\partial c/\partial p = 0.016 \text{ m/sec/m} . \quad (5.4)$$

TABLE 5
EVOLUTION OF THE MIXED LAYER DEPTH IN DECEMBER
WITH LIGHT WINDS AND HEAVY RAIN FOR 12 HRS

t(hr)	h(m)	t(hr)	h(m)
0	37.0	24	39.9
6	7.9	36	43.0
12	10.4	48	46.4
13	14.4	60	49.3
14	34.5	72	52.5

The temperature term of the gradient dc/dy is dominant, and the salinity term is usually so small that it is very often neglected. In the case of heavy rain, however, the term $\partial c/\partial S dS/dy$ is not negligible and can be very important and even dominant. In the mixed layer, $dT/dy=0$. Thus if heavy rain occurs, we get $dS/dy >> 0$, and dc/dy can be positive and much greater than usual. This yields a sharp "inversion" as depicted by the sound-speed profile of Figures 5.7 and 5.8.

Another way to examine the effect of the rain is to consider the surface buoyancy flux B_0 :

$$B_0 = \alpha g Q_{\text{net}} \cdot \rho C_p - \beta g S (EV - PR) . \quad (5.5)$$

In winter time, the first term of B_0 is on average strongly negative. This corresponds to an upward buoyancy flux. During heavy rain fall, $EV-PR$ is negative, leading to a positive second term in B_0 . This fact can be verified by investigating the last two columns of Table 4. Rain fall damps the upward buoyancy flux and, thus, decreases the mixed layer deepening.

In Figures 5.7 and 5.8, we see the effect of heavy rain fall on the acoustic propagation at time 0, 6, 12, and 14 hours. In these graphs, the beamwidth has been set to 5° . After 6 hours of heavy rain, a high density of R-SR rays have been trapped in the mixed layer. After 12 hours, the effect is even much more important. Almost all the rays are trapped in a shallow mixed layer, and the convergence zone has disappeared. At that time, the only chance for a surface-ship sonar to get any detection is for a shallow target.

However, this effect does not last very long after the rain stops. We can see in Table 5 that, in only two hours, the mixed layer depth almost returns to its initial value. We can also notice in Figures 5.7 and 5.8 that, only two hours after the end of the rain, the acoustic propagation is almost the same as for the initial case at $t=0$. This is due to the strong winter time and night time surface cooling, even though the wind is light. This fact also demonstrates the strong effect of surface cooling on the mixed layer deepening in winter time.

2. Source at 40 meters

Now, we are going to study the case where the source is just below the initial mixed layer (37m).

a. *Strong wind conditions (30 knots)*

In the case of no clouds and no rain, Figure 5.9 shows the evolution of the acoustic propagation over one day of strong wind for a beamwidth θ of 6° .

Initially, at time $t=0$, all the rays are R-SR, and we have a perfect case of convergence zone (CZ) detection with a strong focusing effect at the smaller range of the CZ (around 15km). After 24 hours of strong wind, the deepening effect of the mixed layer redistributes 42% of the acoustic energy into a mixed layer type

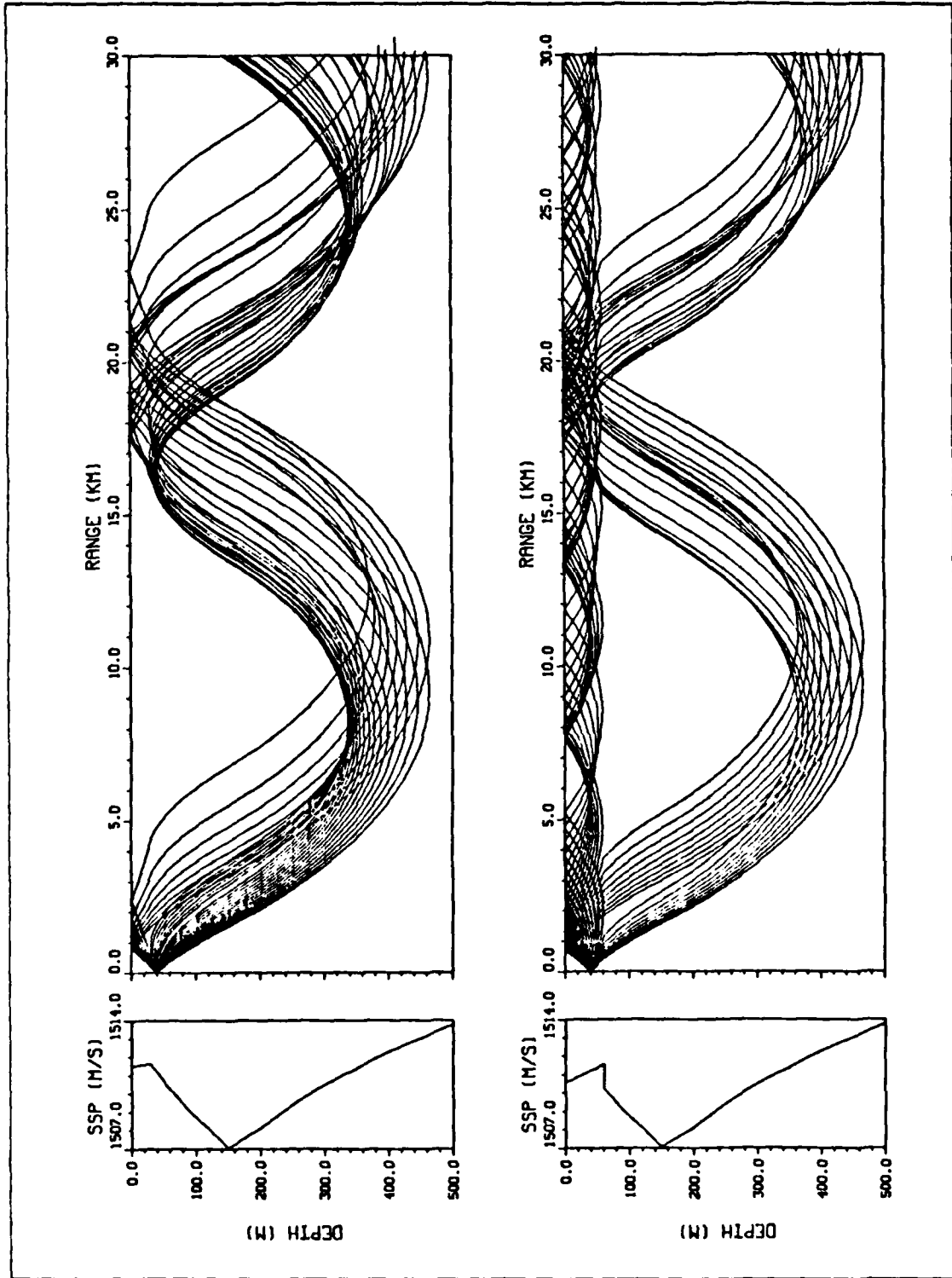


Figure 5.9 December, strong wind, source at 40 meters: $t = 0,24$ hrs, $\theta = 6^\circ$.

propagation. The CZ range stays the same, but the CZ is weakened and the focusing effect is greatly reduced.

Figure 5.9 shows that the detection ability of a towed sonar at 40 m is much improved because of the deepening of the mixed layer mainly due to the wind stirring. For the purpose of highlighting this effect, Figure 5.10 extracts only the influenced ray bundle, that is, the bundle with a beamwidth of 2.5° . All the rays of this bundle are transformed from RR (refracted-refracted) type to mixed layer trapped.

If we would have added clouds to the simulation, with or without rain, we would have found the same general shape for the acoustic ray trace. The fact confirms that, in winter time, the wind mixing has a dominating effect on the acoustic propagation.

b. Light wind conditions (5 knots)

For a source at 40 meters, even with light wind conditions, acoustic propagation is not very sensitive to heavy rainfall. Figure 5.11 shows the ray trace at time 0 and after 12 hours of rain. The difference in shape between the two graphs is not very great. Thus, the effect of heavy rain is to be considered significant, even with light wind conditions (which is not usually the case in winter time during storms passing by), for only a shallow transmitter, as seen in the previous section.

3. Source at 100 meters

If the source is sufficiently deep relative to the mixed layer depth, the atmospheric forcing has no effect on the acoustic propagation. Adding clouds and rain will not change the general shape of the acoustic ray paths. Figure 5.12 depicts the case of strong wind conditions with no clouds and no rain at $t=0$ and 24 hours. For a beamwidth of 6° , the RR rays stay trapped in the shallow SOFAR channel and do not enter the mixed layer. This is because of the strong thermocline (strong negative gradient dc/dy) underlying the mixed layer. For rays to enter the mixed layer, we would need steep initial angles at the source, which is not realistic for the usual sonar beamwidth.

In Figure 5.13, with a source at 80 meters, an interesting effect on the ray paths is depicted. The rays almost appear to be reflected on the the sharp discontinuity created at the top of the thermocline because of the strong wind mixing.

4. Source on the SOFAR axis (150 meters)

Figure 5.14 shows the acoustic ray paths obtained when the depth of the source is set to 150 meters, that is, the optimum depth for the internal sound-channel

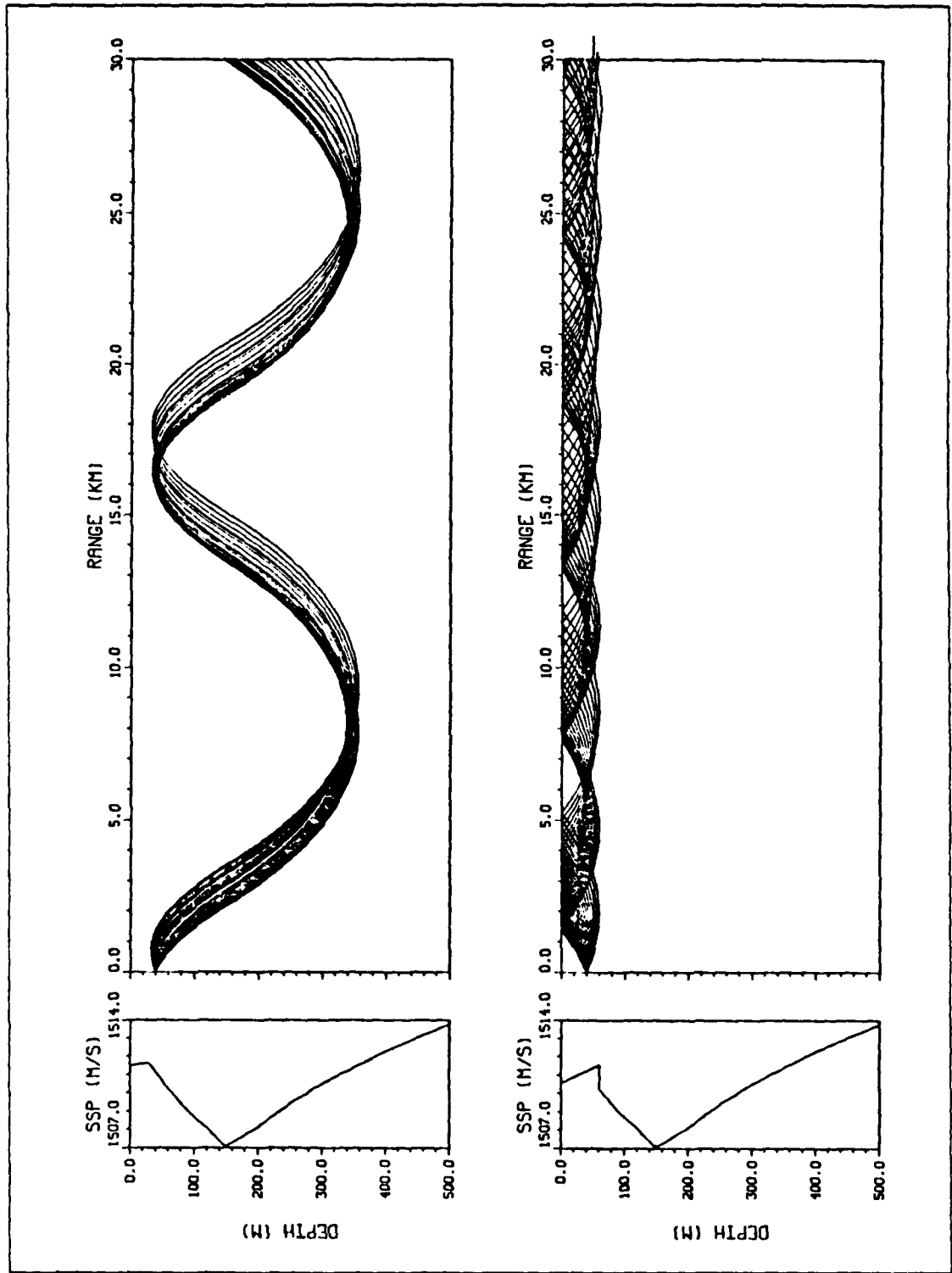


Figure 5.10 December, strong wind, source at 40 meters: $t = 0,24$ hrs, $\theta = 2.5^\circ$.

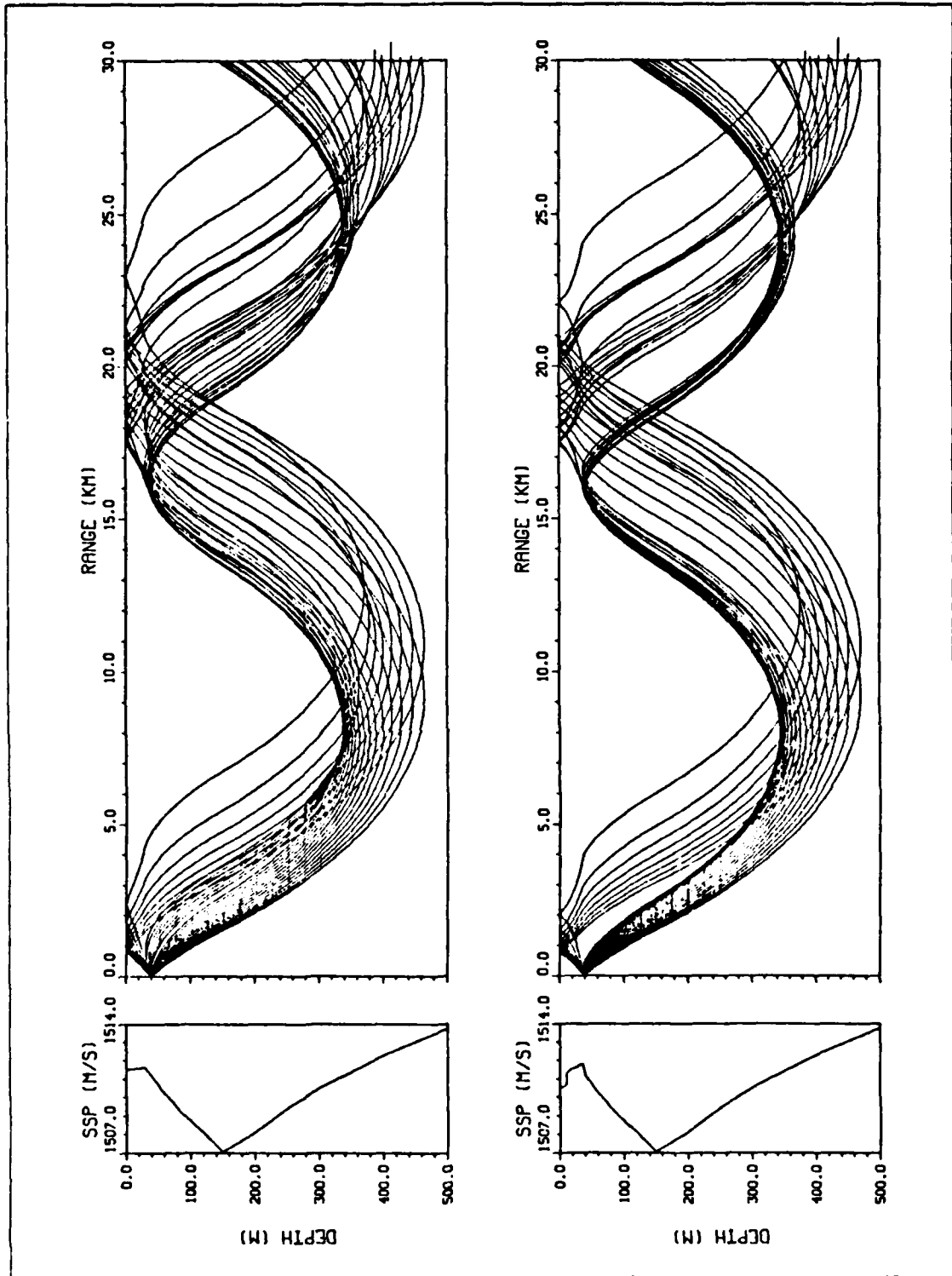


Figure 5.11 December, light wind, heavy rain, source at 40 meters: $t = 0, 12$ hrs, $\theta = 6^\circ$.

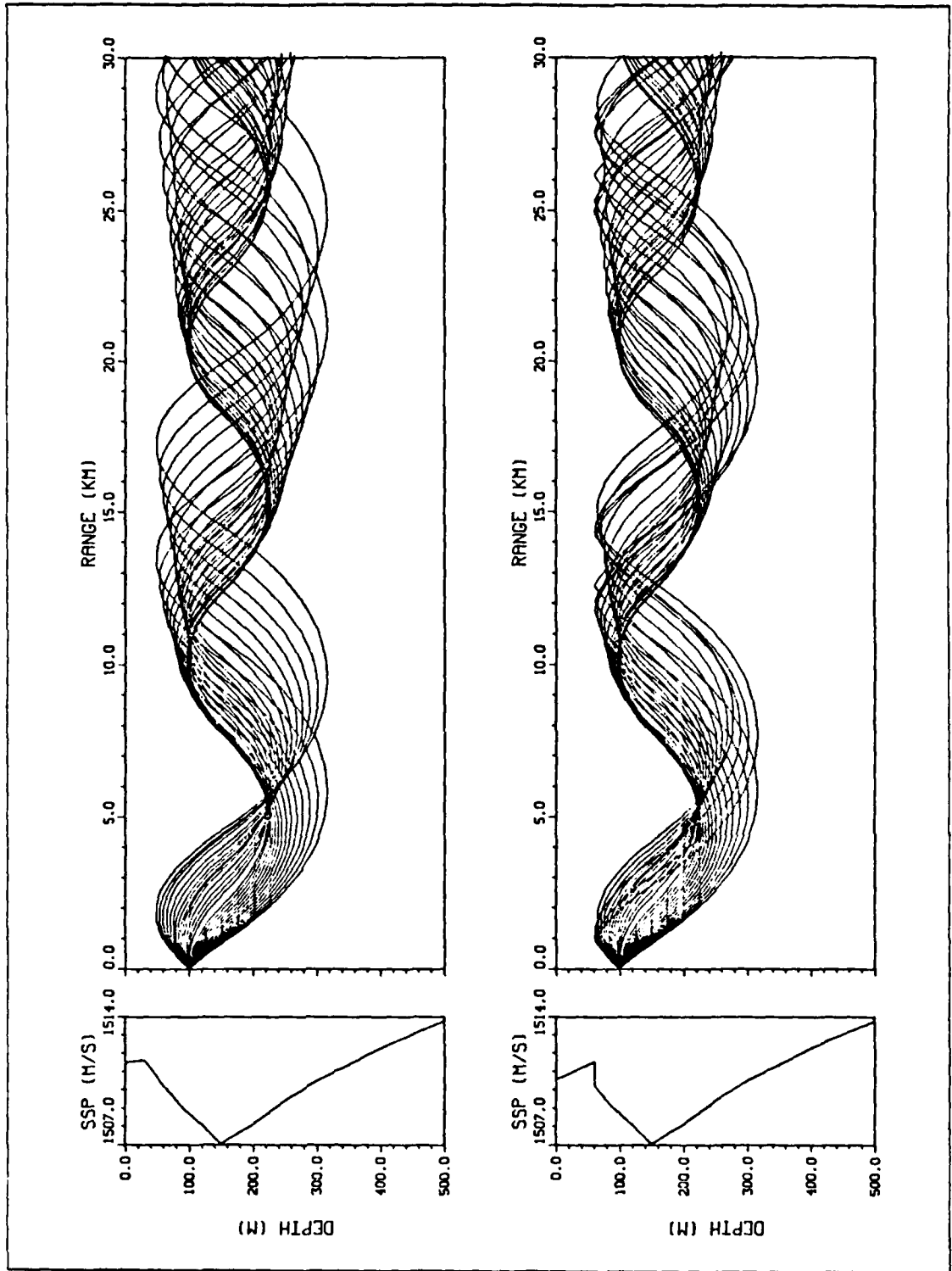


Figure 5.12 December, strong wind, source at 100 meters: $t = 0,24$ hrs, $\theta = 6^\circ$.

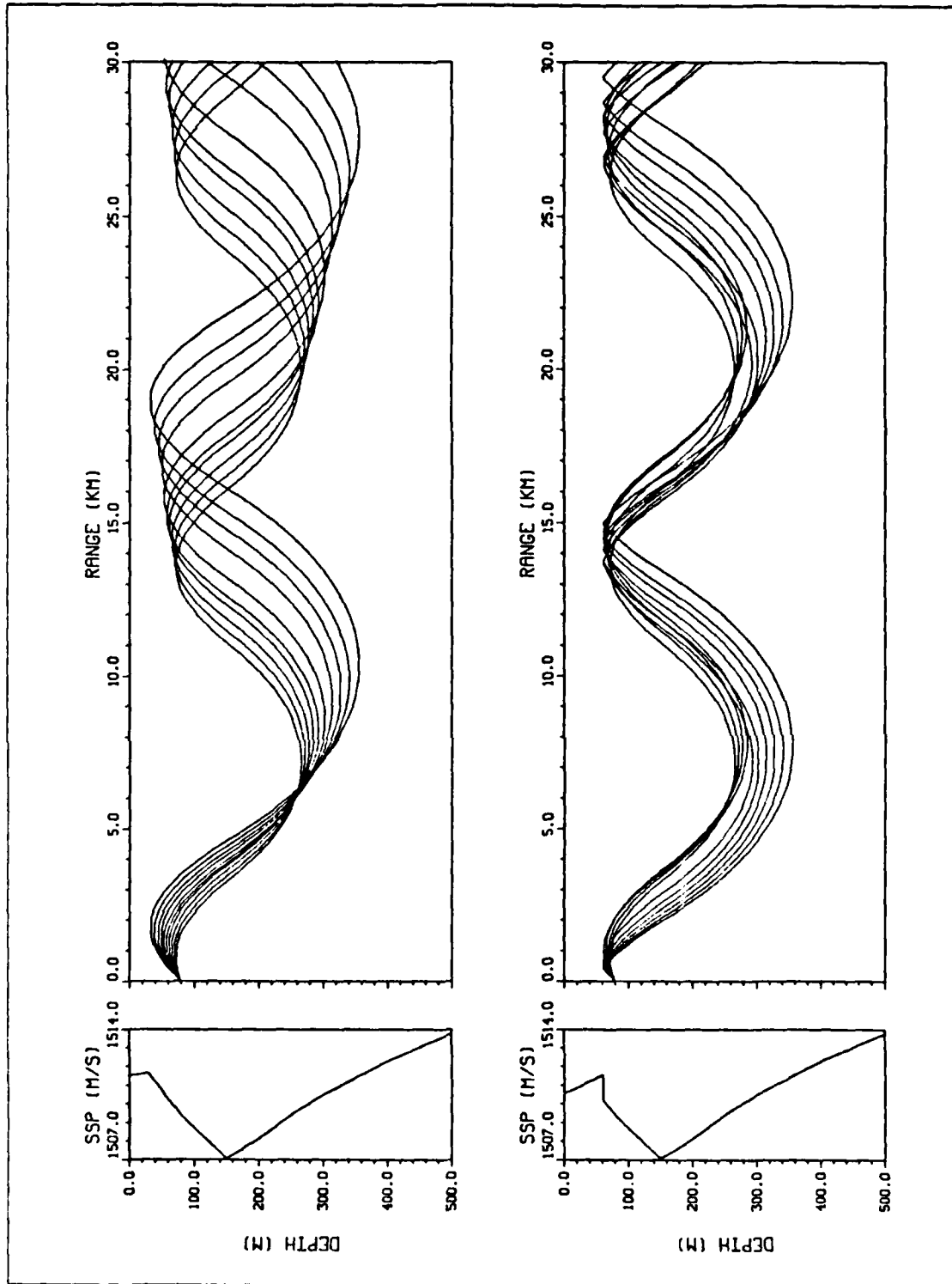


Figure 5.13 December, strong wind, source at 80 meters: $t = 0,24$ hrs, $\beta_0 = 91^\circ$ to 93° .

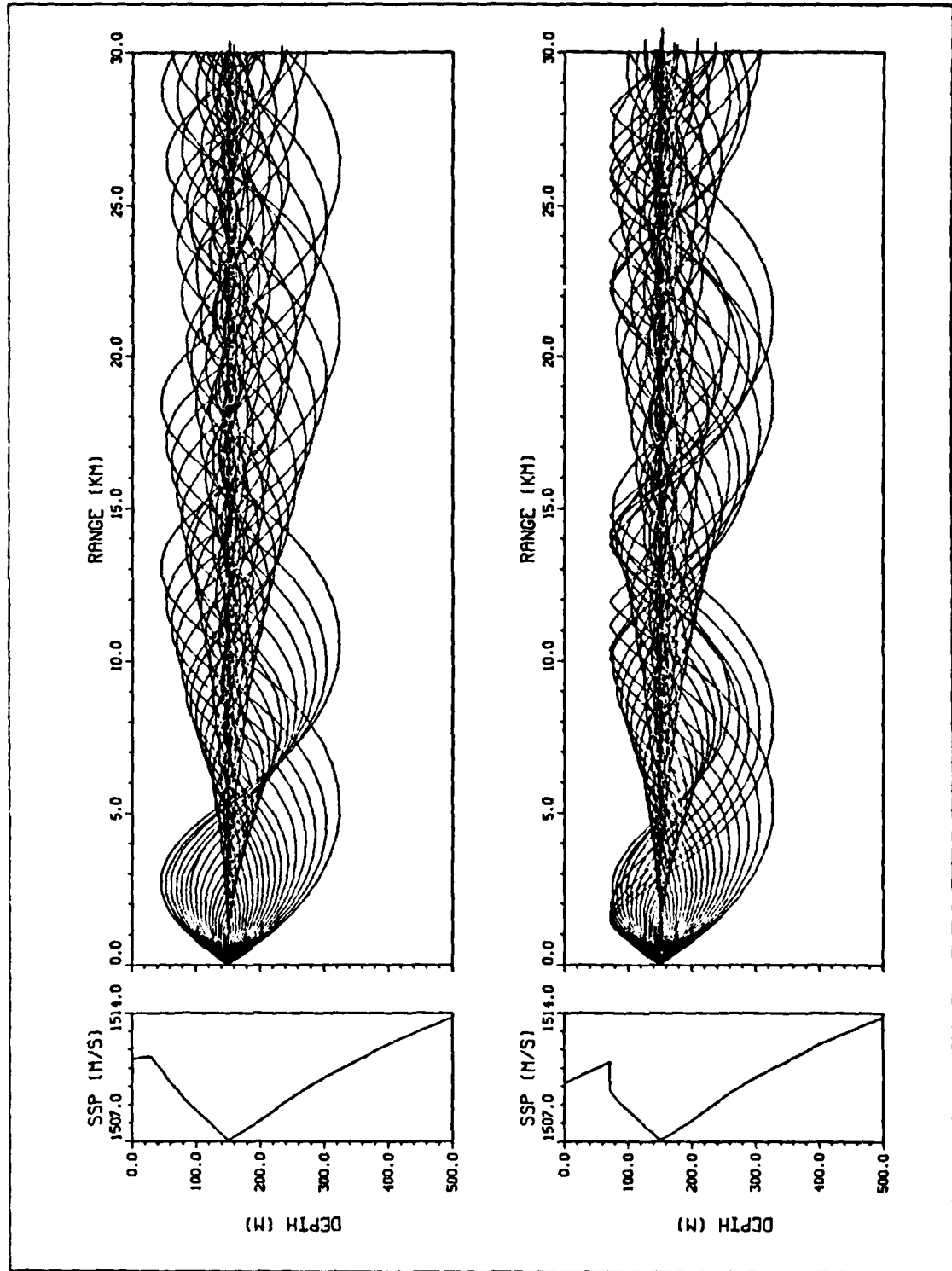


Figure 5.14 December, strong wind, source at 150 m: $t = 0.48$ hrs, $\theta = 9^\circ$.

propagation. Strong wind conditions were simulated for 48 hours and the beamwidth was set to 9° . The interesting acoustic propagation is due to the sharp positive and negative gradients dc dy under and overlying the depth of the SOFAR axis. As mentioned previously, the source is deep enough for the acoustic propagation not to be influenced by the atmospheric forcing. A weak CZ appears at ranges between 15 to 18 km, and these ranges are influenced almost not at all by the boundary conditions.

In that case, if we superimpose the second graphs of Figures 5.5 and 5.14, we can see the combination of the ray traces obtained with a source at 10 meters and a source at 150 meters. The water mass is almost completely filled with acoustic energy, leading to a high probability of detection of a target whose depth would be between 0 and 300 meters.

5. Source at 500 meters

Figure 5.15 displays the case where the wind has been blowing for 24 hours with no clouds and no rain. We would have obtained the same general shape by varying the wind and (or) adding clouds and rain. As in the two previous cases, the source is deep enough for the acoustic propagation not to be influenced by the atmospheric factors. In any case, these graphs were provided to show the excellent shape of the acoustic ray trace in the case of a perfect surface reflection.

6. Conclusions for December

On short time scale, the atmospheric conditions have an effect on the acoustic propagation only for a shallow source (10 to 40 meters in our simulations), that is, for a source in the initial mixed layer or just below.

For such a shallow source, the wind has a dominating effect over rain and clouds. Mainly, this effect is the transformation of R-SR rays to mixed layer trapped rays and the weakening of the convergence zone.

The effect of the surface cooling is also important in winter time. The net upward heat flux was set to -150 W.m^2 in our simulations. This leads to an average deepening of the mixed layer until the month of February when the entire water column is mixed. This was depicted in the light wind conditions cases, and it yields a half-duct type of acoustic propagation.

The effect of heavy rain has been also depicted for light wind conditions and leads to a strong shallow inversion, trapping most of the rays emanating from a shallow source in a shallow surface duct.

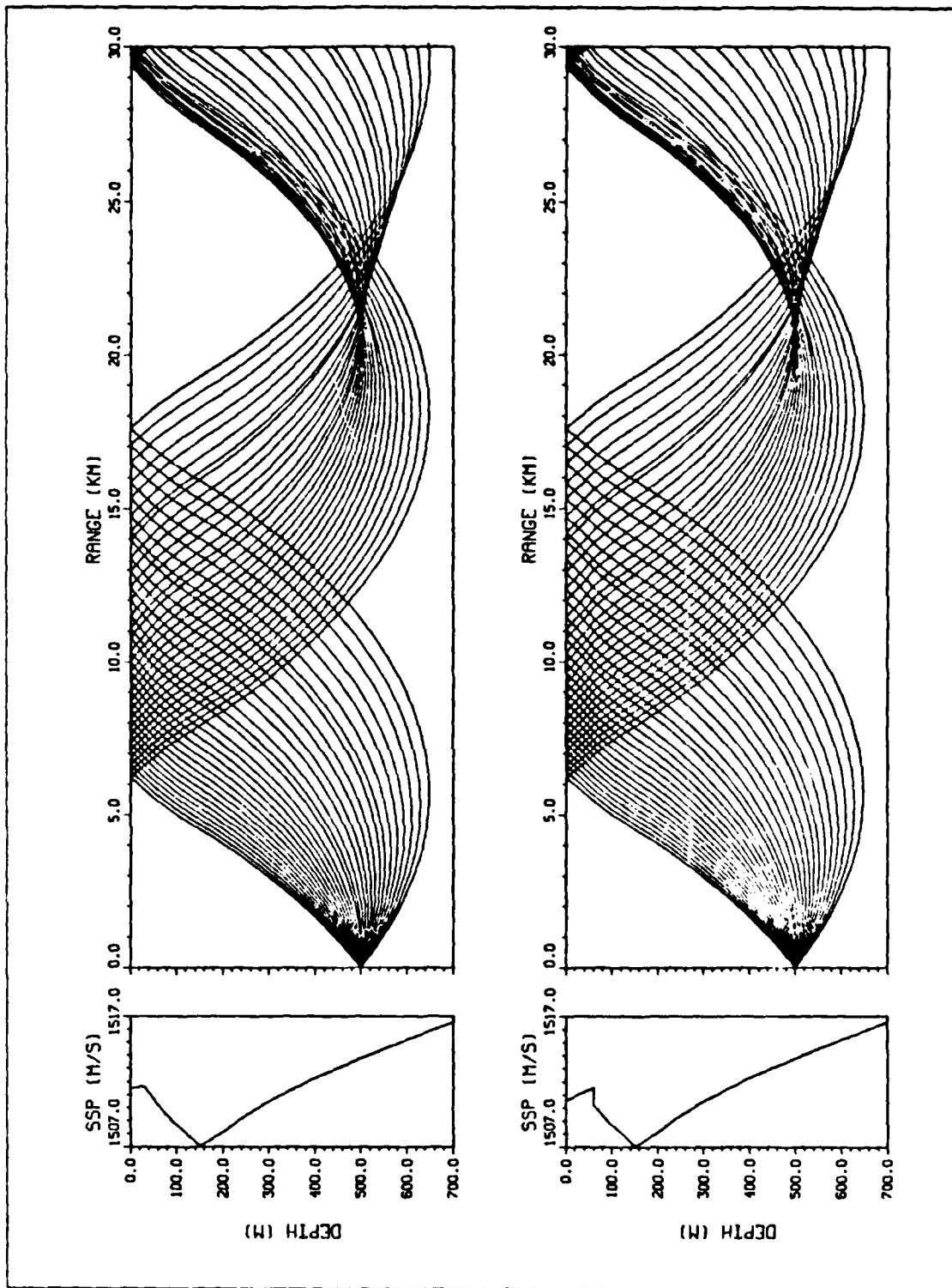


Figure 5.15 December, strong wind, source at 500 m: $t = 0,24$ hrs, $\theta = 6^\circ$.

D. FEBRUARY CASE

1. Source at 10 meters

a. Strong wind conditions (30 knots)

Table 6 shows the evolution of the mixed layer depth for different cloud and rain conditions. In all the cases, the mixed layer deepens mainly because of the wind stirring and, as we saw previously in the December case, adding clouds to the simulation increases the deepening of the mixed layer, while the rain reduces slightly this effect.

TABLE 6
EVOLUTION OF THE MIXED LAYER DEPTH
IN FEBRUARY WITH A STRONG WIND

t(hr)	no rain	no rain	no rain	heavy rain for 12 hrs
	no clouds	50% Q_s	20% Q_s	20% Q_s
	h(m)	h(m)	h(m)	h(m)
0	70.0	70.0	70.0	70.0
12	77.6	79.5	80.5	76.8
24	85.5	87.3	88.3	84.9
36	89.1	92.3	94.1	90.8
48	94.5	97.7	99.5	96.3
60	96.9	101.3	103.8	100.7
72	101.2	105.6	108.0	104.7

The initial mixed layer depth extracted by the OBL model is 70 meters. In this model, the criterion on which is based the choice of this depth is the following :

$$|\Delta b| = |\alpha g \Delta T - \beta g \Delta S| > 0.04 \text{ cm s}^{-2} \quad (5.6)$$

where the symbol Δ represents the variation of buoyancy, temperature, and salinity for an increment of one meter depth. A higher value for the criterion (0.05 for instance) would have increased all the values of the mixed layer depth, but the evolution would have had the same trend as the case depicted in Table 6.

However, independent of the choice of the criterion for the mixed layer depth, the sound-speed profile of Figure 5.16 shows that the water column is mixed almost from the top to the bottom with an average sound-speed gradient dc/dy of 0.02 sec^{-1} . Thus, in February, the main characteristic of the acoustic propagation is a half-duct type of propagation. In the case illustrated by Figure 5.16, the beamwidth has been set to 12° , and the two acoustic ray traces show the situation at time 0 and 24 hours. The wind does not affect the acoustic propagation since the water mass is already almost completely mixed at $t=0$. Nearly identical ray path shapes would have been obtained by assuming clouds and rain.

b. Light wind conditions (5-10 knots)

Table 7, for light wind, no clouds, and no rain conditions, highlights the diurnal variability of the mixed layer depth and illustrates how the surface waters of the sea warm during the daytime hours on a sunny day, shallowing the mixed layer depth. At night, the deepening and cooling mixed layer returns to a state nearly the same as the initial one. These diurnal changes have a profound effect on sound transmission for a surface-ship sonar as depicted in Figures 5.17 and 5.18.

In Figure 5.17, we simulate a light wind of 5 knots with no clouds and no rain. The ray traces are shown at time instant 0 and 12 hours for a beamwidth of 8° . At the end of the daytime ($t=12$ hours), the general shape of the acoustic ray trace is almost the same as the one at the end of the night time ($t=0$ hour), except for the ranges less than 6 km in shallow water. This is depicted in Figure 5.18 at $t=8$ hours, that is, in the middle of the afternoon, for a beamwidth of 6° . This reduction of surface-ship echo ranging on a shallow target is a phenomenon often called the "afternoon effect."

Next, heavy rain is included for 12 hours with light wind conditions. The effect is depicted at time 0 and 12 hours in Figure 5.19, where the wind speed was set equal 10 knots and the beamwidth to 6° . At the initial time, the acoustic energy propagates following a half-duct. At time 12 hours, we find that 62% of the rays are trapped in a shallow surface duct because of the strong discontinuity in the sound-speed profile due to the decrease of salinity in the upper layer of the sea caused by a weak wind stirring and damping of the turbulence by the strong downward surface buoyancy flux associated with the rainfall. However, the overall shape of the acoustic ray trace is not changed significantly. There will be an improved possibility of detection for a shallow target. If the wind continues to blow at 10 knots, the effect remains even 12 hours after the rain has stopped.

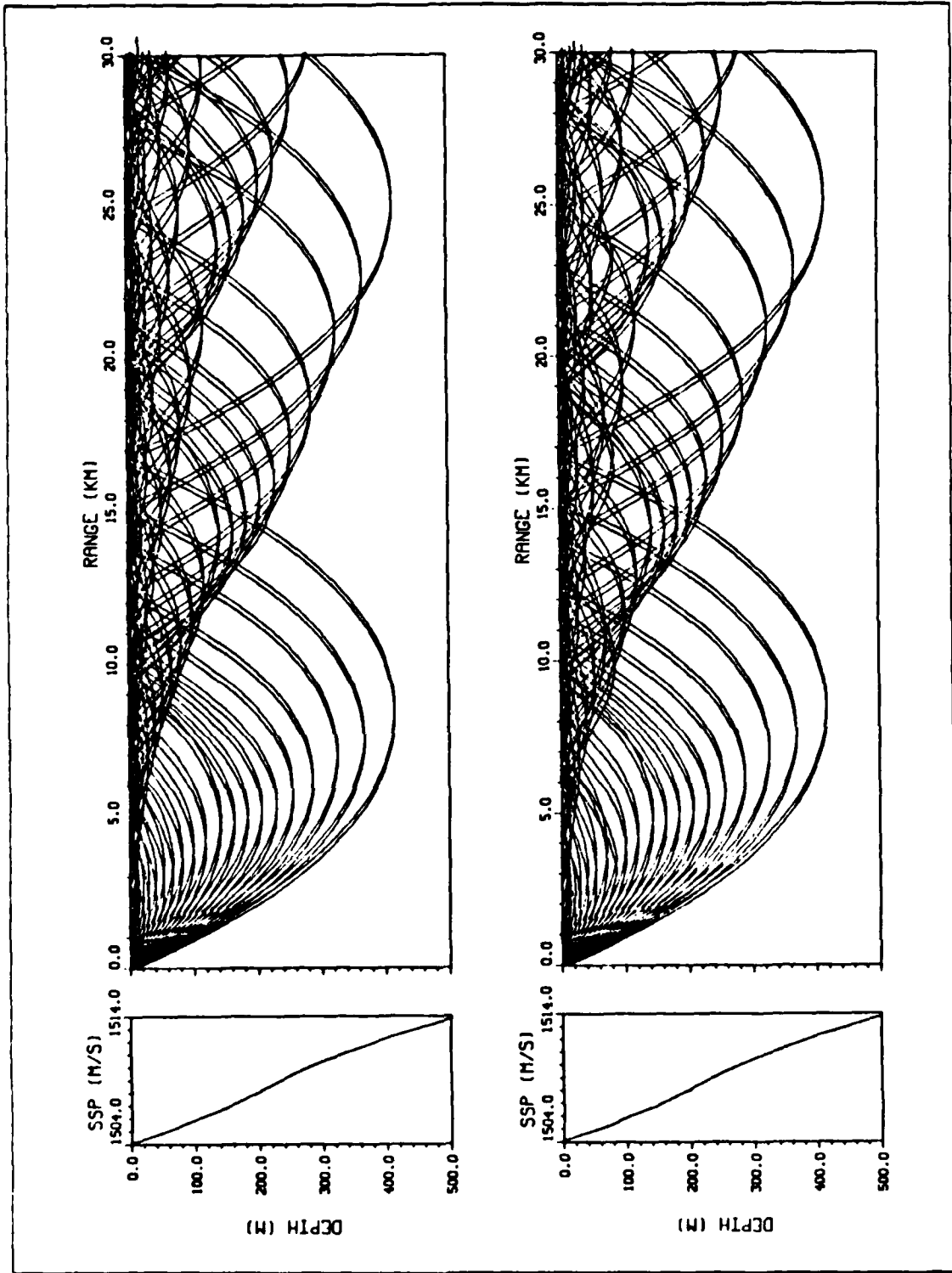


Figure 5.16 February, strong wind, source at 10 meters: $t = 0,24$ hrs, $\theta = 12^\circ$.

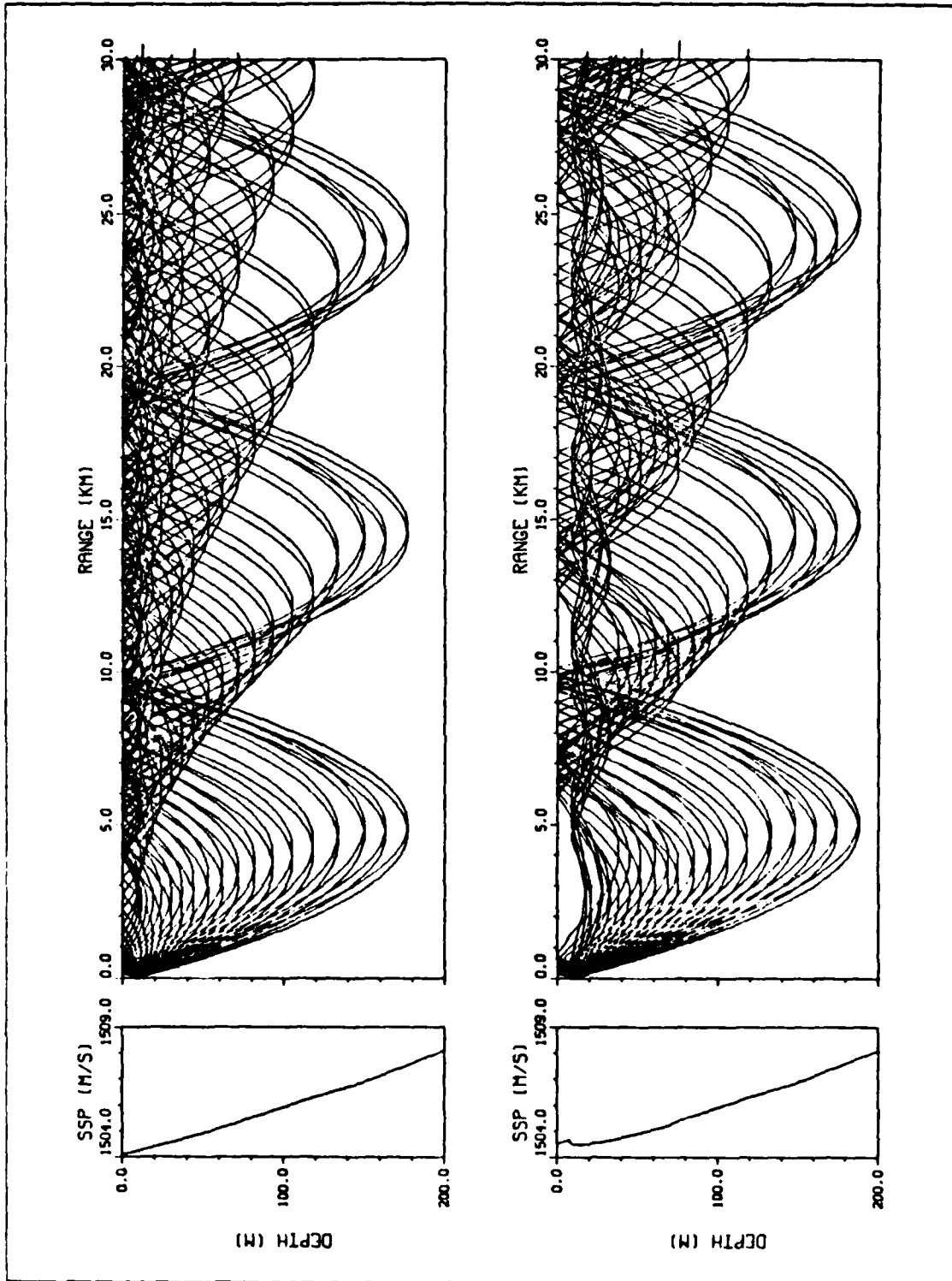


Figure 5.17 February, light wind, source at 10 meters: $t = 0, 12$ hrs, $\theta = 8^\circ$.

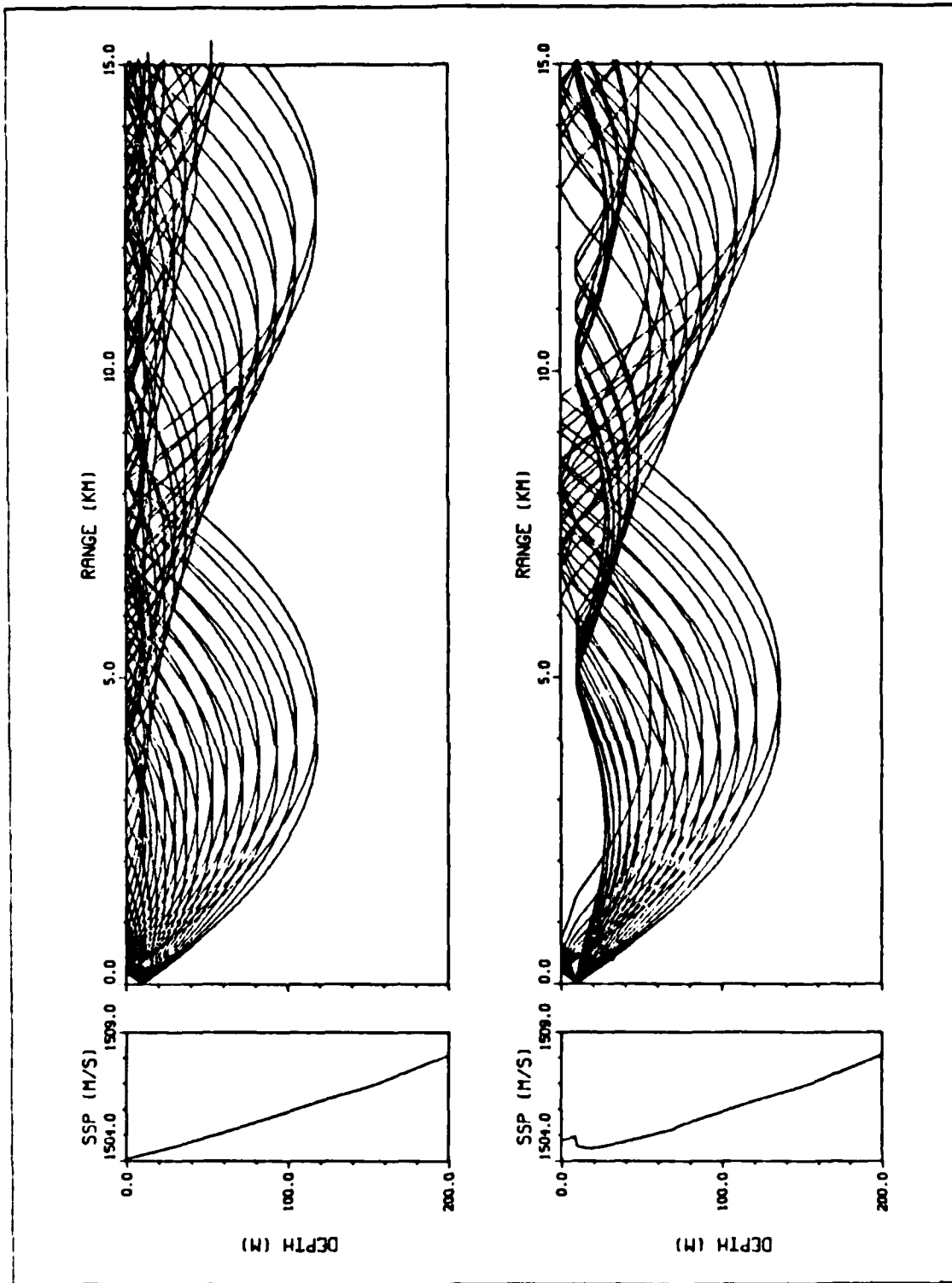


Figure 5.18 February, light wind, source at 10 meters: $t = 0.8$ hrs. $\theta = 6^\circ$.

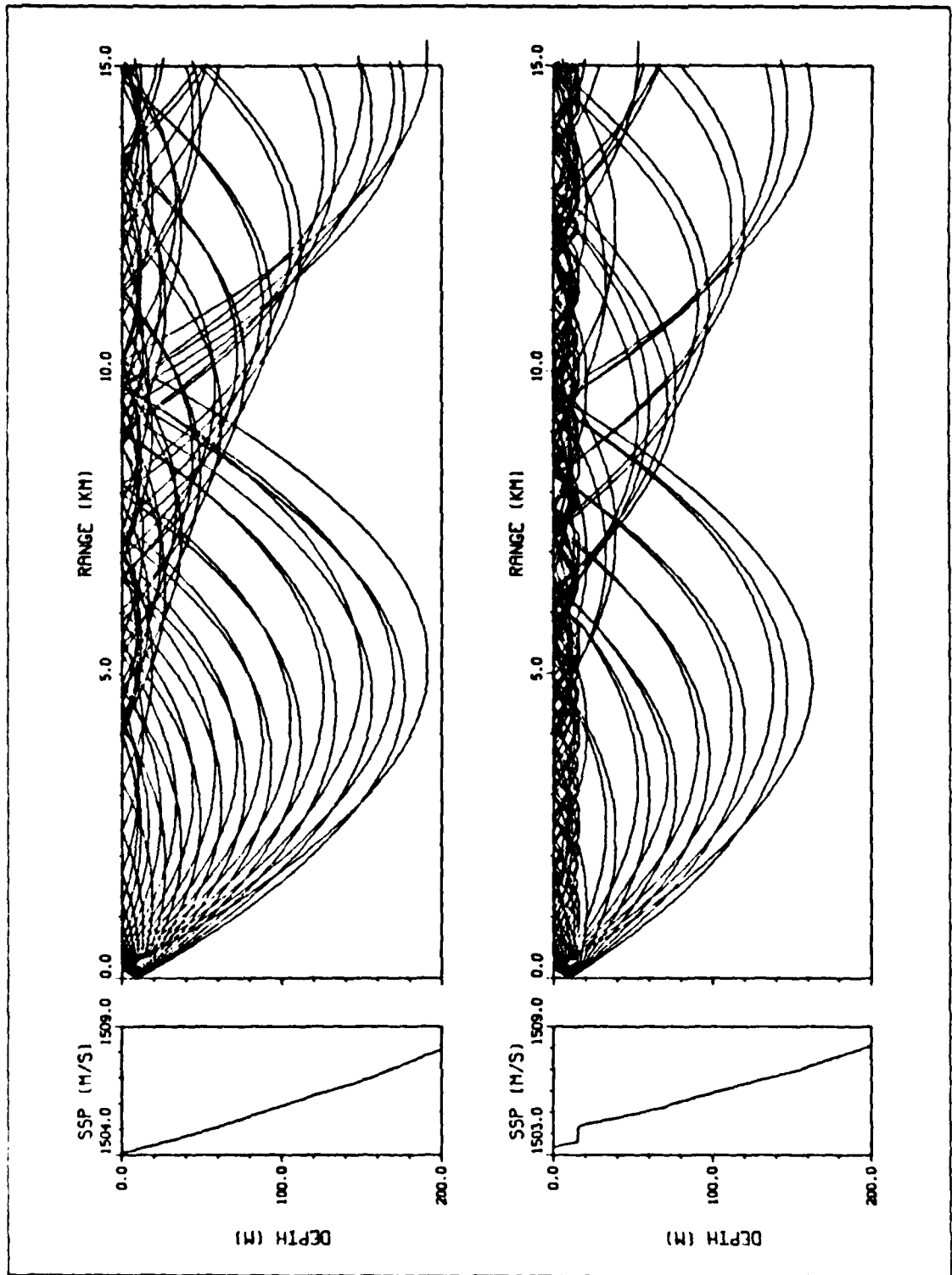


Figure 5.19 February, light wind, heavy rain, source at 10 meters: $t = 0, 12$ hrs, $\theta = 8^\circ$.

2. Source at 200 meters

In this case, we simulate the performance of a sonar towed at a depth of 200 meters. In order to demonstrate that the atmospheric forcing has no effect on sound transmission from a deep source, Figure 5.20 shows the case with a heavy rain for 12 hours together with a light wind of 10 knots. We can see that rain does not influence the acoustic propagation. Whatever the atmospheric conditions in February, a deep towed sonar is able to detect any target moving between 0 and 300 meters. Thus, the half-duct type of propagation is one of the best configurations for underwater detection by deep transmitters.

TABLE 7
EVOLUTION OF THE MIXED LAYER DEPTH
IN FEBRUARY WITH A LIGHT WIND

wind 5 knots no rain no clouds		wind 5 knots heavy rain for 12 hrs 20% Q_s		wind 10 knots heavy rain for 12 hrs 20% Q_s	
t(hr)	h(m)	t(hr)	h(m)	t(hr)	h(m)
0	70.0	0	70.0	0	70.0
12	7.6	12	2.1	12	12.9
24	69.0	16	3.3	20	14.0
36	7.6	20	7.9	24	16.8
48	69.1	24	67.8	36	33.7
60	7.6	36	70.9	48	70.8
72	69.3	48	73.2	60	73.0

3. Conclusions for February

As in December, the atmospheric conditions do not influence the acoustic propagation for rays emanating from a deep towed sonar.

Compared to December, the SOFAR channel has disappeared, and there is a completely asymmetrical, surface-bounded channel (or half-duct) inside which the

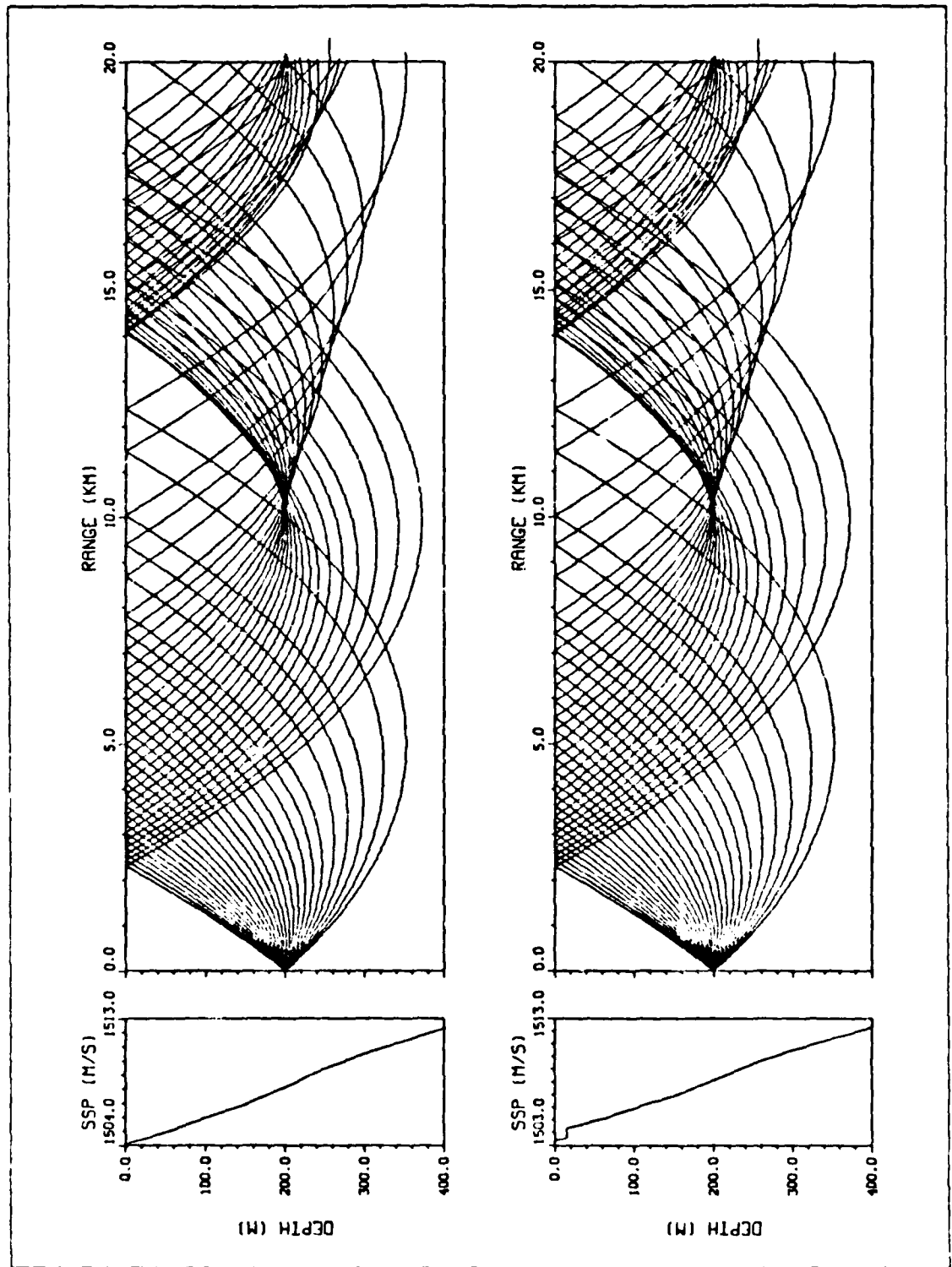


Figure 5.20 February, light wind, heavy rain, source at 200 meters: $t = 0.12$ hrs, $\theta = 8^\circ$.

propagation is made of R-SR rays only. Because of this half-duct type of propagation, February is one of the best months in the Mediterranean for underwater detection by both deep and shallow transmitters. This generalisation not take in consideration the sea state which can generate noise and reflection loss when the sea is rough, because our acoustic model assumes a perfect surface reflection.

With light wind conditions, surface-ship echo ranging can be poorer in the afternoon on a shallow target because of the "afternoon effect" due to surface water heating.

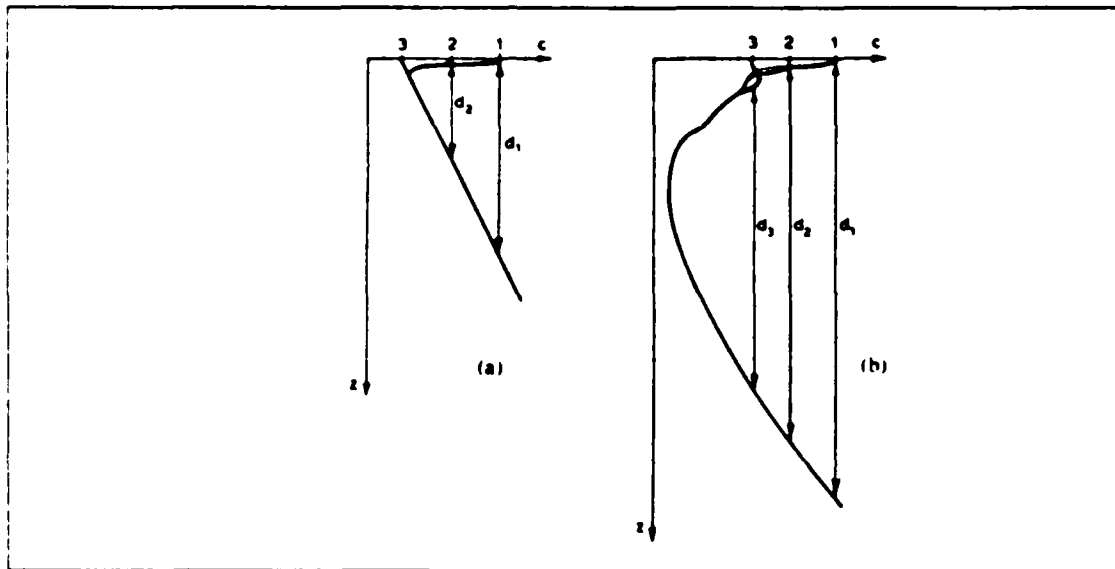


Figure 5.21 Variation of sound-channel width d for similar temperature changes in (a) the Mediterranean and (b) the Atlantic.

E. JUNE CASE

Figures 5.3 and 5.4 show that the shape of the sound-speed profile stays approximatively the same during the entire summer season, that is, from June to September. Therefore, in this section, we will just simulate the atmospheric conditions and the acoustic propagation in June. All of our observations will be applicable to the other months of summer time even though the atmospheric factors change somewhat, as illustrated in Table 3.

In summer, so much heat is added to the upper layer of the Mediterranean Sea that negative gradients in temperature and, thus, in sound-speed develop in the upper

layer of the sea. This is underlain by isothermal water at a relatively shallow depth. The consequence is that a sound channel exists in summer in the Mediterranean and is characterized as follows:

The sound channel is, in all cases, strongly asymmetrical. The sound-speed profile contains a sharp discontinuity between sound-speed gradients of completely different orders of magnitude: 0.017 sec^{-1} on the lower side, due to the pressure effect, and -1 to -5 sec^{-1} on the upper side in the thermocline.

TABLE 8
EVOLUTION OF THE MIXED LAYER DEPTH
IN JUNE WITH STRONG WINDS

t(hr)	no rain	no rain	no rain	heavy rain for 12 hrs
	no clouds	50% Q_s	20% Q_s	20% Q_s
	h(m)	h(m)	h(m)	h(m)
0	2.0	2.0	2.0	2.0
12	20.3	20.8	21.1	20.3
24	25.7	26.2	26.5	25.8
36	29.4	30.3	30.8	30.0
48	32.9	33.9	34.5	33.6
60	35.5	36.9	37.7	36.8
72	38.3	39.8	40.7	39.8

The sound channel axis is very close to the surface, and the curvature of the sound-speed profile near this minimum is very great.

The width of the sound channel is smaller than in the Atlantic and is extremely variable with the temperature of the surface water, as depicted in Figure 5.21. The usual width of the sound channel in summer is on the order of 1400 to 1800 meters. The depth of the Mediterranean is sufficient for this channel not to be intercepted by the sea bottom in most cases.

1. Source at 10 meters

a. Strong wind conditions (30 knots)

The evolution of the mixed layer depth h for different cases is shown in Table 8. In the case of no clouds and no rain, we find that the mixed layer depth increases significantly during the first 12 hours because of the strong wind mixing in spite of the strong summer time heating. As seen in the previous sections, for short time scales, the wind is the dominating factor influencing both the mixed layer depth and the acoustic propagation.

Figure 5.22 shows the acoustic ray trace at time 0 for a beamwidth $\theta = 8^\circ$. After 24 hours of 30 knot winds, the mixed layer deepens to 25.7 meters. Even if the convergence zone weakens slightly, the range of the CZ is not affected. However, the acoustic propagation changes greatly for the less steep rays. Thirty percent of the rays are now trapped in a shallow mixed layer, improving slightly the probability of detection using a surface-ship sonar. However, the unfavorable conditions for underwater detection for a shallow source is well depicted in Figure 5.23.

TABLE 9
MAXIMUM AND MINIMUM ML DEPTHS AND TEMPERATURES
IN JUNE FOR LIGHT WIND CONDITIONS WITH NO CLOUDS

day 2	9a.m.	$h = 4.8\text{m}$	$T = 20.13^\circ\text{C}$
	5 p.m.	$h = 1.1\text{m}$	$T = 21.31^\circ\text{C}$
day 3	9a.m.	$h = 5.4\text{m}$	$T = 20.15^\circ\text{C}$
	5p.m.	$h = 1.1\text{m}$	$T = 21.33^\circ\text{C}$
day 4	9a.m.	$h = 5.6\text{m}$	$T = 20.21^\circ\text{C}$
	5p.m.	$h = 1.1\text{m}$	$T = 21.39^\circ\text{C}$

b. Light wind conditions (5 knots)

Table 9 shows the evolution of the maximum and minimum mixed layer depths and high temperatures rise during light wind conditions with no clouds. The mixed layer responds to the diurnal cycle of solar radiation, shallowing in daytime because of solar heating, and deepening at night because of surface cooling. We notice

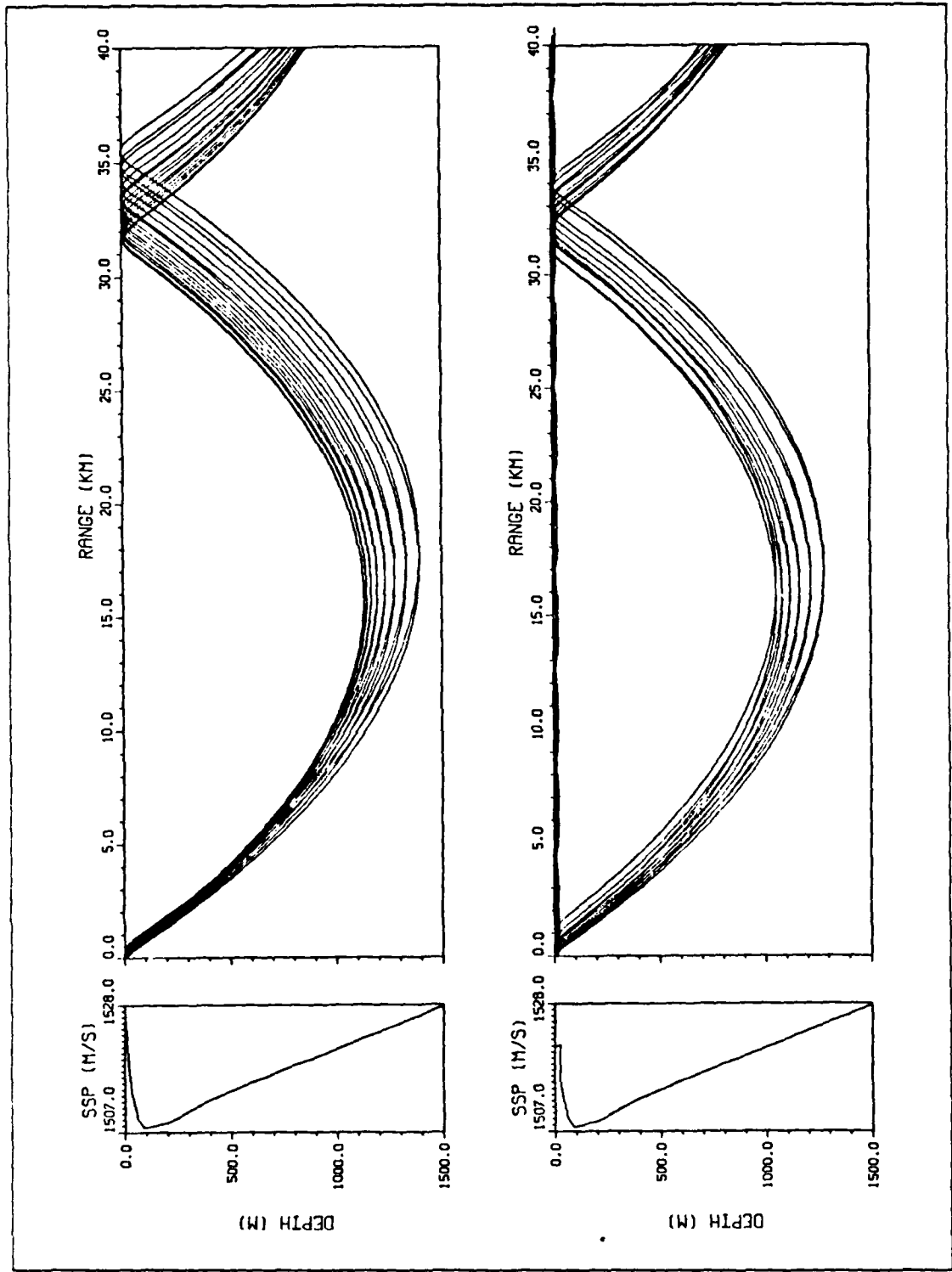


Figure 5.22 June, strong wind, source at 10m: $t = 0,24$ hrs, $\theta = 8^\circ$.

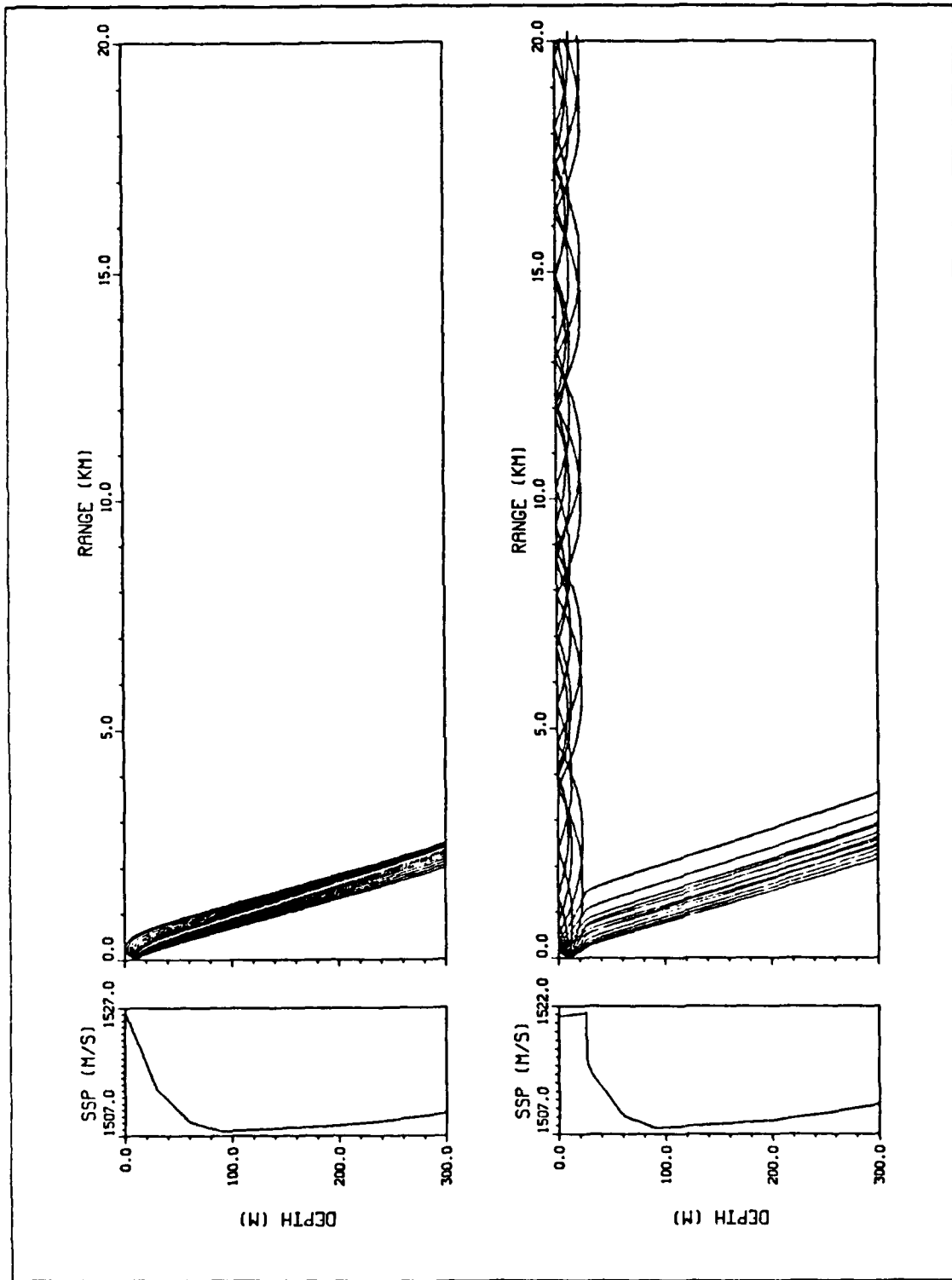


Figure 5.23 June, strong wind, source at 10m: $t = 0.24$ hrs, $\theta = 8^\circ$.

that the general trend of the minimum and maximum temperature is to increase, leading progressively to the extreme sound-speed profile of August (see Figure 5.4). Nevertheless, the mixed layer stays sufficiently shallow not to influence the acoustic propagation, even for a shallow transmitter.

Adding clouds to the simulation (20% Q_s) only deepens the mixed layer to 9 meters after 48 hours, which has almost no effect on the acoustic propagation. A longer period of cloud covering would not be a realistic simulation for summertime in the Mediterranean.

Finally, heavy rain keeps the mixed layer shallow (around 1.5 meters), and sound propagation is not influenced.

2. Source on the SOFAR axis (90 meters)

Figure 5.24 simulates the case where the source is on the shallow sound-channel axis characterizing the Mediterranean summer time. The beamwidth is set to 8° . The strong asymmetry of the sound channel is readily apparent. As previously mentioned, the wind does not influence the sound channel propagation for $\theta = 8^\circ$. The rays at the source are not sufficiently steep to be affected and, even if the sound channel width decreases, the propagation does not change.

However, in order to study the effect due to the decrease of the sound channel width, Figure 5.25 shows the ray traces for steep initial angles $\beta = 81^\circ, 82^\circ, 83^\circ, 97^\circ, 98^\circ, \text{ and } 99^\circ$ at time 0 and after 48 hours of strong winds (30 knots). The channel width decreases from 1400 to 900 meters. The steepest rays ($\beta = 81^\circ, 82^\circ, 98^\circ, \text{ and } 99^\circ$) are transformed from RR type to R-SR type, but the influence of this phenomenon on the acoustic propagation is almost not perceptible with an acoustic ray tracing model as shown by Figure 5.25. A transmission loss model would be necessary to account for the transmission loss due to the reflection on a rough sea surface.

3. Conclusions for June

In June, and for the remainder of the summer, the sound propagation for a deep transmitter is characterized by a sound-channel type of propagation and is not influenced by the atmospheric forcing on a short time scale of a few days.

Because of the absence of a mixed layer and the presence of a sharp thermocline due to the important effect of surface heating, the detection capabilities of a surface-ship sonar are poor and limited to the convergence zone with ranges between 30 and 35 km. However, strong winds can create a shallow mixed layer in which shallow targets could be detected as depicted in Figure 5.26, where rays emanating from both shallow and deep transmitters are traced.

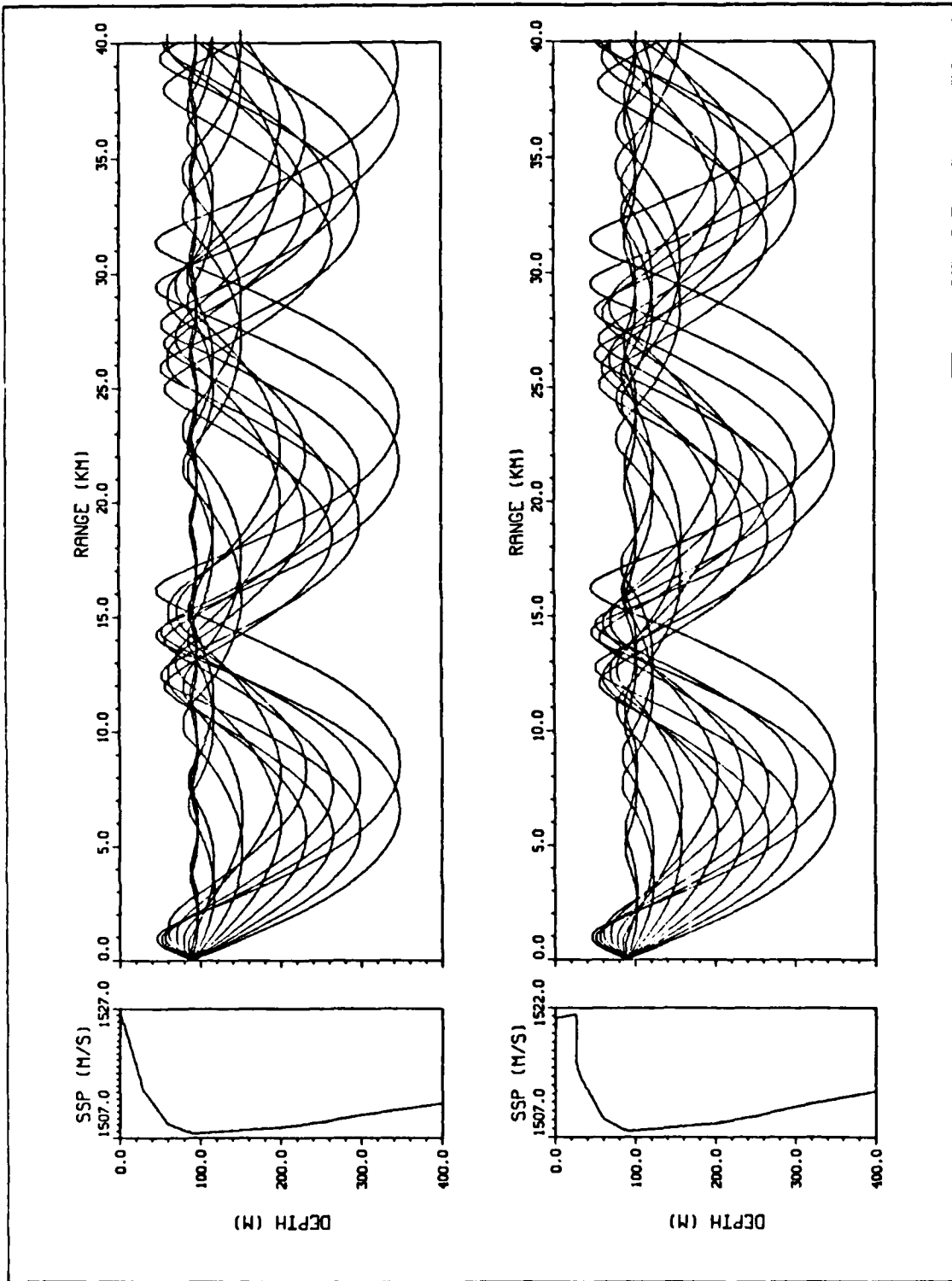


Figure 5.24 June, strong wind, source at 90 meters: $t = 0,24$ hrs, $\theta = 8^\circ$.

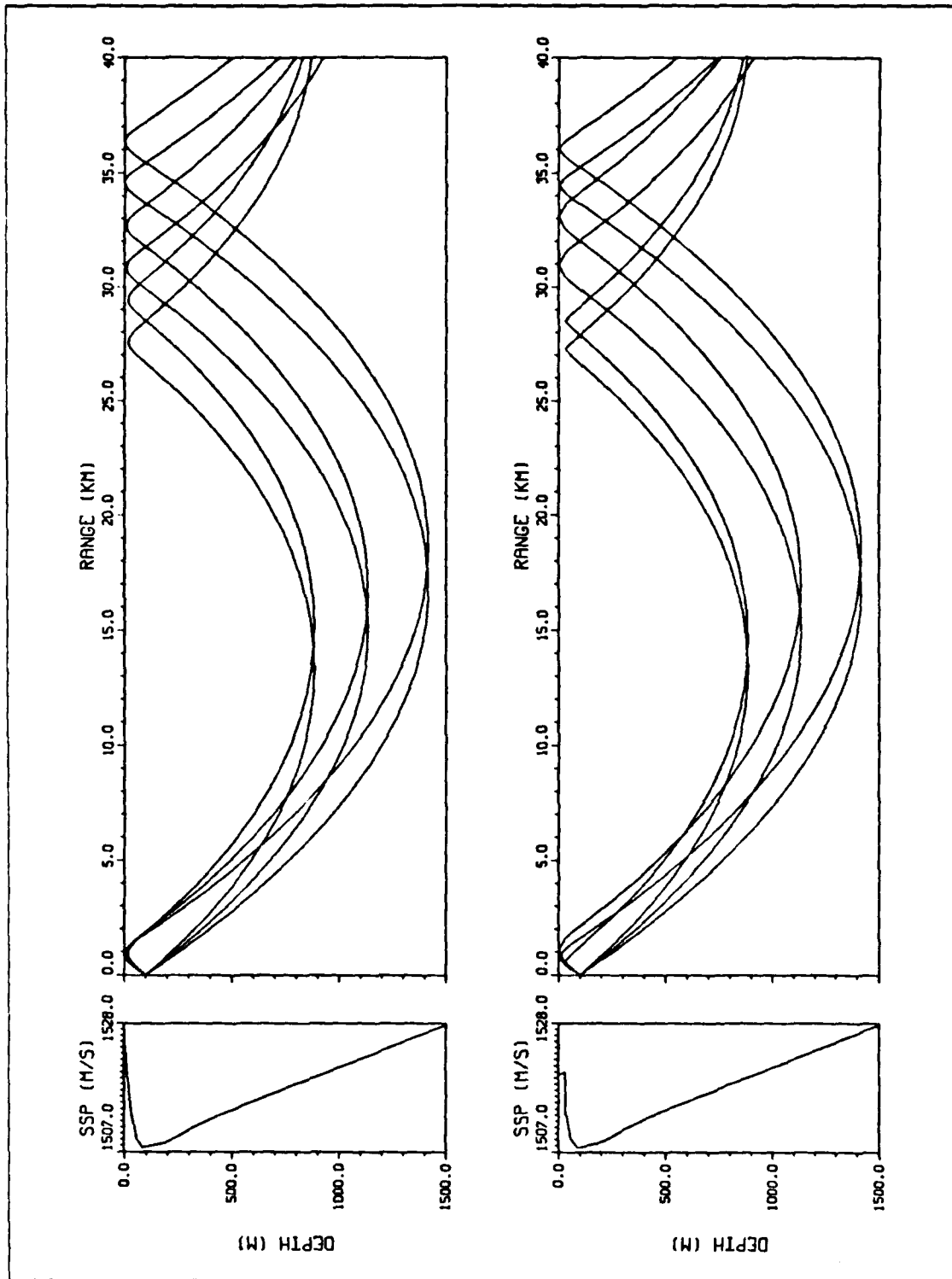


Figure 5.25 June, strong wind, source at 90 meters, $t = 0,48$ hrs, $\beta = 81^\circ, 82^\circ, 83^\circ, 97^\circ, 98^\circ, 99^\circ$.

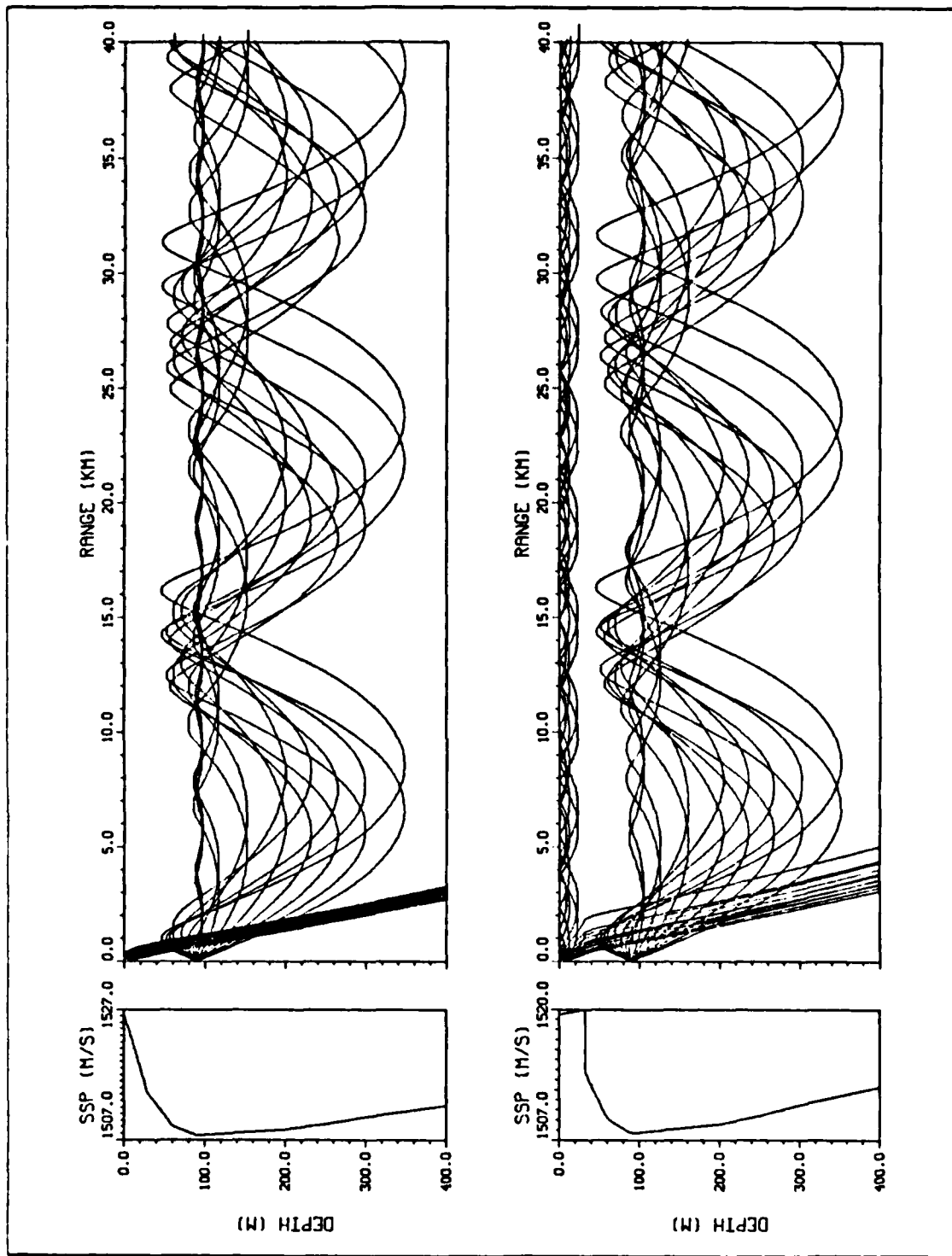


Figure 5.26 June, strong wind, sources at 10 and 90 meters
 $t = 0.48$ hrs, $\theta = 8^\circ$.

VI. CONCLUSION

On a short time scale of a few hours to three days, the atmospheric conditions influence the acoustic propagation only for a shallow source. The ray trace emanating from a deep transmitter is almost not affected by the atmospheric forcing. This conclusion is independent of the type of propagation, depending on the time of the year (deep-sound channel, convergence zone, or half duct).

The wind is the dominant atmospheric factor. For short time scales, the coupled model is not very sensitive to the other boundary conditions (solar irradiation, and rainfall). This is a favorable finding in the sense that the wind is the easiest parameter to measure and to forecast at sea. However, the importance of a heavy rainfall has been demonstrated in the case of light wind conditions.

The initial temperature profile plays a determinant role and has to be provided as accurately as possible. The coupled model is not very sensitive to the initial salinity profile.

A. ADVANTAGES OF THE COUPLED MODEL

The graphic output sequence from the coupled model shows qualitatively the acoustic propagation and its evolution under the forcing of specified atmospheric conditions, and an assumed initial temperature profile.

The simplicity of the model makes it possible to be implemented on a simple desktop computer with some graphics capability.

A current XBT, digitized by using a one-meter depth increment, can be used as input in the model.

B. WEAKNESS OF THE COUPLED MODEL

The fact that the coupled model does not account very well for the operating frequency is inherent to a ray tracing routine. The user of such a model will have to simulate a beamwidth at the source corresponding approximatively to a given frequency.

The output of the coupled model does not provide such quantitative results as median detection range, convergence zone range, S/N ratio at the receiver, and it does not account for scattering and attenuation.

Perfect surface reflection has been assumed whatever the sea-state. An infinitely-deep ocean has been assumed in order to avoid the complication of bottom reflection. However, the model can handle perfect bottom reflection or absorption. Furthermore, the earth curvature has been neglected.

The coupled model assumes horizontal homogeneity of the water mass, which we considered to be realistic for the horizontal ranges considered.

Finally, we neglected horizontal advection, which is compatible with the short time scales studied, especially in the Mediterranean where the currents are weak.

C. RECOMMENDATIONS

Further simulations could be applied to different locations in the Atlantic, Pacific, or Indian Oceans, where climatology is more available.

Real data could be used to initialize the coupled model and the boundary conditions could be computed from observed atmospheric and oceanic conditions. The resulting outputs of the model could be compared with corresponding simulations.

Then, one might couple the OBL model with one of the different acoustic models used by the US Navy (such as RAYMODE, FACT, or PE models) in order to obtain quantitative results including MDR or CZR for usual operating frequencies and a variety of environmental conditions.

APPENDIX

RAY TRACING SUBROUTINE USE EXAMPLE

File giving an example of sound speed profile to be used with RAY :

```

0.    1482.
30.   1482.9
55.   1484.1
90.   1480.5
150.  1482.
225.  1484.1
300.  1486.2

```

```

C    LCDR JACQUES FOURNIOL. FRENCH NAVY.
      PARAMETER (YO=50.,BO=90.,DB=.5,M=7,MM=6,N=300,NN=5000,RANGE=30.)
      DIMENSION BET(M),CC(0:MM),YY(0:MM)
      DIMENSION C(0:N),G(-1:N),YC(0:N)
      DIMENSION Y(0:NN),Z(0:NN)
      READ(05,10)(YY(I),CC(I),I=0,MM)
10    FORMAT(F7.2,2X,F7.2)
      CALL RAY(YO,BET,BO,DB,M,CC,YY,MM,C,G,YC,N,Y,Z,NN,RANGE)
      STOP
      END

```

```

C
C
C    SUBROUTINE USING THE MM+1 POINTS OF A STRAIGHT LINE SEGMENT
C    CONTINUOUS PROFILE ( CC VS YY ) TO TRACE M ACOUSTIC RAYS ISSUED
C    FROM A SOURCE AT A DEPTH YO.
C    REF. "UNDERWATER ACOUSTICS-A LINEAR SYSTEMS THEORY APPROACH"
C    BY ZIOMEK L. P237-238. ACADEMIC PRESS, ORLANDO, FLORIDA. 1985.
C    PERFECT SURFACE AND BOTTOM REFLECTIONS. FLAT BOTTOM.
C    BETA0 : STARTING ANGLE OF RAY, REF VERTICAL, IN RAD.
C    M      : NB OF RAYS SENT.
C    BET    : ARRAY OF THE INITIAL ANGLES IN DEGREES AT THE SOURCE.
C    BO     : INITIAL ANGLE OF THE UPPER RAY OF THE BUNDLE.
C    DB     : INCREMENT OF INITIAL ANGLES IN BET.
C    YO     : SOURCE DEPTH IN METER.
C    MM+1   : NB OF PTS IN PROVIDED SSP.
C    CC     : PROVIDED SSP IN M/SEC.
C    YY     : DEPTH OF THE PTS OF THIS SSP IN METERS.
C    NN     : INDEX OF RANGE.
C    Y      : DEPTH IN METERS AND
C    Z      : HOR. DISTANCE TRAVELLED BY A RAY IN KM.
C    N      : MAX INTEGER VALUE OF DEPTH IN METER.
C    C      : SSP .1 METER INCREMENT.

```

```

C      G      : GRADIENT OF SSP.
C      YC     : ARRAY OF DEPTH FOR PLOTTING SSP.
C      RANGE  : MAX. RANGE OF THE PLOTIN KM.
C      K      : DEPTH INDEX.
C      N MUST BE THE INTEGER VALUE OF THE MAX. DEPTH YY(MM) OF THE
C      INITIAL SSP.
C
C      SUBROUTINE RAY(YO,BET,BO,DB,M,CC,YY,MM,C,G,YC,N,Y,Z,NN,RANGE)
C
C      DIMENSION BET(M),CC(0:MM),YY(0:MM)
C      DIMENSION C(0:N),G(-1:N),YC(0:N)
C      DIMENSION Y(0:NN),Z(0:NN)
C      DATA PI/3.141592654/
C      Y(0)=YY(0)
C      YC(0)=YY(0)
C      JMIN=0
C      C(0)=CC(0)
C
C      COMPUTE THE SSP C AND ITS GRADIENT G WITH 1 METER DEPTH INCREMENT
C      DO 10 I=1,MM
C          DYY=YY(I)-YY(I-1)
C          JMAX=IFIX(YY(I))
C          GG=(CC(I)-CC(I-1))/DYY
C          DO 30 J=JMIN,JMAX-1
C              G(J)=GG
C              C(J+1)=C(J)+GG
30          YC(J+1)=FLOAT(J+1)
C              JMIN=JMAX
10      CONTINUE
C
C      CREATE GRADIENT AT SFC AND BOTTOM TO HANDLE REFLECTION
C      G(-1)=G(0)
C      G(N)=G(N-1)
C
C      DO 03 J=1,M
C03     BET(J)=90.-FLOAT(J)*0.5
C          DO 03 J=1,M
03     BET(J)=BO-FLOAT(J)*DELB
C
C      RESEARCH OF CMIN AND CMAX FOR PLOTTING
C      CMIN=1550.
C      CMAX=1450.
C      DO 40 I=0,N
C          CMIN=AMIN1(CMIN,C(I))
40     CMAX=AMAX1(CMAX,C(I))
C          CMIN=AIN1(CMIN)
C          CMAX=AIN1(CMAX)+1.

```

```

C
C
C   PLOT THE SSP AND PREPARE PLOT FOR RAYS
C   CALL COMPRS
C   CALL CX41(4107)
C   CALL TEK618
C   CALL SHERPA('THESEOUT','B',1)
C   CALL HWROT('AUTO')
C   CALL BLCWUP(0.745)
C   CALL PAGE(11.,5.5)
C   CALL PHYSOR(1.2,1.)
C   CALL AREA2D(1.,3.)
C   CALL THKFRM(.01)
C   CALL XNAME('SSP (M/S)$',-100)
C   CALL YNAME('DEPTH (M)$',100)
C   CALL CROSS
C   CALL YAXANG(0.)
C   CALL YTICKS(5)
C   CALL XTICKS(IFIX(CMAX-CMIN))
C   CALL GRAF(CMIN,CMAX-CMIN,CMAX,FLOAT(N),-50.,0.)
C   CALL CURVE(C,YC,N+1,0)
C   CALL FRAME
C   CALL ENDGR(0)
C   CALL PHYSOR(2.7,1.)
C   CALL AREA2D(7.3,3.)
C   CALL XNAME('RANGE (KM)$',-100)
C   CALL YNAME('$',100)
C   CALL YNONUM
C   CALL CROSS
C   CALL XTICKS(5)
C   CALL GRAF(0.,5.,RANGE,FLOAT(N),-50.,0.)
C
C   DO 05 J=1,M
C   Y(0)=Y0
C   Z(0)=0.
C   K=IFIX(Y0)
C   BETA0=BET(J)/180.*PI
C   CO=C(K)
C   B=SIN(BETA0)/CO
C
C
C   DO 20 I=1,NN
C   NNN=I
C
C   CHECK IF SFC REFLECTION
C   IF (K.EQ.0) BETA0=PI-BETA0
C

```



```

IF((G(K).LT.0.).AND.(G(K-1).GT.0.)) THEN
  IF (BETA0.GT.PI/2.) THEN
    K=K-1
    BETA=PI-ASIN(B*C(K))
    Y(I)=FLOAT(K)
    Z(I)=Z(I-1)+(COS(BETA0)-COS(BETA))/(B*G(K))
    BETA0=BETA
  ELSE
    K=K+1
    BETA=ASIN(B*C(K))
    Y(I)=FLOAT(K)
    Z(I)=Z(I-1)+(COS(BETA0)-COS(BETA))/(B*G(K-1))
    BETA0=BETA
  ENDIF
ELSE
  IF ((G(K).GT.0.).AND.(G(K-1).LT.0.)) THEN
    IF (BETA0.GT.PI/2.) THEN
      BETAC=PI-ASIN(C(K)/C(K-1))
      IF (BETA0.GT.BETAC) THEN
        K=K-1
        BETA=PI-ASIN(B*C(K))
        Y(I)=FLOAT(K)
        Z(I)=Z(I-1)+(COS(BETA0)-COS(BETA))/(B*G(K))
        BETA0=BETA
      ELSE
        Y(I)=FLOAT(K)
        Z(I)=Z(I-1)+2.*COS(BETA0)/(B*G(K-1))
        BETA0=PI-BETA0
      ENDIF
    ELSE
      BETAC=ASIN(C(K)/C(K+1))
      IF (BETA0.LT.BETAC) THEN
        K=K+1
        BETA=ASIN(B*C(K))
        Y(I)=FLOAT(K)
        Z(I)=Z(I-1)+(COS(BETA0)-COS(BETA))/(B*G(K-1))
        BETA0=BETA
      ELSE
        Y(I)=FLOAT(K)
        Z(I)=Z(I-1)+2.*COS(BETA0)/(B*G(K))
        BETA0=PI-BETA0
      ENDIF
    ENDIF
  ENDIF
ENDIF
ENDIF
ENDIF
ENDIF
ENDIF

```

AD-A184 357

COUPLED ACOUSTIC AND OCEAN THERMODYNAMIC MODEL(U) NAVAL
POSTGRADUATE SCHOOL MONTEREY CA J M FOURNIOU JUN 87

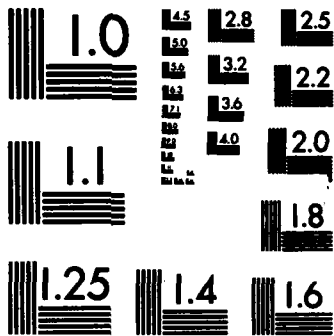
2/2

UNCLASSIFIED

F/G 20/1

NL





MICROCOPY RESOLUTION TEST CHART
NATIONAL BUREAU OF STANDARDS-1963-A

```
                IF(Z(I).GT.RANGE*1000.) GO TO 21
20             CONTINUE
C
C
21             CONTINUE
C
C             CONVERSION M TO KM
                DO 50 I=0,NNN
50             Z(I)=Z(I)*0.001
C
C
C             PLOT THE RAYS
                CALL CURVE(Z,Y,NNN+1,0)
C
05            CONTINUE
C
                CALL FRAME
C             CALL HEADIN('ACOUSTIC RAY TRACINGS',100,2.,1)
                CALL ENDPL(0)
                CALL DONEPL
                STOP
                END
```

LIST OF REFERENCES

1. Garwood, R. *A General Model of the Ocean Mixed Layer*. NOAA Technical Report ERL 384-PMEL 27. September 1976.
2. Fisher, R.H. *Variability and sensitivity of coupled mixed layer-acoustic systems*. M.S. Thesis, Naval Postgraduate School, Monterey, California, March 1981.
3. McManus, J.J. *Coupled mixed layer-acoustic model*. M.S. Thesis, Naval Postgraduate School, Monterey, California, September 1985.
4. Ziomek, L. *Underwater Acoustics-A Linear Systems Theory Approach*. Academic Press, Orlando, Florida, 1985.
5. Garwood, R. *An Oceanic Mixed Layer Model Capable of Simulating Cyclic States*. *J. Phys. Oceanogr.*, 7:455-468, 1977.
6. Adamec, D., Elsberry, R., Garwood, R., and Haney, R. *An Embedded Mixed Layer Ocean Circulation Model*. *Dyn. Atmos. Oceans*, 6:69-96, 1981.
7. Miller, A.R., Tchernia, P., Charnock, H., and McGill, D.A. *Mediterranean Sea Atlas*. WHOI, Woods Hole, Massachusetts, 1970.
8. Chen, C.T. and Millero, F.J. *Speed of sound in sea water at high pressures*. *JASA*, 62:1129, 1977.
9. Del Grosso, V.A. *New equations for the speed of sound in natural waters (with comparisons to other equations)*. *JASA*, 56:1084, 1974.
10. Wilson, W.D. *Speed of sound in sea water as a function of temperature, salinity and pressure*. *JASA*, 32:641, 1960.
11. Urick, R.J. *Principles of Underwater Sound*. 3rd ed. Mc Graw Hill Book Company, 1983.
12. Coppens, A.B. *JASA*, 69:382, 1981.
13. Tchernia, P. *Descriptive Regional Oceanography*. Vol. 3, Pergamon Marine series, 1980.

14. Leroy, C.C. *Sound Propagation in the Mediterranean Sea*, in V.M. Albers (ed.), *Under-water Acoustics*, vol.2, p203. Plenum Press. New York. 1967.
15. Sound-speed profiles for the Mediterranean. NUSC Technical Document 6309.
16. Levastu, T. et al. *Annual cycles of heat in the Northern Hemisphere oceans and heat distribution by ocean currents*. FNWC. Tech.note AD-A018 275. Janvier 1970.
17. Bethoux, J.P. *Budgets of the Mediterranean Sea. Their dependence on the local climate and on the characteristics of the Atlantic waters*. *Oceanologica Acta*. vol.2 (2):157-163.1979.
18. Bunker, A.F., Charnock, H., and Goldsmith, R.A. *A note on the heat balance of the Mediterranean and Red Seas*. *J.Mar.Research*. vol 40-suppl.:73-84. 1982.
19. Colacino, M., and Dell'Osso, L. *The monthly Heat Budget Isolines on the Mediterranean Sea*. *Arch. Met. Geoph.Biokl., Ser.A*, 24:171-178, 1975.

INITIAL DISTRIBUTION LIST

		No. Copies
1.	Defense Technical Information Center Cameron Station Alexandria, VA 22304-6145	2
2.	Library, Code 0142 Naval Postgraduate School Monterey, CA 93943-5002	2
3.	Professor E. B. Thornton, Chairman, code 68Tm Department of Oceanography Naval Postgraduate School Monterey, CA 93943	1
4.	Professor J. P. Powers, Chairman, code 62Po Department of Electrical and Computer Engineering Naval Postgraduate School Monterey, CA 93943	1
5.	Professor R. W. Garwood, code 68Gd Department of Oceanography Naval Postgraduate School Monterey, CA 93943	2
6.	Professor L. J. Ziomek, code 62Zm Department of Electrical and Computer Engineering Naval Postgraduate School Monterey, CA 93943	1
7.	Professor C. Dunlap, code 68Du Department of Oceanography Naval Postgraduate School Monterey, CA 93943	1
8.	Professor R.H. Bourke, code 68Bf Department of Oceanography Naval Postgraduate School Monterey, CA 93943	1
9.	Dr. T. W. Spence Physical Oceanography Office of the Chief of Naval Research Arlington, VA 22217-5000	1

- | | | |
|-----|---|---|
| 10. | Monsieur l'Amiral
Chef d'Etat-Major de la Marine
2, rue Royale
75200 Paris Naval, France | 3 |
| 11. | Monsieur le Contre-Amiral
Attache Naval aupres de l'Ambassade de France
4101, Reservoir road NW
Washington D.C. 20007 | 2 |
| 12. | Monsieur le Capitaine de Vaisseau
Commandant le CEPMAN
B.P. 38, 83800 Toulon Naval, France | 2 |
| 13. | Monsieur l'Ingenieur en Chef de l'Armement
Directeur de l'EPSHOM
B.P. 426, 29275 Brest Cedex, France | 1 |
| 14. | Capitaine de Corvette J. Fourniol
Cellule Operationelle d'Environnement de la Marine
2, avenue Rapp
75007 Paris, France | 7 |
| 15. | Meteorologie Nationale
SMM / Documentation
2, avenue Rapp
75007 Paris, France | 1 |
| 16. | Fang, Chung-Ming
Chinese Naval Hydrographic & Oceanographic Office
Tsoying, Kaohsiung
Taiwan 813
Republic of China | 1 |
| 17. | Dr. Geoff Kirby Head
Ocean Sciences Division
Admiralty Research Establishment
Southwell
Portland, Dorset DT5 256
Great Britain | 1 |

END

10-87

DTIC